

Practitioner's guide to laser pulse propagation models and simulation

Numerical implementation and practical usage of modern pulse propagation models

A. Couairon^{1,a}, E. Brambilla², T. Corti², D. Majus³, O. de J. Ramírez-Góngora⁴,
and M. Kolesik^{5,6,b}

¹ Centre de Physique Théorique, CNRS, École Polytechnique, 91128 Palaiseau, France

² Department of Physics and Mathematics, University of Insubria, via Valleggio 11, 22100 Como, Italy

³ Department of Quantum Electronics, Vilnius University, Sauletekio Avenue 9, Bldg. 3, 10222 Vilnius, Lithuania

⁴ Departamento de Ciencias Naturales y Matemáticas, Pontificia Universidad Javeriana-Cali, Avenida Cañas Gordas No 118-250, Cali, Colombia

⁵ College of Optical Sciences, Tucson, Arizona 85721, USA

⁶ Department of Physics, Constantine the Philosopher University, Nitra, Slovakia

Received 29 August 2011 / Received in final form 4 October 2011

Published online 7 December 2011

Abstract. The purpose of this article is to provide practical introduction into numerical modeling of ultrashort optical pulses in extreme nonlinear regimes. The theoretic background section covers derivation of modern pulse propagation models starting from Maxwell's equations, and includes both envelope-based models and carrier-resolving propagation equations. We then continue with a detailed description of implementation in software of Nonlinear Envelope Equations as an example of a mixed approach which combines finite-difference and spectral techniques. Fully spectral numerical solution methods for the Unidirectional Pulse Propagation Equation are discussed next. The modeling part of this guide concludes with a brief introduction into efficient implementations of nonlinear medium responses. Finally, we include several worked-out simulation examples. These are mini-projects designed to highlight numerical and modeling issues, and to teach numerical-experiment practices. They are also meant to illustrate, first and foremost for a non-specialist, how tools discussed in this guide can be applied in practical numerical modeling.

1 Introduction

As femtosecond lasers become available to many groups, simulation of propagation of optical pulses of ultra-short duration and their interaction with media gains new

^a e-mail: couairon@cpht.polytechnique.fr

^b e-mail: kolesik@optics.arizona.edu

importance. Modern experiments can barely exist without the support from modeling and simulation in order to understand and interpret measured data. This is especially true as nonlinear optics continues to explore ever more extreme regimes [1–4].

As a result of this development, the need to perform sophisticated simulations widens considerably. However, the development of software for numerical experiments requires specific knowledge, time and means that too often constitute a barrier between practitioners of real experiments and their modeling needs.

Fortunately, simulation in *ultrafast nonlinear optics* has reached a degree of maturity at which it makes sense for the community to have certain *standard tools* that can be used in support of state of the art experiments. Alongside researchers mainly involved in computer simulation, informed non-specialists have been more and more engaged in numerical modeling [5, 6]. In line with these trends, this paper targets all researchers, teachers and students working in the field of ultrafast nonlinear optics, who need to perform numerical simulation with proper understanding of modeling, implementation, and numerical issues. Our main aim is to provide a *practitioner's guide* to this wide audience. This is therefore a didactic- and instruction-motivated text which combines a detailed overview including necessary theoretical background, and a number of opportunities to hone practical skills through a set of exercises.

The physics governing the effects we aim to understand and model in ultrafast nonlinear optics belong to several broader fields: classical and quantum optics, electromagnetism, plasma physics, solid state physics. This rich physics results from laser-matter interaction in the *ultrashort* pulse regime, i.e. with sub-picosecond durations ($T \leq 10^{-12}$ s), typically produced by the Chirped Pulse Amplification technique [7]. Nowadays, lasers that produce extremely powerful ($1 \text{ PW} \equiv 10^{15} \text{ W}$) ultrashort pulses are developed. Very high light intensities in these pulses induce extreme *nonlinear effects* in any condensed material or gaseous medium. In this paper, we do not consider ultra-intense laser fields corresponding to the highest intensities achievable today (e.g. by tight focusing on a target the most powerful ultrashort laser pulses). Instead, we concentrate on the regime of intensities up to 10^{15} W/cm^2 obtained e.g. by focusing a pulse with power in the MW-TW range in a transparent dielectric medium (gas, liquid or solid). Our rationale is that in this regime, the *propagation* effects can be, and indeed are, as significant as the *interaction* effects. Laser-matter interaction at these intensities can induce nonlinear refraction index change or lead to partial ionization of the dielectric medium, however we do not consider the regime of interaction with fully ionized plasmas. Another boundary in nonlinear optics is given by the definition of *ultrashort*, or sub-picosecond times; they typically correspond to time scales above which the response of matter to laser excitation starts to involve heat transfer, relaxation processes and hydrodynamic phenomena. The pulse durations we consider are shorter than the time scales for these phenomena.

Ultrashort laser pulse filamentation constitutes an example of physical phenomena in ultrafast nonlinear optics where approaches described in this guide apply particularly well. It denotes a specific regime of nonlinear propagation of intense laser pulses $\mathcal{I} \sim 10^{13} - 10^{14} \text{ W/cm}^2$ with narrow beam widths, over distances much larger than a typical diffraction length. The reader is referred to Ref. [8] for the discovery of this phenomenon and to Ref. [3] for a detailed review of the rich physics it involves. Here we describe methods for the modeling of nonlinear laser pulse propagation that apply in a broader context, and we will use ultrashort laser pulse filamentation as a concrete context for illustrating a specific medium model *plug-in* for general pulse-propagation models.

The paper is organized into three main sections covering (i) the theoretic background (Sec. 2), (ii) the description of model implementation (Sec. 3) and (iii) a series of worked-out examples (Sec. 4). Section 2 starts from Maxwell's equations and presents the derivation of several families of propagation models suitable for nonlinear

Table 1. Carrier-Resolved Propagation Equations: in the laboratory frame: $\frac{\partial \tilde{E}}{\partial z} = iK_z(\omega, \mathbf{k}_\perp) \tilde{E} + iQ(\omega, \mathbf{k}_\perp) \frac{\tilde{P}}{2\epsilon_0}$, in the local pulse frame: $\frac{\partial \tilde{E}}{\partial \zeta} = i(K_z(\omega, \mathbf{k}_\perp) - \frac{\omega}{v_g}) \tilde{E} + iQ(\omega, \mathbf{k}_\perp) \frac{\tilde{P}}{2\epsilon_0}$. UPPE: Unidirectional Pulse Propagation Equation. FME: Forward Maxwell Equation. FWE: Forward Wave Equation. FOP: First-Order Propagation equation. UA: Unidirectional Approximation. MA: Minimal Approximation. SEWA: Slowly Evolving Wave Approximation. P: Paraxial. ND: No Dispersion.

Eq.	Ref.	Approximation	$K_z(\omega, \mathbf{k}_\perp)$	$Q(\omega, \mathbf{k}_\perp)$
UPPE	[5, 10]	UA	$\sqrt{k^2(\omega) - k_\perp^2}$	$\frac{\omega^2}{c^2 \sqrt{k^2(\omega) - k_\perp^2}}$
FME	[11]	SEWA, P	$k(\omega) - \frac{k_\perp^2}{2k(\omega)}$	$\frac{1}{n(\omega)} \frac{\omega}{c}$
FWE	[12, 13]	MA, P	$k(\omega) + \frac{v_g}{2\omega} [(k(\omega) - \frac{\omega}{v_g})^2 - k_\perp^2]$	$\frac{v_g}{c} \frac{\omega}{c}$
FOP	[14]	SEWA, P, ND	$\frac{\omega}{c} - \frac{ck_\perp^2}{2\omega}$	$\frac{\omega}{c}$

optics in regimes where Maxwell's equations are intractable. It introduces envelope models describing the propagation of laser pulses with many optical cycles as well as carrier-resolving pulse propagation models suited for few-cycle pulses. Section 3 deals with translation of theoretical models into simulation software. It shows how to implement propagation models by means of numerical algorithms that apply to a broad class of physical problems, namely those which exhibit a well-defined propagation direction. In particular, we present methods valid for envelope as well as carrier-resolving pulse propagation models, and discuss their advantages when the distance a laser pulse travels along the propagation direction is much larger than the wavelength and the dimensions of the pulse. Numerical implementation of medium-response models is treated in this section too, in particular for nonlinearities playing a role in the physics of ultrashort laser pulse filamentation. Finally, Section 4 is organized in the form of mini-projects that aim to introduce a non-specialist into simulations and let him gain confidence through practical exercise.

As a concluding word for this introduction, we would like to comment on the spirit of the presentation to help readers navigate the paper. This guide concentrates on propagation equations that take a canonical form, namely (i) Nonlinear Envelope Propagation Equations (listed in table 2) solved by combination of finite-difference and spectral methods, and (ii) Carrier Resolving Propagation Equations (listed in table 1) solved by purely spectral methods.¹ Our goal is to provide a self-contained overview of the state of the art in numerical simulation of femtosecond optical pulses, and, first and foremost, a practical way to embark on practical simulation. That is why Section 3 was written in the way allowing for a step-by-step building of general tools for numerical resolution of propagation equations, from the simplest to the most elaborate models. We show how to decompose a problem at hand, i.e. construction of a simulation engine into basic building blocks (e.g. linear propagation, nonlinear source terms, etc). Then we progressively include specifics describing various linear or nonlinear physical effects. Since partial differential equations of the same type as the considered propagation equations are encountered in several fields of physics (e.g., heat equation, advection-diffusion equations, amplitude equations in pattern

¹ Solution methods presented for paraxial Nonlinear Envelope Propagation Equations also apply to paraxial Carrier Resolving Propagation Equations.

Table 2. Envelope Propagation Equations: in the laboratory frame: $\frac{\partial \tilde{\mathcal{E}}}{\partial z} = i \left(\mathcal{K}(\Omega, \mathbf{k}_\perp) + \frac{\Omega}{v_g} \right) \tilde{\mathcal{E}} + i \mathcal{Q}(\Omega, \mathbf{k}_\perp) \frac{\tilde{\mathcal{P}}}{2\epsilon_0}$, in the pulse frame: $(\Omega \equiv \omega - \omega_0)$: $\frac{\partial \tilde{\mathcal{E}}}{\partial \zeta} = i \mathcal{K}(\Omega, \mathbf{k}_\perp) \tilde{\mathcal{E}} + i \mathcal{Q}(\Omega, \mathbf{k}_\perp) \frac{\tilde{\mathcal{P}}}{2\epsilon_0}$, where $\kappa(\omega) \equiv k_0 + (\omega - \omega_0)/v_g$ and $\omega \equiv \omega_0 + \Omega$. FEE: Forward Envelope Equation. NEE: Nonlinear Envelope Equation. LEE: Linear Envelope Equation. NLS: Nonlinear Schrödinger Equation. PC-NLS: Partially Corrected Nonlinear Schrödinger Equation. P: Paraxial. MA: Minimal Approximation. GFEA: Generalized Few-cycle Envelope Approximation. SEEA: Slowly Evolving Envelope Approximation. SEWA: Slowly Evolving Wave Approximation. SVEA: Slowly Varying Envelope Approximation.

Eq.	Ref.	Approximation	$\mathcal{K}(\Omega, \mathbf{k}_\perp)$	$\mathcal{Q}(\Omega, \mathbf{k}_\perp)$
FEE		P	$k(\omega) - \kappa(\omega) - \frac{k_\perp^2}{2k(\omega)}$	$\frac{\omega^2}{c^2 k(\omega)}$
NEE	[3]	MA	$\frac{k^2(\omega) - \kappa^2(\omega)}{2\kappa(\omega)} - \frac{k_\perp^2}{2\kappa(\omega)}$	$\frac{\omega^2}{c^2 \kappa(\omega)}$
NEE	[15]	GFEA	$k(\omega) - \kappa(\omega) - \frac{k_\perp^2}{2\kappa(\omega)}$	$\frac{\omega^2}{c^2 \kappa(\omega)}$
LEE	[16]	SEEA	$k(\omega) - \kappa(\omega) - \frac{k_\perp^2}{2\kappa(\omega)}$	0
NEE	[17]	SEWA	$k(\omega) - \kappa(\omega) - \frac{ck_\perp^2}{2n_0\omega}$	$\frac{\omega}{cn_0}$
NLS	[18]	SVEA	$\frac{k_0''\Omega^2}{2} - \frac{k_\perp^2}{2k_0}$	$\frac{\omega_0}{cn_0}$
PC-NLS			$k(\omega) - \frac{ck_\perp^2}{2n_0\omega_0} (2 - \frac{\omega}{\omega_0})$	$\frac{\omega}{cn_0}$

formation problems, soliton propagation equations), the techniques taught here are naturally applicable in many other fields.

This work is part of the 2011 edition of the Stella school [9]. Worked-out examples were executed by Stella students, and this part of the paper has been written by students themselves. As such this work is a case study in what the Practitioner's Guide aims to foster.

1.1 List of Propagation Equations discussed in this guide

All propagation equations considered in this guide can be expressed in Fourier space in a canonical form for unidirectional equations, either in the laboratory frame or in a moving frame co-propagating with the pulse under examination. Propagation equations are furthermore subdivided into carrier-resolving propagation equations (see table 1) and envelope propagation equations (see table 2), which all follow the canonical form. The numerical methods we present are valid to solve all propagation equations listed in tables 1 and 2. Independently of the distinction between carrier-resolving and envelope equations, we distinguished non-paraxial propagation equations, which can only be solved in the spectral domain for space-and-time by the method presented in section 3.2, from paraxial propagation equations which can also be solved by various combinations of finite-difference and spectral methods presented in section 3.1. The method presented for solving non-paraxial equations applies to paraxial equations, but the opposite is not true. Tables 1 and 2 list only scalar

propagation equations but we show that vectorial propagation equations can also be derived in the canonical form, thus our resolution methods extend to vectorial propagation equations.

2 Theory

When viewed through the eyes of a computational physicist, Maxwell's equations appear to consist of three coupled components. Divergence equations express initial conditions or constraints. They are *automatically* satisfied by any *good* numerical method (for example, direct Maxwell solvers will preserve $\nabla \cdot \mathbf{D} = 0$ as long as this was the case for the initial condition). Then we have the curl, or *propagation* equations, which give us the wave equation. These must be implemented, in some form, by the simulator. This part will be referred to as propagation models. The third component is embodied in material constitutive relations, which express properties of light-matter interactions. The latter part will be referred to as medium response models.

A good implementation in software should treat Maxwell system components as distinct. In other words, propagation models and medium responses should be separated as much as possible. In particular, realistic pulse evolution equations must not build on specific assumptions about the light-matter interactions. Organization of this theory Section reflects this divide and conquer approach. We will first discuss two classes of propagation models, namely envelope based and carrier-resolving in a general frame where all light-matter interactions are described by a nonlinear polarization. Then we deal with nonlinear medium properties that typically play a role in optical filamentation.

2.1 Derivation of unidirectional propagation models from the wave equation

2.1.1 From Maxwell's to the wave equation

Maxwell-Faraday and Maxwell-Ampere equations in a nonmagnetic dielectric medium read:

$$\nabla \times \mathbf{E} = -\frac{\partial \mathbf{B}}{\partial t} \quad (1)$$

$$\nabla \times \mathbf{B} = \mu_0 \left(\mathbf{J} + \frac{\partial \mathbf{D}}{\partial t} \right) \quad (2)$$

where \mathbf{E} and \mathbf{B} denote the electric and magnetic fields, \mathbf{D} denotes the electric displacement field, \mathbf{J} is the current density of free charges. All fields (amplitude and phase) depend on space variables $\mathbf{r} \equiv (x, y)$, time t and the propagation variable z , where we implicitly assumed existence of a well defined propagation direction. The constant μ_0 is the permeability of free space. The vector wave equation is derived from Eqs. (1,2) and the relation between the electric displacement field, the electric field, and the polarization which models the response of bound electrons in the medium to the electric field. The polarization itself usually depends on the electric field via a model forming a material constitutive relation. Without entering into the details of constitutive relations at this stage, it is useful to decompose the polarization into a linear (or first order) part $\mathbf{P}^{(1)}$ describing the response of the medium for weak electric fields, and a nonlinear part \mathbf{P} that is a nonlinear function of the electric field components and becomes relevant for stronger fields. The validity limit of this decomposition is expressed mathematically by the condition $\mathbf{P} \sim \mathbf{P}^{(1)}$ and corresponds physically to the range of electric fields where most electrons are still bound to the

nucleus. Laser intensities up to $\sim 10^{15} \text{ W/cm}^2$ belong to this regime when ionization induced by the optical field leads to a plasma of smaller density than that of the neutral medium. In this paper, we consider gases or dielectrics that are isotropic and homogeneous media, for which the components of the first-order polarization are linear functions of the components of the electric field in the frequency domain. The first order polarization follows the linear relation:

$$\hat{\mathbf{P}}^{(1)}(\mathbf{r}, \omega, z) = \epsilon_0 \chi^{(1)}(\omega) \hat{\mathbf{E}}(\mathbf{r}, \omega, z), \quad (3)$$

where ϵ_0 denotes the permittivity of free space and $\chi^{(1)}(\omega)$ is the linear susceptibility of the medium. The expression for the electric displacement reads:

$$\hat{\mathbf{D}}(\mathbf{r}, \omega, z) = \epsilon_0 \epsilon(\omega) \hat{\mathbf{E}}(\mathbf{r}, \omega, z) + \hat{\mathbf{P}}(\mathbf{r}, \omega, z), \quad (4)$$

where $\epsilon(\omega) \equiv 1 + \chi^{(1)}(\omega)$ denotes the relative permittivity of the medium [19]. By insertion of Eq. (4) in the Maxwell-Ampere equation, derivation in time of the resulting equation and by combining it with the curl of Maxwell-Gauss equation, we obtain the vectorial wave equation governing the evolution of the laser pulse in a transparent nonlinear medium. In the space-time domain with linear terms gathered on the left hand side and nonlinear material response on the right hand side, it reads:

$$\nabla^2 \mathbf{E} - \nabla(\nabla \cdot \mathbf{E}) - \frac{1}{c^2} \frac{\partial^2}{\partial t^2} \int_{-\infty}^t \epsilon(t-t') \mathbf{E}(\mathbf{r}, t', z) dt' = \mu_0 \left(\frac{\partial \mathbf{J}}{\partial t} + \frac{\partial^2 \mathbf{P}}{\partial t^2} \right) \quad (5)$$

where \mathbf{E} , \mathbf{J} and \mathbf{P} depend on (\mathbf{r}, t, z) and we use the same notation for the frequency dependent material permittivity $\epsilon(\omega) \equiv n^2(\omega)$, which defines the complex refraction index $n(\omega)$ of the material (including effects of linear absorption), and its time representation $\epsilon(t)$. Note that in the general case, the wave equation (5) involves a time-convolution of the permittivity with the electric field. In the following, it is useful to work with the space-frequency representation of Eq. (5):

$$\nabla^2 \hat{\mathbf{E}} - \nabla(\nabla \cdot \hat{\mathbf{E}}) + \frac{\omega^2 n^2(\omega)}{c^2} \hat{\mathbf{E}} = \mu_0 \left(-i\omega \hat{\mathbf{J}} - \omega^2 \hat{\mathbf{P}} \right) \quad (6)$$

where $\hat{\mathbf{E}}$, $\hat{\mathbf{J}}$ and $\hat{\mathbf{P}}$ depend on (\mathbf{r}, ω, z) . Resolution of Eq. (5) or Eq. (6) requires constitutive equations for the medium $\mathbf{P}(\mathbf{E})$, $\mathbf{J}(\mathbf{E})$ which define a model for the medium response (free and bound electrons). Examples are given in section 2.4.

Several successive approximations can be made to derive from Eq. (5) a pulse propagation equation that is suitable for numerical implementation when the processes to simulate occur over long propagation distances along a dominant direction z . We specify these approximations and the associated simplifications of Eq. (5) in the following sections.

2.1.2 Scalar wave equation

This section details approximations to reduce the vectorial wave equation to the scalar wave equation.

First, the electric field is assumed to remain linearly polarized along a direction \mathbf{e}_s transverse to the propagation axis. Thus, $\mathbf{E} = E\mathbf{e}_s$, $\mathbf{J} = J\mathbf{e}_s$, $\mathbf{P} = P\mathbf{e}_s$. There are actually two assumptions in one: First the electric field and the medium response (current \mathbf{J} , nonlinear polarization \mathbf{P}) are transverse, i.e., perpendicular to the propagation direction determined by the wave number \mathbf{k} . This standard assumption in propagation of electromagnetic fields means that the term $\nabla(\nabla \cdot \mathbf{E})$ in Eq. (5) can be neglected. This remains valid as long as beams are not too strongly focused. When the

beam numerical aperture² exceeds a few percent, a small longitudinal component E_z may develop close to the focus and makes this approximation invalid. We will see in section 2.1.7 how to deal with this situation by adding vectorial corrections. Second, there is the assumption that the electric field polarization is *linear*. The latter is not too restrictive as it essentially means that Eq. (5) can be rewritten in a scalar form by projection along the polarization direction \mathbf{e}_s :

$$(\partial_z^2 + \nabla_\perp^2)E(\mathbf{r}, t, z) - \frac{1}{c^2} \frac{\partial^2}{\partial t^2} \int_{-\infty}^t \epsilon(t - t') E(\mathbf{r}, t', z) dt' = \mu_0 \left(\frac{\partial^2 P}{\partial t^2} + \frac{\partial J}{\partial t} \right). \quad (7)$$

In the case of more than one direction for the electric field polarization, an equation of the same type as that of Eq. (7) would be obtained for each polarization direction, with coupling encoded in the material response (see section 2.3.3).

Without loss of generality, we note that the free charge current on the right hand side of Eq. (7) is formally equivalent to a time derivative of the nonlinear polarization: in the time domain, $J(\mathbf{r}, t, z) \leftrightarrow \partial_t P(\mathbf{r}, t, z)$. This has a counterpart in the frequency domain, $\hat{J}(\mathbf{r}, \omega, z) \leftrightarrow -i\omega \hat{P}(\mathbf{r}, \omega, z)$ where \hat{P} and \hat{J} are the Fourier transformed nonlinear polarization and current. Therefore, up to the point where we will need to specify the material nonlinear response and separate explicitly the current from the nonlinear polarization, we will consider a single term (nonlinear polarization) in propagation models. The current may then be reintroduced in any propagation equation by changing \hat{P} into $\hat{P} + i\hat{J}/\omega$. Equation (7) then becomes:

$$(\partial_z^2 + \nabla_\perp^2)E(\mathbf{r}, t, z) - \frac{1}{c^2} \partial_t^2 \int_{-\infty}^t n^2(\mathbf{r}, t - t', z) E(\mathbf{r}, t', z) dt' = \mu_0 \partial_t^2 P(\mathbf{r}, t, z) \quad (8)$$

which is formally easier to handle in the Fourier domain:

$$(\partial_z^2 + \nabla_\perp^2) \hat{E}(\mathbf{r}, \omega, z) + k^2(\omega) \hat{E}(\mathbf{r}, \omega, z) = -\mu_0 \omega^2 \hat{P}(\mathbf{r}, \omega, z) \quad (9)$$

where $k(\omega) \equiv n(\omega)\omega/c$.

2.1.3 Forward Maxwell Equation by factorization of the scalar wave equation

A standard way to derive a propagation equation, starting from Eq. (9), is to use a factorization method proposed by Feit and Fleck [20], which consists in separating the forward and backward propagators as:

$$(\partial_z + ik(\omega)) (\partial_z - ik(\omega)) \hat{E} = -\Delta_\perp \hat{E} - \mu_0 \omega^2 \hat{P}(\mathbf{r}, \omega, z). \quad (10)$$

In the absence of the right hand side, which represents diffraction in the transverse plane and the nonlinear polarization term, Eq. (10) would admit a superposition of two solutions:

$$\hat{E}(\omega, z) = \hat{A}_+(\omega) \exp[ik(\omega)z] + \hat{A}_-(\omega) \exp[-ik(\omega)z] \quad (11)$$

which represent waves propagating in the forward or in the backward direction. Equation (10) is transformed into a unidirectional propagation equation by assuming that the backward propagating component can be neglected with respect to

² The numerical aperture is defined as the ratio between beam diameter and focal distance.

the forward propagating component: $|\hat{A}_-| \ll |\hat{A}_+|$, leading to the approximation: $\partial_z + ik(\omega) \simeq 2ik(\omega)$, and to the Forward Maxwell Equation (FME) [11]:

$$\frac{\partial \hat{E}}{\partial z} = ik(\omega)\hat{E} + \frac{i}{2k(\omega)}\Delta_\perp \hat{E} + \frac{i}{2n(\omega)}\frac{\omega}{c}\frac{\hat{P}}{\epsilon_0}, \quad (12)$$

where μ_0 was replaced by $1/\epsilon_0 c^2$ so as to make apparent the quantity P/ϵ_0 which has the same unit as the electric field E . As shown in section 2.1.6, the FME (12) belongs to the class of carrier resolving paraxial propagation equations, which assumes that the extent of the angular spectrum of the propagated beams remains significantly smaller than the pulse central wave number in the propagation direction. This is usually the case except for beams that are tightly focused by means of microscope objectives. The FME therefore correctly models the propagation of beams with numerical aperture smaller than ~ 0.1 or conical beams with cone angle smaller than a few degrees [21].

We will see that in the spectral domain for both space and time, all unidirectional propagation equations take a canonical form:

$$\frac{\partial \tilde{E}}{\partial z} = iK_z(\omega, \mathbf{k}_\perp)\tilde{E} + iQ(\omega, \mathbf{k}_\perp)\frac{\tilde{P}}{2\epsilon_0} \quad (13)$$

where $K_z(\omega, \mathbf{k}_\perp)$ and $Q(\omega, \mathbf{k}_\perp)$ specifically depend on the approximations made to derive the equation. For the FME (12), we find:

$$K_z^{(\text{FME})}(\omega, \mathbf{k}_\perp) \equiv k(\omega) - \frac{k_\perp^2}{2k(\omega)}, \quad Q^{(\text{FME})}(\omega, \mathbf{k}_\perp) \equiv \frac{\omega}{cn(\omega)} \quad (14)$$

which are reported in Table 1 to facilitate comparison with other models.

2.1.4 From the laboratory to the pulse local frame

In numerical simulations, it is convenient to follow a propagating pulse in its motion when (i) it travels along large distances, (ii) the main phenomena under investigation are determined by the interaction with the medium over durations of the same order of magnitude as the pulse itself, and (iii) this interaction does not lead to a strong reflected component in the backward direction so as to keep valid the unidirectional approximation $|\hat{A}_-| \ll |\hat{A}_+|$ assumed in the previous section. The latter condition does not hold e.g. in a multiple layer mirror but conditions (i)–(iii) are valid for many experimental situations where propagation effects prevail over interaction with the medium. Following the pulse in its motion is then usually performed by a change of reference frame from the laboratory to the pulse local frame $(z, t) \rightarrow (\zeta, \tau)$, where τ denotes the retarded time in the pulse frame:

$$\zeta = z, \quad \tau = t - z/v_g \quad (15)$$

$$\partial_z = \partial_\zeta - (1/v_g)\partial_\tau, \quad \partial_t = \partial_\tau. \quad (16)$$

Note that v_g denotes a constant velocity corresponding to the change of reference frame. It is possible to chose v_g arbitrarily but a convenient choice is $v_g = 1/k'_0$, i.e. v_g coincides with the pulse group velocity obtained from the derivative $k'_0 \equiv (\partial k / \partial \omega)|_{\omega_0}$ of the dispersion relation in the medium $k = k(\omega)$ at the central frequency of the pulse ω_0 .

The spectral counterpart of the first equation of Eqs. (16), i.e. $\partial_z = \partial_\zeta + i(\omega/v_g)$,³ can be directly introduced into Equation (12) to obtain:

$$\frac{\partial \hat{E}}{\partial \zeta} = i[k(\omega) - \omega/v_g]\hat{E} + \frac{i}{2k(\omega)}\Delta_\perp \hat{E} + \frac{i}{2n(\omega)}\frac{\omega}{c}\frac{\hat{P}}{\epsilon_0}. \quad (17)$$

Equation (17) is still a paraxial propagation equation.

We will see through various examples that all unidirectional propagation equations originally expressed in the laboratory frame have a counterpart in the pulse frame given by a canonical form similar to Eq. (13) with the same Q and modified $K_z \rightarrow K_z - \omega/v_g$:

$$\frac{\partial \tilde{E}}{\partial \zeta} = i[K_z(\omega, \mathbf{k}_\perp) - \omega/v_g]\tilde{E} + iQ(\omega, \mathbf{k}_\perp)\frac{\tilde{P}}{2\epsilon_0}. \quad (18)$$

It can be readily seen that Equation (17) indeed takes the canonical form of Eq. (18) with K_z and Q defined by Eqs. (14). This means that the different ingredients in Eq. (18) constitute the basic building blocks for the numerical implementation of a flexible numerical tool that applies to all other carrier resolving propagation equations having the canonical form, with a simple change of (i) the frequency and wave number dependence of operators K_z and Q , and (ii) constitutive relations, i.e. $P(E)$.

2.1.5 Slowly Evolving Wave Approximation

The change of reference frame made in section 2.1.4 may be applied directly to the scalar wave equation by introducing $\partial_z = \partial_\zeta + i(\omega/v_g)$ into Eq. (9). This yields:

$$\frac{\partial^2 \hat{E}}{\partial \zeta^2} + 2i\frac{\omega}{v_g}\frac{\partial \hat{E}}{\partial \zeta} = -\Delta_\perp \hat{E} - [k^2(\omega) - \frac{\omega^2}{v_g^2}]\hat{E} - \frac{\omega^2}{c^2}\frac{\hat{P}}{\epsilon_0}. \quad (19)$$

From the still exact Eq. (19), the slowly evolving wave approximation (SEWA) consists in neglecting the second order derivative in ζ with respect to the second term: $|\partial_\zeta^2 \hat{E}| \ll 2(\omega/v_g)|\partial_\zeta \hat{E}|$, or equivalently:

$$\left| \partial_\zeta \hat{E} \right| \ll \frac{\omega}{v_g} |\hat{E}|. \quad (20)$$

Physically, this approximation means that the field amplitude *and* phase are evolving sufficiently slowly along the propagation direction ζ , i.e., the typical length scale to observe a variation of $\hat{E}(\mathbf{r}, \omega)$ is much larger than v_g/ω . Note that this approximation does not impose that the electric field be free of a fast oscillating carrier. The SEWA remains valid for carrier-resolving models with electric fields $E(\mathbf{r}, \tau) \propto \exp(-i\omega\tau)$. Originally proposed in the context of nonlinear envelope equations [17], the SEWA does not only consist in neglecting ∂_ζ^2 with respect to $(\omega/v_g)\partial_\zeta$ in Eq. (19), called here the Minimal approximation (MA), but also in another correction presented below. We start with the MA that corresponds to Eq. (20). Under the MA, Eq. (19) becomes a unidirectional propagation equation in the form of Eq. (13), called the Forward Wave Equation (FWE), which reads:

$$\frac{\partial \hat{E}}{\partial \zeta} = \frac{i}{2(\omega/v_g)}\Delta_\perp \hat{E} + i\frac{[k^2(\omega) - (\omega/v_g)^2]}{2(\omega/v_g)}\hat{E} + \frac{iv_g}{2c}\frac{\omega}{c}\frac{\hat{P}}{\epsilon_0}. \quad (21)$$

³ It is found by introducing the spectral counterpart of the second equation $\partial_\tau = -i\omega$ into the first equation of Eqs. (16).

It is readily seen⁴ that Eq. (21) takes the same form as Eq. (18) with

$$K_z^{(\text{FWE})}(\omega, \mathbf{k}_\perp) \equiv k(\omega) + \frac{v_g}{2\omega} \left(k(\omega) - \frac{\omega}{v_g} \right)^2 - \frac{v_g k_\perp^2}{2\omega}, \quad Q^{(\text{FWE})}(\omega, \mathbf{k}_\perp) \equiv \frac{v_g \omega}{c^2}. \quad (22)$$

The FWE (21) is a carrier resolving paraxial propagation equation, that allowed for simulations of filamentation and few-cycle pulse formation in argon, coupled with a model for high harmonic generation [12, 13, 22–24]. In order to specify the physical content of the MA, we consider a pulse with carrier frequency ω_0 : $E(z, t) \propto \exp(-i\omega_0 t + ik_0 z)$. In the pulse frame defined by Eq. (15), the field becomes $E(\zeta, \tau) \propto \exp[-i\omega_0 \tau + i(k_0 - \omega_0/v_g)\zeta]$. Thus, the field is oscillating at the same carrier frequency but the wave number seen in the pulse frame is $k_0 - \omega_0/v_g$, justifying the assumption that the field *evolves* along ζ sufficiently slowly with respect to the central wavelength, but does not necessarily vary slowly in time. The MA as well as other approximations of the SEWA class (see Table 1) only concern the evolution variable ζ , but do not impose any restriction on the variation in time τ of the pulse. Taking the ζ derivative of the field yields $\partial_\zeta E \propto (k_0 - \omega_0/v_g)E$. Inserting the latter expression in Eq. (20) leads to the condition:

$$\left| \frac{v_g k_0}{\omega_0} - 1 \right| \ll 1 \quad \leftrightarrow \quad \left| \frac{v_g n_0}{c} - 1 \right| \ll 1. \quad (23)$$

In other words, taking v_g as the pulse group velocity, the MA and the SEWA are justified if the relative difference between phase and group velocities is sufficiently small. More generally, the MA is valid for all frequencies of the pulse which have a phase velocity close enough to the velocity of the moving frame: $|v_g n(\omega)/c - 1| \ll 1$.

Comparison of Equation (21) with Eq. (17) shows that differences appear in the linear and nonlinear dispersion operators, i.e., the frequency-dependence in K_z and Q :

$$K_z^{(\text{FME})} - K_z^{(\text{FWE})} = -\frac{\omega}{2v_g} \left(1 - \frac{n(\omega)v_g}{c} \right)^2 - \left(1 - \frac{n(\omega)v_g}{c} \right) \frac{\mathbf{k}_\perp^2}{2k(\omega)} \quad (24)$$

$$Q^{(\text{FME})} - Q^{(\text{FWE})} = \frac{\omega^2}{c^2} \left(1 - \frac{n(\omega)v_g}{c} \right). \quad (25)$$

All terms on the right hand side of Eqs. (24) and (25) are first or second order terms with respect to the quantity $(1 - n(\omega)v_g/c)$. In addition to Eq. (20), the SEWA consists in also neglecting the right hand sides of Eqs. (24) and (25), thus rendering the FWE and the FME identical. A graphical representation of the MA and SEWA will be shown in Fig. 1.

2.1.6 Non paraxiality

The FME (17) and FWE (21) are paraxial propagation equations. We will see in this section how to account for nonparaxiality in unidirectional propagation equations. In Fourier space, Eq. (12) is expressed in the canonical form Eq. (13) with $K_z(\omega, \mathbf{k}_\perp) = K_z^{(\text{FME})}(\omega, \mathbf{k}_\perp)$ given by Eq. (14). This expression is exactly the first order, small $k_\perp/k(\omega)$ -expansion⁵ of the dispersion relation obtained from the left hand side of

⁴ $K_z^{(\text{FWE})}(\omega, \mathbf{k}_\perp) \equiv (v_g/2\omega)[k^2(\omega) - (\omega/v_g)^2] + \omega/v_g$.

⁵ $|k_\perp| \ll |k(\omega)|$ means that the validity limit of the expansion is the paraxial propagation regime.

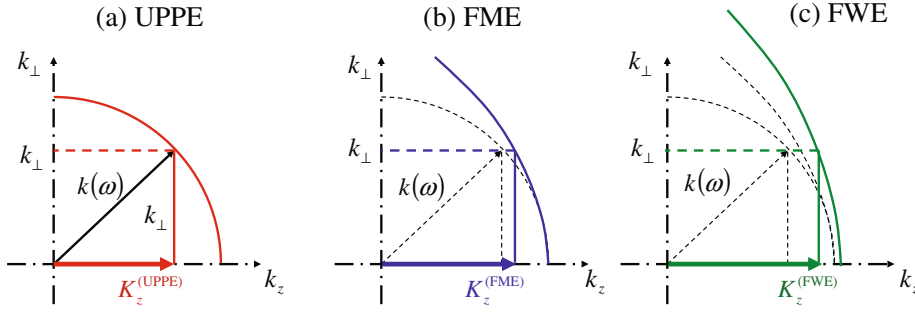


Fig. 1. Comparison of dispersion relations corresponding to the (a) UPPE, (b) FME and (c) FWE models. For a given medium characterized by its dispersion relation $k(\omega)$, the continuous curves show the dispersion relation $k_z(k_\perp, \omega)$ for each model as given by $K_z^{(UPPE)}$, $K_z^{(FME)}$, and $K_z^{(FWE)}$.

the wave equation (9):

$$K_z(\omega, k_\perp) = \sqrt{k^2(\omega) - k_\perp^2}. \quad (26)$$

In order to account for nonparaxial effects while keeping the advantage of the unidirectional propagation, the forward and backward propagators in Eq. (9) must be rewritten in the Fourier space as:

$$[\partial_z + iK_z(\omega, k_\perp)][\partial_z - iK_z(\omega, k_\perp)]\tilde{E} = -\mu_0\omega^2\tilde{P}. \quad (27)$$

As in Eq. (10), we now consider only the forward propagating component, i.e., we make the approximation $\partial_z + iK_z \sim 2iK_z$. This leads to the nonparaxial version of the FME, i.e. the Unidirectional Pulse Propagation Equation (UPPE):

$$\frac{\partial \tilde{E}}{\partial z} = iK_z(\omega, k_\perp)\tilde{E} + \frac{i}{2K_z(\omega, k_\perp)} \frac{\omega^2}{c^2} \frac{\tilde{P}}{\epsilon_0} \quad (28)$$

which follows the canonical form with $K_z^{(UPPE)}$ given by Eq. (26) and $Q^{(UPPE)} \equiv \omega^2/K_z^{(UPPE)}c^2$. The UPPE (28) was obtained here by the factorization method. Sections 2.3 and 2.3.3 will present a rigorous derivation from which the physical meaning of the approximation made in the factorization will appear.

Comparing the UPPE (28) with the FME (12), we note two important differences: (i) The FME involves differential operators in transverse spatial variables that describe diffraction in the transverse plane and space-time focusing due to the frequency dependence in the diffraction coefficient. Its nonparaxial version Eq. (28) is naturally expressed in the spectral domain due to the factorization method. Therefore, it cannot be translated easily in terms of differential operators in spatial variables, apart from a formal writing which becomes rather intractable when numerical implementation with finite difference is concerned. The effects of diffraction and space-time focusing are still described via the wave number (k_\perp) and frequency (ω) dependence in $K_z(\omega, k_\perp)$ [Eq. (26)], respectively, but nonparaxiality is now accounted for. (ii) Since $K_z^{(UPPE)}(\omega, k_\perp)$ depends on k_\perp and $Q^{(UPPE)}$ is obtained as a function of $K_z^{(UPPE)}$, wave numbers appear as new Fourier variables in the operator Q acting on nonlinear polarization in the UPPE (28), whereas Eqs. (14) show that the quantity $Q^{(FME)}$ is independant of k_\perp . This means that Eq. (28) is potentially much easier to implement numerically than equations in the form of the FME. Evaluation of the r.h.s. of Eq. (28) simply requires multiplications in the spectral domain $K_z(\omega, k_\perp) \times \tilde{E}(\omega, k_\perp)$

to describe linear propagation effects instead of dealing with the transverse Laplacian in the spatial domain as in Eq. (17) and paraxial equations in general. However, the nonlinear polarization $\tilde{P}(\omega, k_\perp)$ is often most easily evaluated in the space-time domain $P(\tau, r)$. Thus, the gain due to the simplicity in linear propagation in Eq. (28) is partly compensated by the need to perform three-dimensional Fourier transforms back and forth each time the nonlinear polarization $\tilde{P}(\omega, k_\perp)$ will be evaluated from $P(\tau, r)$.

Figure 1 shows a comparison of different approximations made to derive the UPPE, the FME and the FWE models. The axial wave number for the FME departs from that of the UPPE for large transverse wave numbers, which corresponds to the paraxiality assumption made in the FME. The axial wave number for the FWE exhibits a small departure from that of the FME even for small transverse wave numbers, which corresponds to a systematic distortion in the dispersion relation introduced when only the MA is assumed. The SEWA corrects this distortion. However, this deviation is really small for common focusing geometries and pulse durations. More limiting from the practical point of view is the uncertainty in medium parameters, and availability of dispersion relations accurate over wide frequency ranges [25].

2.1.7 Vectorial effects

Up to now, we have neglected $\nabla(\nabla \cdot \mathbf{E})$ in the wave equation. The goal of this section is to reintroduce this term so as to obtain a unidirectional propagation equation valid for describing vectorial effects, i.e. in the case of tightly focused beams. Maxwell-Gauss equation reads:

$$\nabla \cdot \mathbf{D} = \rho_f \quad (29)$$

where ρ_f denote the free space charge. By introducing the relation $\mathbf{D} = \epsilon_0 \mathbf{E} + \mathbf{P}^{(1)} + \mathbf{P}$ into Eq. (29), we obtain

$$\epsilon_0 \nabla \cdot \mathbf{E} = \rho_f - \nabla \cdot (\mathbf{P}^{(1)} + \mathbf{P}) \quad (30)$$

which can be expressed in the frequency domain by using Eq. (3):

$$\nabla \cdot \hat{\mathbf{E}} = \frac{1}{\epsilon_0 \epsilon(\omega)} (\hat{\rho}_f - \nabla \cdot \hat{\mathbf{P}}). \quad (31)$$

As long as the motion of charges does not occur over long spatial scales, the total free charge density can be considered zero even if the propagating laser pulse is so intense that it ionizes the medium. Ionization indeed leads to a plasma of negative electrons and positive ions; electroneutrality is satisfied at the macroscopic scale. Under these assumptions, reintroducing $\nabla \cdot \hat{\mathbf{E}}$ in the wave equation and considering the case of a linear or circular laser polarization along the transverse unit vector(s) \mathbf{e}_\perp , the Vectorial Forward Maxwell Equation (VFME), i.e., a paraxial propagation equation of the same type as the FME but including vectorial effects, is obtained as:

$$\frac{\partial \hat{\mathbf{E}}}{\partial z} = \frac{i}{2k(\omega)} \Delta_\perp \hat{\mathbf{E}} + ik(\omega) \hat{E} + \frac{i}{2k(\omega)\epsilon(\omega)} \mathbf{e}_\perp \cdot \nabla \left(\nabla \cdot \frac{\hat{\mathbf{P}}}{\epsilon_0} \right) + \frac{i}{2n(\omega)} \frac{\omega}{c} \frac{\hat{\mathbf{P}}}{\epsilon_0} \quad (32)$$

and its non paraxial unidirectional version as

$$\frac{\partial \tilde{\mathbf{E}}}{\partial z} = iK_z(\omega, k_\perp) \tilde{\mathbf{E}} - \frac{i}{2\epsilon(\omega)K_z(\omega, k_\perp)} \mathbf{k}_\perp \left(\mathbf{k}_\perp \cdot \frac{\tilde{\mathbf{P}}}{\epsilon_0} \right) + \frac{i}{2K_z(\omega, k_\perp)} \frac{\omega^2}{c^2} \frac{\tilde{\mathbf{P}}}{\epsilon_0} \quad (33)$$

where the second term on the right hand side accounts for vectorial effects. Note that Eqs. (32) and (33) involve the main component for the electric field which is perpendicular to the propagation direction. Vectorial effects, however, induce a small component in the longitudinal direction [26].

2.2 Derivation of envelope propagation equations

Envelope models are useful when there exist separate scales for the evolution of the pulse, a fast scale typically of the order of the wavelength, and a slow scale much larger than the wavelength. The pulse propagation can then be advantageously described by considering the electric field as a superposition of the pulse envelope \mathcal{E} with a carrier wave of frequency ω_0 : $E(\mathbf{r}, t, z) = \mathcal{E}(\mathbf{r}, t, z) \exp(ik_0 z - i\omega_0 t)$. In the local pulse frame: $E(\mathbf{r}, \tau, \zeta) = \mathcal{E}(\mathbf{r}, \tau, \zeta) \exp[i(k_0 - \omega_0/v_g)\zeta - i\omega_0\tau]$. A similar decomposition holds for the nonlinear polarization and the free charge current: $\{P, J\}(\mathbf{r}, \tau, \zeta) = \{\mathcal{P}, \mathcal{J}\}(\mathbf{r}, \tau, \zeta) \exp[i(k_0 - \omega_0/v_g)\zeta - i\omega_0\tau]$. Propagation equations for the envelope can be obtained by introducing this decomposition in any carrier resolving propagation equation or in the wave equation itself. We will examine both techniques. Formally, one simply needs to apply transformations to the evolution operator and time derivatives which read:

In the laboratory frame:

$$\partial_z E = \exp(ik_0 z - i\omega_0 t) [\partial_z + ik_0] \mathcal{E} \quad (34)$$

$$\partial_t E = \exp(ik_0 z - i\omega_0 t) [\partial_t - i\omega_0] \mathcal{E}. \quad (35)$$

In the pulse frame:

$$\partial_\zeta E = \exp(i(k_0 - \omega_0/v_g)\zeta - i\omega_0\tau) [\partial_\zeta + i(k_0 - \omega_0/v_g)] \mathcal{E}, \quad (36)$$

$$\partial_\tau E = \exp(i(k_0 - \omega_0/v_g)\zeta - i\omega_0\tau) [\partial_\tau - i\omega_0] \mathcal{E}. \quad (37)$$

We will see in several examples that these transformations lead to envelope propagation equations that also take the canonical form:

$$\frac{\partial \tilde{\mathcal{E}}}{\partial \zeta} = i\mathcal{K}(\Omega, \mathbf{k}_\perp) \tilde{\mathcal{E}} + i\mathcal{Q}(\Omega, \mathbf{k}_\perp) \frac{\tilde{\mathcal{P}}}{2\epsilon_0} \quad (38)$$

where $\Omega \equiv \omega - \omega_0$.

2.2.1 Nonlinear Envelope Equations from Carrier-Resolving Propagation equations

In this section, we derive nonlinear envelope equations obtained when the carrier and envelope decomposition is introduced in a carrier resolving propagation equation. Introducing Equations (36) and $\partial_z = \partial_\zeta + \omega/v_g$ into the canonical carrier resolving propagation equation (13) and removing the carrier wave $\exp[i(k_0 - \omega_0/v_g)\zeta - i\omega_0\tau]$ transforms it into Eq. (38) with

$$\mathcal{K}(\Omega, \mathbf{k}_\perp) \equiv K_z(\omega = \omega_0 + \Omega, \mathbf{k}_\perp) - \kappa(\omega = \omega_0 + \Omega) \quad (39)$$

$$\mathcal{Q}(\Omega, \mathbf{k}_\perp) \equiv Q(\omega = \omega_0 + \Omega, \mathbf{k}_\perp) \quad (40)$$

where $\kappa(\omega) \equiv k_0 + (\omega - \omega_0)/v_g$.

Using the Forward Maxwell Equation (17) as a starting point leads to the nonlinear envelope equation written in the spectral domain:

$$\frac{\partial \hat{\mathcal{E}}}{\partial \zeta} = \frac{i}{2k(\omega)} \Delta_{\perp} \hat{\mathcal{E}} + i[k(\omega) - \kappa(\omega)] \hat{\mathcal{E}} + \frac{i}{2k(\omega)} \frac{\omega^2}{c^2} \frac{\hat{\mathcal{P}}}{\epsilon_0}. \quad (41)$$

One notes that Eq. (41), as the original FME (17), is a paraxial equation. The main difference is that the fields in Eq. (17) have to be treated as real quantities with high temporal resolution of the order of the optical period, whereas the envelopes in Eq. (41) are complex quantities that require lower temporal resolution of the order of the pulse duration.

2.2.2 Nonlinear Envelope Equation from the wave equation

In this section, we derive Nonlinear Envelope Equations (NEE) directly from the wave equation. Since we aim at finding a nonlinear envelope equation in the pulse frame, we start from the wave equation (19) in the pulse frame, we introduce the carrier-envelope decomposition (36), remove the carrier and recombine the ω/v_g terms with $k_0 - \omega_0/v_g$ to form $\kappa(\omega) = k_0 + (\omega - \omega_0)/v_g$. This yields:

$$\frac{\partial^2 \hat{\mathcal{E}}}{\partial \zeta^2} + 2i\kappa(\omega) \frac{\partial \hat{\mathcal{E}}}{\partial \zeta} = -\Delta_{\perp} \hat{\mathcal{E}} - [k^2(\omega) - \kappa^2(\omega)] \hat{\mathcal{E}} - \frac{\omega^2}{c^2} \frac{\hat{\mathcal{P}}}{\epsilon_0}. \quad (42)$$

Equation (42) is exact and did not require any approximation except when vectorial effects in the original wave equation were neglected. We discuss below different Nonlinear Envelope Equations obtained by performing various approximations.

Minimal Approximation (MA) From Equation (42), the only required approximation to obtain a propagation equation in the canonical form for nonlinear envelope equations is that of neglecting ∂_{ζ}^2 . This yields a NEE that has been extensively used in simulations of ultrashort laser pulse filamentation [3]:

$$\frac{\partial \hat{\mathcal{E}}}{\partial \zeta} = \frac{i}{2\kappa(\omega)} \Delta_{\perp} \hat{\mathcal{E}} + i \frac{[k^2(\omega) - \kappa^2(\omega)]}{2\kappa(\omega)} \hat{\mathcal{E}} + \frac{i}{2\kappa(\omega)} \frac{\omega^2}{c^2} \frac{\hat{\mathcal{P}}}{\epsilon_0}. \quad (43)$$

Equation (43) contains all terms found in various types of NEEs found in the literature, derived under various approximations. To discuss these approximations, we rewrite the second term on the right hand side of Eq. (42) as:

$$k^2(\omega) - \kappa^2(\omega) = 2\kappa(\omega)[k(\omega) - \kappa(\omega)] + [k(\omega) - \kappa(\omega)]^2. \quad (44)$$

The rationale behind this rewriting is understood from a small $\Omega \equiv \omega - \omega_0$ Taylor expansion of the difference $k(\omega) - \kappa(\omega)$ around ω_0 , which introduces the high-order dispersive terms

$$k(\omega_0 + \Omega) - \kappa(\omega_0 + \Omega) = \sum_{l=2}^{+\infty} \frac{k_0^{(l)}}{l!} \Omega^l, \quad (45)$$

where $k_0^{(l)} \equiv \partial_{\omega}^l k|_{\omega_0}$. Note that the lowest order term in the second term on the rhs of Eq. (44) is $O(\Omega^4)$, and thus appears as a small correction with respect to the first term on the rhs of Eq. (44) that is $O(\Omega^2)$. Equation (43) is thus rewritten as

$$\frac{\partial \hat{\mathcal{E}}}{\partial \zeta} = \frac{i}{2\kappa(\omega)} \Delta_{\perp} \hat{\mathcal{E}} + i(k(\omega) - \kappa(\omega)) \hat{\mathcal{E}} + i \frac{[k(\omega) - \kappa(\omega)]^2}{2\kappa(\omega)} \hat{\mathcal{E}} + \frac{i}{2\kappa(\omega)} \frac{\omega^2}{c^2} \frac{\hat{\mathcal{P}}}{\epsilon_0} \quad (46)$$

which is convenient to review the various type of NEEs and compare them to the NEE-MA, since all of them neglect the $O(\Omega^4)$ third term on the rhs of Eq. (46). We will follow the terminology introduced by Kinsler et al. [15] that classifies various approximations in the literature on nonlinear envelope equations.

Generalized Few-cycle Envelope Approximation (GFEA). This approximation proposed by Kinsler et al [15] consists in first rewriting the envelope equation (42) by using Eq. (44) as for the NEE-MA:

$$2i\kappa(\omega)\frac{\partial\hat{\mathcal{E}}}{\partial\zeta} = -\Delta_{\perp}\hat{\mathcal{E}} - 2\kappa(\omega)[k(\omega) - \kappa(\omega)]\hat{\mathcal{E}} + \{[k(\omega) - \kappa(\omega)]^2 - \partial_{\zeta}^2\}\hat{\mathcal{E}} - \frac{\omega^2}{c^2}\frac{\hat{\mathcal{P}}}{\epsilon_0}. \quad (47)$$

Equation (47) is still exact. Then the third term on the r.h.s. of Equation (47) is neglected. This yields:

$$\frac{\partial\hat{\mathcal{E}}}{\partial\zeta} = i[k(\omega) - \kappa(\omega)]\hat{\mathcal{E}} + \frac{i}{2\kappa(\omega)}\Delta_{\perp}\hat{\mathcal{E}} + \frac{i}{2\kappa(\omega)}\frac{\omega^2}{c^2}\frac{\hat{\mathcal{P}}}{\epsilon_0}, \quad (48)$$

which has a counterpart in the space-time domain:

$$\frac{\partial\mathcal{E}}{\partial\zeta} = i\mathcal{D}(i\partial_{\tau})\mathcal{E} + \frac{i}{2k_0}\left(1 + i\frac{k'_0}{k_0}\partial_{\tau}\right)^{-1}\Delta_{\perp}\mathcal{E} + \frac{i}{2}\frac{\omega_0}{n_0c}\left(1 + i\frac{k'_0}{k_0}\partial_{\tau}\right)^{-1}\left(1 + \frac{i}{\omega_0}\partial_{\tau}\right)^2\frac{\mathcal{P}}{\epsilon_0}, \quad (49)$$

where $\mathcal{D}(i\partial_{\tau}) \equiv \sum_{l=2}^{+\infty} \frac{k_0^{(l)}}{l!}(i\partial_{\tau})^l$.

Thus there are two approximations in the GFEA: (i) An implicit small Ω -Taylor expansion of the dispersion operator is assumed and $O(\Omega^4)$ terms are neglected. The neglected terms precisely make the remaining dispersive terms of the NEE-GFEA (48) identical to those of the Forward Envelope Equation (41). (ii) The envelope is evolving slowly with respect to the propagation variable ζ : $|\partial_{\zeta}\mathcal{E}| \ll |k_0\mathcal{E}|$. In the original terminology introduced for the linear version of the NEE-GFEA (48), i.e. in the absence of a nonlinear polarization, the latter approximation was called the Slowly Evolving Envelope Approximation (SEEA) [16]. The operator $(1 + i(k'_0/k_0)\partial_{\tau})^{-1}$ in front of the diffraction term describe space-time focusing, i.e, a frequency dependence of diffraction carried by the effective propagation constant $\kappa(\omega) = k_0 + k'_0(\omega - \omega_0)$. In a medium with normal dispersion, red frequencies propagate faster than blue frequencies and a pulse with flat phase front would normally broaden. For a beam, due to space-time focusing, red frequencies are diffracted at larger angles than blue frequencies making diffraction equivalent to an anomalous dispersive phenomenon that can compensate normal dispersion [16].

Slowly Evolving Wave Approximation (SEWA). The SEWA was explained in the context of carrier-resolving equations. In the context of Nonlinear Envelope Equations, the SEWA was introduced by Brabec and Krausz [17] and consists in the same approximation as the GFEA with an additional approximation on the propagation constant $\kappa(\omega) \sim n_0\omega/c$ appearing in the second and third terms⁶ on the r.h.s. of Eq. (48). This leads to the spectral version of the Nonlinear Envelope Equation under the SEWA (NEE-SEWA):

$$\frac{\partial\hat{\mathcal{E}}}{\partial\zeta} = \frac{ic}{2n_0\omega}\Delta_{\perp}\hat{\mathcal{E}} + i[k(\omega) - \kappa(\omega)]\hat{\mathcal{E}} + \frac{i}{2n_0}\frac{\omega}{c}\frac{\hat{\mathcal{P}}}{\epsilon_0}, \quad (50)$$

⁶ It does not effectively appear in the first term. This can be verified by the Taylor expansion (45).

which was initially derived in the space-time domain [17]. From the NEE-GFEA, the approximation made to derive the NEE-SEWA is equivalently expressed in the temporal domain as $(1 + i(k'_0/k_0)\partial_\tau) \sim (1 + i/\omega_0^{-1}\partial_\tau)$, thus the space-time counterpart of the NEE-SEWA reads:

$$\frac{\partial \mathcal{E}}{\partial \zeta} = i\mathcal{D}(i\partial_\tau)\mathcal{E} + \frac{i}{2k_0} \left(1 + \frac{i}{\omega_0}\partial_\tau\right)^{-1} \Delta_\perp \mathcal{E} + \frac{i}{2} \frac{\omega_0}{n_0 c} \left(1 + \frac{i}{\omega_0}\partial_\tau\right) \frac{\mathcal{P}}{\epsilon_0}. \quad (51)$$

The SEWA introduces a slight distortion in the space-time focusing operator $(1 + (i/\omega_0)\partial_\tau)^{-1}$, obtained from its original version $(1 + i(k'_0/k_0)\partial_\tau)$ by the change $k'_0/k_0 \rightarrow \omega_0^{-1}$ which amounts to neglecting the difference between phase and group velocities $c/n_0 = \omega_0/k_0 \sim 1/k'_0$, as seen from the frequency dependence of effective propagation constant for the NEE-GFEA and NEE-SEWA $k_0 + k'_0(\omega - \omega_0) \sim k_0\omega/\omega_0$.

Slowly Varying Envelope Approximation (SVEA). At the lowest order, we may retain only the second order dispersive term in Equation (45), or the second and third orders:

$$k(\omega_0 + \Omega) - \kappa(\omega_0 + \Omega) = \frac{k_0^{(2)}}{2} \Omega^2 + O(\Omega^3), \quad (52)$$

and by keeping the lowest order in $\kappa(\omega_0 + \Omega) \sim k_0$ and $\omega \sim \omega_0$, we obtain from Eq. (43) an equation of the Nonlinear Schrödinger (NLS) type that is valid for pulses with a narrow spectrum:

$$\frac{\partial \hat{\mathcal{E}}}{\partial \zeta} = \frac{i}{2k_0} \Delta_\perp \hat{\mathcal{E}} + i \frac{k_0^{(2)}}{2} \Omega^2 \hat{\mathcal{E}} + \frac{i}{2n_0} \frac{\omega_0}{c} \frac{\hat{\mathcal{P}}}{\epsilon_0}. \quad (53)$$

Strictly speaking, the Nonlinear Schrödinger Equation involves a cubic dependence of the nonlinear polarization $\mathcal{P} \propto |\mathcal{E}|^2 \mathcal{E}$ as obtained with a Kerr nonlinearity (see section on the medium response) and is usually derived by introducing the carrier and envelope decomposition directly into the wave equation written in the space-time domain.

$$\frac{\partial \mathcal{E}}{\partial \zeta} = \frac{i}{2k_0} \Delta_\perp \mathcal{E} - i \frac{k_0^{(2)}}{2} \frac{\partial^2 \mathcal{E}}{\partial \tau^2} + \frac{i}{2n_0} \frac{\omega_0}{c} \frac{\mathcal{P}}{\epsilon_0}. \quad (54)$$

As written in Eq. (53), the NLS takes the canonical form of envelope equations. All nonlinear envelope equations derived in the previous sections can be considered as extended NLS equations in the sense that they can be obtained from the NLS equation by introducing the proper frequency dependence in the propagation constant, dispersion operator, and nonlinear dispersion.

2.3 Derivation of carrier-resolving pulse propagation models

The following section is devoted to rigorous derivations of Unidirectional Pulse Propagation Equations (UPPE). The idea here is to start from Maxwell's equations and avoid any approximation in the *propagation part of the problem*. As the reader will see, approximations become only necessary at the point when nonlinear interactions are considered, and then they only have to do with splitting an exact system of pulse propagation equations into two decoupled *unidirectional* equations.

The UPPE approach has been previously derived in two flavors, depending on direction of the numerically simulated evolution [5,10]. The latter can proceed either along the time coordinate, or it can follow a wave packet along one of the spatial coordinates (usually chosen as z) in the direction of the laser beam.

In the first case, termed *time-propagated evolution*, one has an initial condition (i.e. a given description of the electric and magnetic fields) specified in all space for a given initial time. The evolution is calculated along the time axis, and it naturally reflects the structure of Maxwell's equations.

In the second case, termed *z-propagated evolution*, the initial condition is given as a function of the local pulse time and of two transverse (with respect to the propagation direction) coordinates. Numerical evolution then proceeds along the propagation axis. From the mathematical point of view, this case is an initial value problem very much the same way the *t*-propagated case is. However, from the physical point of view this is a rather subtle issue because the true *initial* condition requires knowledge of the *total* field in the past and in the future. This includes the light which may be nonlinearly reflected from the focal region of an experiment. Only if we can assume that this is sufficiently weak, we can practically solve the corresponding initial value problem.

The time-propagated approach is common for solvers based on direct integration of Maxwell's equations. Accordingly, the time-propagated versions of UPPE are more suitable for tight-focusing scenarios when the non-paraxial effects start to play a role.

On the other hand, the *z*-propagated equations are easier to use in situations which allow to neglect longitudinal field components as contributing sources of nonlinear material responses. That is the main reason the *z*-propagated approach is more common, especially in nonlinear optics. In this paper, we will restrict our attention to the *z*-propagated case. However, numerical techniques described here are directly applicable to any *t*-propagated simulator implementation.

In relation to the previous section, the following material will reveal an interesting fact. We have seen that some of the equations derived from the wave equations seem to require certain approximations. Now it will be shown that in spite of this, the resulting equations are in a certain sense *exact*, and that assumptions needed for the Laplacian factorization are in fact not necessary but only sufficient conditions. This apparent contradiction originates in the fact that a solution to a unidirectional propagation equation must not satisfy the wave equation. Only two coupled unidirectional solutions (propagating in opposite directions) must, and indeed obey the wave equation.

2.3.1 A simplified case first: One-dimensional Maxwell's equations

The most important ingredient in unidirectional evolution equations is the separation of those wave-form portions which propagate in opposite direction. To emphasize this, and also to make the subsequent full derivation easier to digest, we start with a simplified case of one-dimensional Maxwell's equations. This reduced case is free of notational complications while it illustrates all important steps of the fully vectorial treatment. In particular, it shows very clearly that a pair of unidirectional equations is exact.

The one dimensional Maxwell equations reduced to linearly polarized electric field can be written as (for convenience and notational simplicity, appropriate scaled units are used in this subsection):

$$\begin{aligned} -\partial_z H &= \partial_t E + \partial_t P \\ -\partial_z E &= \partial_t H \end{aligned} \tag{55}$$

where z is the optical axis and E and H are implicitly understood to be orthogonal to each other and to z . P represents nonlinear polarization that itself is a functional of the electric field history at a given spatial point. Section 2.4 provides several examples

the reader can keep in mind, but a concrete form of this nonlinearity is completely unimportant for the purpose of the following derivation.

This simplified Maxwell system has harmonic waves as solutions in the linear regime when $P = 0$:

$$\begin{aligned}\mathcal{E}_\lambda(\omega, z, t) &= \mathcal{E}_0 \exp[-i\omega t + i\lambda k(\omega)z] \\ \mathcal{H}_\lambda(\omega, z, t) &= \lambda \mathcal{H}_0 \exp[-i\omega t + i\lambda k(\omega)z] \quad \omega > 0 \quad \lambda = \pm 1.\end{aligned}\tag{56}$$

The direction indicator λ selects forward and backward (or left and right) propagating waves. We can use these plane-waves as a basis in which to express a full, nonlinear solution as

$$E = \sum_{\mu=\pm 1} \int d\Omega A_\mu(\Omega, z) \mathcal{E}_\mu(\Omega, z, t) \quad H = \sum_{\mu=\pm 1} \int d\Omega A_\mu(\Omega, z) \mathcal{H}_\mu(\Omega, z, t).$$

Here, $A_\mu(\Omega, z)$ are spectral amplitudes for which we have to find an evolution equation. Taking (55), and multiplying with the above linear basis solutions we get

$$\begin{aligned}\mathcal{E}_\lambda \partial_z H &= -\mathcal{E}_\lambda \partial_t E - \mathcal{E}_\lambda \partial_t P \\ \mathcal{H}_\lambda \partial_z E &= -\mathcal{H}_\lambda \partial_t H.\end{aligned}\tag{57}$$

In these equations and in following formulas, we assume that the arguments of \mathcal{E}_λ and \mathcal{H}_λ are Ω, z, t . We now add these two equations, and collect terms that constitute full derivatives while using the fact that $\mathcal{H}_\lambda, \mathcal{E}_\lambda$ solve the linear Maxwell system:

$$\partial_z [\mathcal{E}_\lambda H + \mathcal{H}_\lambda E] = -\partial_t [\mathcal{E}_\lambda H + \mathcal{H}_\lambda E] - \mathcal{E}_\lambda \partial_t P.\tag{58}$$

The next step is to integrate over the whole domain perpendicular to the direction of propagation. In this simplified case it means the t domain alone. After integration over t , the middle term gives rise to boundary terms at past and future temporal infinities. To get rid of these, we will restrict our solution space to those functions which satisfy

$$\lim_{t \rightarrow \pm\infty} [\mathcal{E}_\lambda H(z, t) + \mathcal{H}_\lambda E(z, t)] = 0.\tag{59}$$

What this condition requires is that for every fixed z along the laser beam axis, the field will vanish if we wait for a sufficiently long time. In other words, light energy will dissipate into positive and negative z -infinities. This is certainly a very benign assumption in the context of pulse propagation, because this is exactly what happens to localized pulsed wave packets - they eventually disappear from our sight.

The above condition eliminates the middle term in (58), and the rest can be transformed as follows. First, in the left-hand side we use the fact that the basis solutions are orthogonal, and after time integration they eliminate the sum over Ω and the modal index μ :

$$\begin{aligned}& \int dt \partial_z [\mathcal{E}_\lambda(\omega, z, t) H + \mathcal{H}_\lambda(\omega, z, t) E] \\ &= \int dt \partial_z \mathcal{E}_\lambda(\omega, z, t) \sum_{\mu=\pm 1} \int d\Omega A_\mu(\Omega, z) \mathcal{H}_\mu(\Omega, z, t) \\ & \quad + \int dt \partial_z \mathcal{H}_\lambda(\omega, z, t) \sum_{\mu=\pm 1} \int d\Omega A_\mu(\Omega, z) \mathcal{E}_\mu(\Omega, z, t) \\ &= 2\lambda \mathcal{E}_0 \mathcal{H}_0 \partial_z A_\lambda(\omega, z).\end{aligned}\tag{60}$$

On the right-hand side of Eq. (58), the polarization term yields essentially a Fourier transform

$$- \int dt \mathcal{E}_\lambda(\omega, z, t) \partial_t P = i\omega \exp[-i\lambda k(\omega)z] \hat{P}(\omega, z).$$

Collecting both sides, we arrive at an evolution equation for spectral amplitudes:

$$\partial_z A_\lambda(\omega, z) = \frac{i\omega}{2\lambda \mathcal{E}_0 \mathcal{H}_0} \exp[-i\lambda k(\omega)z] \hat{P}(\omega, z). \quad (61)$$

To obtain a corresponding equation for the electric field, we recall that

$$\hat{E}_\lambda(\omega, z) = A_\lambda(\omega, z) \exp[i\lambda k(\omega)z]$$

and expressing its z -derivatives using the evolution equation (61) for the spectral amplitudes, we have:

$$\partial_z \hat{E}_\lambda(\omega, z) = i\lambda k(\omega) \hat{E}_\lambda(\omega, z) + i\lambda \frac{\omega}{2\mathcal{E}_0 \mathcal{H}_0} \hat{P}(\omega, z).$$

This is a pair of equations for forward and backward ($\lambda = \pm 1$) propagating fields. The two are coupled through the polarization which depends on their sum. Explicitly,

$$P(z, t) = P[E_+(z, t) + E_-(z, t)].$$

where the concrete functional form of this dependence is not important for the present purpose, but as an example one can consider the instantaneous Kerr nonlinearity for which the polarization is simply proportional to the cube of the electric field (for more examples, see section 2.4):

$$P(z, t) = P[E_+(z, t) + E_-(z, t)] \propto [E_+(z, t) + E_-(z, t)]^3.$$

The above derivation illustrates the scheme we will use in the next Section to derive the general, fully vectorial Unidirectional Pulse Propagation Equation. The important point to note here is that within the admissible subspace specified by condition (59), the pair of unidirectional equations is *exact*.

2.3.2 Maxwell's equations as a boundary value problem for pulsed beam propagation

As a first step in derivation of various versions of UPPE, we derive an exact coupled-modes system of equations. Electromagnetic fields of a light pulse propagating along the z -axis can be expanded into modal contributions that reflect the geometry of the waveguide (we can consider a homogeneous medium as a special case of the latter).

$$\begin{aligned} \mathbf{E}(x, y, z, t) &= \sum_{m, \omega} A_m(\omega, z) \mathcal{E}_m(\omega, x, y) e^{i\beta_m(\omega)z - i\omega t} \\ \mathbf{H}(x, y, z, t) &= \sum_{m, \omega} A_m(\omega, z) \mathcal{H}_m(\omega, x, y) e^{i\beta_m(\omega)z - i\omega t}. \end{aligned} \quad (62)$$

Here, m labels all transverse modes, and an initial condition $A_m(\omega, z = 0)$ is supposed to be given or calculated from the known field values at $z = 0$. Note that the above expansion is valid for the transverse components only, and that the modal index m is a short hand for all quantities which are required to specify a unique propagation mode. For example, in a homogeneous bulk medium, the eigen modes are the well known

plane waves, and the index m represents polarization, two transverse wave numbers, and a binary value selecting the forward or backward direction of propagation.

To save space and reduce clutter, the following short-hand notation will be used below

$$\begin{aligned}\mathcal{E}_m &\equiv \mathcal{E}_m(\omega, x, y)e^{i\beta_m(\omega)z - i\omega t} \\ \mathcal{H}_m &\equiv \mathcal{H}_m(\omega, x, y)e^{i\beta_m(\omega)z - i\omega t}.\end{aligned}\tag{63}$$

We consider a non-magnetic medium ($\mu = \mu_0$) with a linear permittivity $\epsilon(\omega, x, y)$ that does not depend on the propagation coordinate z which coincides with what we consider forward and backward propagation direction. Note that the permittivity or, equivalently, the index of refraction may depend on the transverse coordinates x, y . That would be the case for example in a micro-structured waveguide, or in a hollow-core fiber or capillary; at this first stage, we want to treat bulk media and fiber-like geometries together. Later we can *branch* and derive separate, specialized equations for waveguides and for bulk media.

The starting point of our derivations is the Maxwell equations:

$$\begin{aligned}\mathbf{J} + \partial_t \mathbf{P} + \epsilon_0 \partial_t \epsilon * \mathbf{E} &= \nabla \times \mathbf{H} \\ -\mu_0 \partial_t \mathbf{H} &= \nabla \times \mathbf{E}\end{aligned}\tag{64}$$

where the star represents a convolution so that the term is a short hand for

$$\epsilon_0 \partial_t \epsilon * \mathbf{E} = \epsilon_0 \partial_t \int_0^\infty d\tau \epsilon(\tau) \mathbf{E}(t - \tau).$$

Here $\epsilon(\tau)$ is the temporal representation of frequency-dependent permittivity $\epsilon(\omega)$. The same notation will be used for both quantities, and their arguments will serve to distinguish them where needed.

As a first step, we scalar-multiply Maxwell's equations by complex conjugate modal fields

$$\begin{aligned}\mathcal{E}_m^* \cdot (\mathbf{J} + \partial_t \mathbf{P}) + \epsilon_0 \mathcal{E}_m^* \cdot \partial_t \epsilon * \mathbf{E} &= \mathcal{E}_m^* \cdot \nabla \times \mathbf{H} \\ -\mu_0 \mathcal{H}_m^* \cdot \partial_t \mathbf{H} &= \mathcal{H}_m^* \cdot \nabla \times \mathbf{E}.\end{aligned}\tag{65}$$

Using the formula $\mathbf{b} \cdot (\nabla \times \mathbf{a}) = \nabla \cdot (\mathbf{a} \times \mathbf{b}) + \mathbf{a} \cdot (\nabla \times \mathbf{b})$, we transform both right-hand sides to obtain

$$\begin{aligned}\mathcal{E}_m^* \cdot (\mathbf{J} + \partial_t \mathbf{P}) + \epsilon_0 \mathcal{E}_m^* \cdot \partial_t \epsilon * \mathbf{E} &= \nabla \cdot [\mathbf{H} \times \mathcal{E}_m^*] + \mathbf{H} \cdot [\nabla \times \mathcal{E}_m^*] \\ -\mu_0 \mathcal{H}_m^* \cdot \partial_t \mathbf{H} &= \nabla \cdot [\mathbf{E} \times \mathcal{H}_m^*] + \mathbf{E} \cdot [\nabla \times \mathcal{H}_m^*].\end{aligned}\tag{66}$$

Now we can take advantage of the fact the modal fields themselves satisfy Maxwell's equations

$$\begin{aligned}\nabla \times \mathcal{E}_m^* &= -\mu_0 \partial_t \mathcal{H}_m^* \\ \nabla \times \mathcal{H}_m^* &= \epsilon_0 \partial_t \epsilon * \mathcal{E}_m^*,\end{aligned}\tag{67}$$

and therefore the previous equations can be written as

$$\begin{aligned}\mathcal{E}_m^* \cdot (\mathbf{J} + \partial_t \mathbf{P}) + \epsilon_0 \mathcal{E}_m^* \cdot \partial_t \epsilon * \mathbf{E} &= \nabla \cdot [\mathbf{H} \times \mathcal{E}_m^*] - \mu_0 \mathbf{H} \cdot \partial_t \mathcal{H}_m^* \\ -\mu_0 \mathcal{H}_m^* \cdot \partial_t \mathbf{H} &= \nabla \cdot [\mathbf{E} \times \mathcal{H}_m^*] + \epsilon_0 \mathbf{E} \cdot \partial_t \epsilon * \mathcal{E}_m^*.\end{aligned}\tag{68}$$

Next, we subtract the two equations and collect terms that constitute full time derivatives

$$\mathcal{E}_m^* \cdot (\mathbf{J} + \partial_t \mathbf{P}) + \partial_t [\epsilon_0 \mathcal{E}_m^* \cdot \epsilon * \mathbf{E}] = \nabla \cdot [\mathbf{H} \times \mathcal{E}_m^*] - \partial_t [\mu_0 \mathcal{H}_m^* \cdot \mathbf{H}] - \nabla \cdot [\mathbf{E} \times \mathcal{H}_m^*]. \quad (69)$$

Now we integrate over the whole xyt domain. Note that all terms except the first and ∂_z , which is implicit in the $\nabla \cdot$ operator, are derivatives that give rise to *surface terms* after integration over x, y, t . These surface terms are supposed to vanish far from the axis of the laser beam, as well as in past and future temporal infinities. Intuitively, admissible solutions include spatially and temporally localized pulse-like solutions. As a consequence, the only surviving derivatives will be ∂_z :

$$\int \mathcal{E}_m^* \cdot (\mathbf{J} + \partial_t \mathbf{P}) dx dy dt = \partial_z \int z \cdot [\mathbf{H} \times \mathcal{E}_m^*] dx dy dt - \partial_z \int z \cdot [\mathbf{E} \times \mathcal{H}_m^*] dx dy dt. \quad (70)$$

Here and in what follows, t integrations are understood as: $\int dt \equiv \frac{1}{T} \int_{-T/2}^{+T/2} dt$ where T is a large normalization volume, and integrals over x, y are understood in a similar way. This will give us a convenient way to obtain the correct normalization and *translate* it into implementation which will be in terms of numerical Fourier transforms.

Because only transverse field components enter the above equation, we can use our modal expansion here (recall that those are only valid for transverse vector components):

$$\begin{aligned} & \int \mathcal{E}_m^* \cdot (\mathbf{J} + \partial_t \mathbf{P}) dx dy dt \\ &= \partial_z \int \mathbf{z} \cdot \left[\sum_{n, \Omega} A_n(\Omega, z) \mathcal{H}_n(\Omega) \times \mathcal{E}_m^*(\omega) \right] e^{i\beta_n(\Omega)z - i\Omega t} e^{-i\beta_m(\omega)z + i\omega t} dx dy dt \\ & - \partial_z \int \mathbf{z} \cdot \left[\sum_{n, \Omega} A_n(\Omega, z) \mathcal{E}_n(\Omega) \times \mathcal{H}_m^*(\omega) \right] e^{i\beta_n(\Omega)z - i\Omega t} e^{-i\beta_m(\omega)z + i\omega t} dx dy dt. \end{aligned} \quad (71)$$

Integration over time gives a Kronecker delta between angular frequencies, $\delta_{\Omega\omega}$, which in turn reduces the sum over Ω :

$$\begin{aligned} & \int \mathcal{E}_m^* \cdot (\mathbf{J} + \partial_t \mathbf{P}) dx dy dt \\ &= \partial_z \int \mathbf{z} \cdot \left[\sum_n A_n(\omega, z) \mathcal{H}_n(\omega, x, y) \times \mathcal{E}_m^*(\omega, x, y) \right] e^{i\beta_n(\omega)z} e^{-i\beta_m(\omega)z} dx dy \\ & - \partial_z \int \mathbf{z} \cdot \left[\sum_n A_n(\omega, z) \mathcal{E}_n(\omega, x, y) \times \mathcal{H}_m^*(\omega, x, y) \right] e^{i\beta_n(\omega)z} e^{-i\beta_m(\omega)z} dx dy. \end{aligned} \quad (72)$$

Collecting like terms results in an equation

$$\begin{aligned} & \int \mathcal{E}_m^* \cdot (\mathbf{J} + \partial_t \mathbf{P}) dx dy dt = \partial_z \sum_n A_n(\omega, z) e^{i\beta_n(\omega)z} e^{-i\beta_m(\omega)z} \\ & \times \int \mathbf{z} \cdot [\mathcal{H}_n(\omega, x, y) \times \mathcal{E}_m^*(\omega, x, y) - \mathcal{E}_n(\omega, x, y) \times \mathcal{H}_m^*(\omega, x, y)] dx dy. \end{aligned} \quad (73)$$

At this point we are going to use a general property of electromagnetic modal fields which constitute an orthogonal basis: all radiative waveforms can be expressed as their linear combinations. To calculate such expansions, one can utilize the following orthogonality relation

$$\int \mathbf{z} \cdot [\mathcal{E}_m \times \mathcal{H}_n^* - \mathcal{H}_m \times \mathcal{E}_n^*] dx dy = 2\delta_{m,n} N_m(\omega). \quad (74)$$

Here $N_m(\omega)$ is a normalization constant, whose explicit functional form has to be derived for each concrete set of modes.

Orthogonality of modes is used to reduce the sum over n in (73)

$$\int \mathcal{E}_m^*(\mathbf{J} + \partial_t \mathbf{P}) dx dy dt = -\partial_z \sum_n A_n(\omega, z) e^{i\beta_n(\omega)z} e^{-i\beta_m(\omega)z} 2\delta_{m,n} N_m(\omega), \quad (75)$$

and we finally obtain an evolution equation for our expansion coefficients:

$$\begin{aligned} \partial_z A_m(\omega, z) = & -\frac{1}{2N_m(\omega)XYT} \int_{-T/2}^{+T/2} dt \int_{-Y/2}^{+Y/2} dy \int_{-X/2}^{+X/2} dx \\ & \times e^{-i\beta_m(\omega)z+i\omega t} \mathcal{E}_m^*(\omega, \mathbf{r}) \cdot [\mathbf{J}(\mathbf{r}, t) + \partial_t \mathbf{P}(\mathbf{r}, t)]. \end{aligned} \quad (76)$$

This is the common representation for various z -propagated unidirectional equations, and in fact the form in which numerical solutions should be implemented. In the following sections, we will specialize this to the case of bulk media.

2.3.3 z -propagated UPPE for homogeneous media: General case

In this section, Eq. (76) is specialized for the case of a homogeneous medium. This is done by inserting explicit expressions for a given family of modal fields. In a bulk medium, these field modes are the well-known plane waves. They can be labeled by transverse wave numbers k_x, k_y , by a polarization index $s = 1, 2$, and by a \pm sign signifying the direction of propagation along the z direction. Thus the index m , which we used to label modes in the preceding Section, is actually a list:

$$m \equiv k_x, k_y, s, \pm. \quad (77)$$

The following notation will be used for the frequency- and wave number-dependent propagation constant of a plane wave characterized by its angular frequency ω :

$$\beta_{k_x, k_y, s, \pm}(\omega) \equiv k_z(\omega, k_x, k_y) = \sqrt{k^2(\omega) - k_x^2 - k_y^2}, \quad (78)$$

where $k^2(\omega) \equiv \epsilon(\omega)\omega^2/c^2$ depends on the dispersive properties of the medium through the permittivity ϵ .

Electric and magnetic amplitudes in plane waves are mutually determined by Maxwell's equations. We can choose them as

$$\mathcal{E}_{k_x, k_y, s, \pm} = \mathbf{e}_s \exp[ik_x x + ik_y y \pm ik_z(\omega, k_x, k_y)z] \quad (79)$$

$$\mathcal{H}_{k_x, k_y, s, \pm} = \frac{1}{\mu_0 \omega} \mathbf{k} \times \mathcal{E}_{k_x, k_y, \omega, s, \pm}. \quad (80)$$

The polarization of modal fields is determined by polarization vectors $\mathbf{e}_{s=1,2}$ which are of unit length and are normal to the wave-vector

$$\mathbf{k} = \{k_x, k_y, k_z \equiv \sqrt{k^2(\omega) - k_x^2 - k_y^2}\}. \quad (81)$$

Using the above formulas, it is straightforward to calculate the modal normalization constant

$$\begin{aligned} 2N_{k_x, k_y, s, \pm}(\omega) &= \int \mathbf{z} \cdot [\mathcal{E}_m \times \mathcal{H}_m^* - \mathcal{H}_m \times \mathcal{E}_m^*] dx dy \\ &= 2\mathbf{z} \cdot [\mathbf{e}_s \times (\mathbf{k} \times \mathbf{e}_s)] \frac{1}{\mu_0 \omega} = \pm 2k_z(\omega, k_x, k_y) \frac{1}{\mu_0 \omega} \end{aligned} \quad (82)$$

$$N_{k_x, k_y, s, \pm}(\omega) = \pm \frac{k_z(\omega, k_x, k_z)}{\mu_0 \omega}. \quad (83)$$

Now we can insert expressions for modal fields and the corresponding normalization constant into coupled mode equation Eq. (76) to obtain

$$\partial_z A_{k_x, k_y, s, \pm}(\omega, z) = \mp \frac{\omega \mu_0}{2k_z} e^{\mp i k_z z} \int \frac{dx dy dt}{L_x L_y T} e^{i(\omega t - \mathbf{k} \cdot \mathbf{r})} \times \mathbf{e}_s \cdot [\mathbf{J}(\mathbf{r}, t, z) + \partial_t \mathbf{P}(\mathbf{r}, t, z)]. \quad (84)$$

The above integral is nothing but a spatial and temporal Fourier transform, and one can write the equations in the spectral domain

$$\partial_z A_{k_x, k_y, s, +}(\omega, z) = \frac{\omega}{2\epsilon_0 c^2 k_z} e^{-i k_z z} \mathbf{e}_s \cdot [i\omega \mathbf{P}_{k_x, k_y}(\omega, z) - \mathbf{J}_{k_x, k_y}(\omega, z)]. \quad (85)$$

This is the propagation equation that will actually be solved numerically because it is cast in terms of the slowest variables our propagation problem has. We can see that the only source of evolution in spectral amplitudes is nonlinearity.

For those who prefer to see evolution equations for electric fields proper, we express the above in terms of the electric field rather than in terms of modal expansion coefficients. From a modal expansion, the transverse part of the electric field is

$$\mathbf{E}_{k_x, k_y, +}^\perp(\omega, z) = \sum_{s=1,2} \mathbf{e}_s^\perp \mathbf{A}_{k_x, k_y, s, +}(\omega, z) e^{i k_z(\omega, \mathbf{k}_\perp)z}, \quad (86)$$

and therefore its z derivative reads

$$\partial_z \mathbf{E}_{k_x, k_y, +}^\perp(\omega, z) = i k_z(\omega, \mathbf{k}_\perp) \mathbf{E}_{k_x, k_y, +}^\perp(\omega, z) + \sum_{s=1,2} \mathbf{e}_s^\perp \partial_z \mathbf{A}_{k_x, k_y, s, +}(\omega, z) e^{i k_z(\omega, \mathbf{k}_\perp)z}. \quad (87)$$

Using Eq. (85), we obtain the vectorial UPPE for a homogeneous medium:

$$\begin{aligned} \partial_z \mathbf{E}_{k_x, k_y, +}^\perp(\omega, z) = & +i k_z \mathbf{E}_{k_x, k_y, +}^\perp(\omega, z) \\ & + \sum_{s=1,2} \mathbf{e}_s^\perp \mathbf{e}_s \cdot \left[\frac{i\omega^2}{2\epsilon_0 c^2 k_z} \mathbf{P}_{k_x, k_y}(\omega, z) - \frac{\omega}{2\epsilon_0 c^2 k_z} \mathbf{J}_{k_x, k_y}(\omega, z) \right]. \end{aligned} \quad (88)$$

Of course, an analogous equation holds for the backward propagating component:

$$\begin{aligned} \partial_z \mathbf{E}_{k_x, k_y, -}^\perp(\omega, z) = & -i k_z \mathbf{E}_{k_x, k_y, -}^\perp(\omega, z) \\ & - \sum_{s=1,2} \mathbf{e}_s^\perp \mathbf{e}_s \cdot \left[\frac{i\omega^2}{2\epsilon_0 c^2 k_z} \mathbf{P}_{k_x, k_y}(\omega, z) - \frac{\omega}{2\epsilon_0 c^2 k_z} \mathbf{J}_{k_x, k_y}(\omega, z) \right]. \end{aligned} \quad (89)$$

This pair of equation is exact and completely analogous to the pair of z -propagated equations discussed in the previous section. Because the nonlinear polarization in these equations results as a response to the *complete* electric field, they cannot be used to calculate the forward field in isolation (i.e. without its backward propagating counterpart). The equation becomes unidirectional only when the following approximation can be adopted:

$$\mathbf{P}(\mathbf{E}), \mathbf{J}(\mathbf{E}) \rightarrow \mathbf{P}(\mathbf{E}_f), \mathbf{J}(\mathbf{E}_f). \quad (90)$$

In other words, to obtain a closed system *which is restricted to a single direction*, we must require that nonlinear polarization can be calculated accurately from only

the forward propagating field. This means that UPPE is only applicable when the back-reflected portion of the field is so small that its contribution to the nonlinearity can be neglected. Note that this assumption is inherent in any one-way propagating pulse evolution equation. Since it is the only approximation required for the UPPE, it should not be surprising that all other pulse propagation models can be derived from the UPPE by adopting further approximations.

2.3.4 z -propagated UPPE: Simplified, practical version

Equation (88), with nonlinear polarization approximated by Eq. (90) can easily become a rather large system to solve numerically. This is especially true for experiments with wide-beam, multi-TW lasers. Fortunately, in most cases transverse dimensions of resulting structures remain relatively large in comparison to wavelength, and further approximations are possible. For example in femtosecond filamentation in gases, the typical diameter of the filament core is about hundred microns which dimension is large in comparison with the laser wavelength. Consequently, the longitudinal vector component of the electric field is much smaller than the transverse (x, y) components, and can be neglected in calculation of the nonlinear medium response. It thus makes sense to take advantage of this fact to obtain a simpler equation.

Concretely, one can neglect the z components of the field and polarization vectors. In such a situation the sum over polarization vectors reduces approximately to unity

$$\sum_{s=1,2} \mathbf{e}_s^\perp \mathbf{e}_s \approx 1. \quad (91)$$

To see this, it is enough to recall that the left-hand side constitutes a projector onto the wave-vector (recall that these vectors are mutually orthogonal). As the wave-vector is pointing in the direction almost parallel to the beam axis, it is also approximately a unity *operator* in the vector subspace spanned by x, y .

Replacing the transverse projection by unity, the full UPPE simplifies into an equation for transverse component(s)

$$\begin{aligned} \partial_z E_{k_x, k_y}(\omega, z) &= ik_z E_{k_x, k_y}(\omega, z) + \frac{i\omega^2}{2\epsilon_0 c^2 k_z} P_{k_x, k_y}(\omega, z) - \frac{\omega}{2\epsilon_0 c^2 k_z} J_{k_x, k_y}(\omega, z), \\ k_z &= \sqrt{k^2(\omega) - k_x^2 - k_y^2}. \end{aligned} \quad (92)$$

This is the most useful form for practical calculation, and is therefore called simply UPPE. While we write it as a scalar equation, it should be understood that it is in general coupled to its counterpart governing the other polarization. The two polarization components of the electric field both contribute to the nonlinear polarization and this is how they become mutually coupled.

2.3.5 Other propagation models as approximations of UPPE

The previous section showed that Unidirectional Pulse Propagation Equations can be rigorously derived under a very general assumption that nonlinear interaction between light and matter occurs in a regime which makes it possible to calculate the nonlinear medium response with sufficient accuracy only from the forward-propagating field component. Because this is how *all* one-way pulse propagation equation treat the nonlinearity, one can expect that other types of equations can be derived from UPPE. In fact, a universal scheme to derive all other propagation models can be given.

Several types of unidirectional propagation equation appear frequently in the literature on nonlinear optics. The most important examples are Non-Linear Schrödinger (NLS) equation [18], Nonlinear Envelope Equation [17] (NEE), the First-Order Propagation equation [14] (FOP), Forward Maxwell's Equation [11] (FME), and several other equations that are closely related to these. All of these can be understood as approximations to the UPPE.

The unified derivation procedure, described in detail in Ref. [5], brings various propagation equations under one roof, and elucidates exactly what approximations must be assumed to justify their original derivations. This allows us to compare physical assumptions and approximations underlying different equations. It also reveals relations between equations which may not be obvious either because of their apparently different form, or because of different methods used in the original derivations.

It is instructive to break the derivation procedure into several steps. As a first step, we adopt a scalar, one-component approximation and write the Unidirectional Pulse Propagation Equation in the canonical form:

$$\partial_z E_{k_x, k_y}(\omega, z) = iK_z E_{k_x, k_y}(\omega, z) + iQ \frac{P_{k_x, k_y}(\omega, z)}{2\epsilon_0} \quad (93)$$

where

$$K_z(k_x, k_y, \omega) = \sqrt{k^2(\omega) - k_x^2 - k_y^2} \quad (94)$$

and

$$Q(k_x, k_y, \omega) = \frac{\omega^2}{c^2 K_z(k_x, k_y, \omega)} \quad (95)$$

will be called nonlinear coupling. In most cases, the concrete form of the nonlinear polarization P is unimportant, and we will assume that it can be specified in terms of an algorithm which accepts the electric field (in general as a function of time at a given spatial location) as input.

Let us note that this one-component, or scalar representation can be still understood as a description of a single polarization in a coupled system describing two transverse vector components of an optical field. While each equation appears scalar, the two become coupled through the polarization term, for example due to the nonlinear birefringence. These coupling effects can play a role even if a laser beam is much wider than the light wavelength, and can lead to a rich polarization dynamics within femtosecond filaments. What *is* neglected at this step is the longitudinal part of the electric field. That only becomes important when the beam focuses to a size comparable with wavelength. However, in the naturally occurring filaments, i.e., without focusing by short focal-length optical elements, such extreme focusing is never achieved, because self-focusing collapse is always arrested either by chromatic dispersion [30] or by the free-electron induced de-focusing [8, 31]. Thus, for many practical purposes, the above representation is sufficiently rich and accurate.

In the second derivation step, we replace couplings K_z and Q by suitable approximations. In most cases, they are closely related to Taylor expansions in frequency and in transverse wave numbers. It is at this stage that artificial parameters are introduced into a propagation model (a typical example is the reference frequency). It is important to keep in mind that information extracted from simulations should not depend on such degrees of freedom. In this respect, the improvements introduced into various pulse evolution equations can be viewed as corrections which (partially) restore the invariance of the model with respect to these choices.

Having specified approximations for the linear and nonlinear coupling, we are still in the real-field representation. However, most of the published models are written

using envelopes. Thus, in the next step, we obtain *envelope* equations. To do this, one can express the field in terms of an envelope by factoring out the carrier wave at a chosen reference angular frequency ω_r with the corresponding wave-vector $k_r = K_z(0, 0, \omega_r)$:

$$E(\mathbf{r}, t, z) = \mathcal{A}(\mathbf{r}, t, z)e^{i(k_r z - \omega_r t)}. \quad (96)$$

A similar factorization is of course introduced for the nonlinear polarization $P(\mathbf{r}, t, z)$ as well.

The final step consists in transforming the equation from the spectral- to the real-space representation. Mathematically, this is nothing but a Fourier transform, and the following standard replacement rules for differential operators provide quick and easy way to do this transformation:

$$ik_x \rightarrow \partial_x \quad ik_y \rightarrow \partial_y \quad (\omega - \omega_R) \rightarrow i\partial_t \quad \partial_z \rightarrow ik(\omega_R) + \partial_z. \quad (97)$$

Finally, in most cases we also transform to a frame moving with a suitable group velocity such that the pulse remains close to the center of the computational domain. We invite the reader to consult reference [5] which shows details of application of this method to several examples of propagation equations. Also note that the above procedure is closely related to that described in Section 2.2, where the Nonlinear Envelope Equation was derived from the Forward Maxwell Equation.

2.4 Medium response and nonlinear interactions

This section describes typical components of medium response models in nonlinear optics of ultrashort pulses. They all can be viewed as contributions to the polarization or to the induced current density, both of which appear in Maxwell's equations or in the wave equation as source terms.

2.4.1 Optical Kerr effect

We will use the optical Kerr effect as a prototypical example of nonlinear source term that can be included in the polarization. At the dominant third order for a centro-symmetric medium, the nonlinear polarization \mathbf{P} reads:

$$\mathbf{P} \equiv \epsilon_0 \chi^{(3)} \mathbf{E}^3. \quad (98)$$

By expressing the scalar components of the electric field as an envelope and a carrier: $E = \frac{1}{2}[\mathcal{E} \exp(ik_0 z - i\omega_0 t) + \mathcal{E}^* \exp(-ik_0 z + i\omega_0 t)]$, we obtain an expression for E^3 :

$$E^3 = \frac{1}{8}[\mathcal{E}^3 \exp(i3k_0 z - i3\omega_0 t) + 3|\mathcal{E}|^2 \mathcal{E} \exp(ik_0 z - i\omega_0 t) + \text{c.c.}], \quad (99)$$

where c.c. denotes complex conjugation. By introducing Eq. (99) into Eq. (98), we identify the nonlinear polarization envelope \mathcal{P} from its carrier envelope decomposition $P = \frac{1}{2}[\mathcal{P} \exp(ik_0 z - i\omega_0 t) + \mathcal{P}^* \exp(-ik_0 z + i\omega_0 t)]$:

$$\mathcal{P} \equiv \epsilon_0 \chi^{(3)} \frac{3}{4} |\mathcal{E}|^2 \mathcal{E}. \quad (100)$$

It is readily seen that Equation (99) contains a component oscillating at the third harmonic ($3\omega_0$) that has been discarded in the nonlinear polarization, as we only identified the fundamental components oscillating at ω_0 to derive the nonlinear polarization envelope (100). Thus, introduction of Eq. (100) in an envelope propagation

model describes the effects called self-focusing (for a positive $\chi^{(3)}$) and self-phase modulation but not third-harmonic generation. Next section will show how to describe the latter effect either with an envelope or a carrier resolving propagation equation.

Up to now, we have written our models with *hidden* material coefficients such as, e.g., the linear susceptibility $\chi^{(1)}(\omega)$ which is included in the dispersion relation $k(\omega)$ of the medium, in turn involving specific resonance frequencies and amplitudes. For practical situations, it is needed to supply numerical codes with parameter values for the material coefficients. For the nonlinear third-order susceptibility, values may be obtained from ab-initio calculations but measurements of the nonlinear index coefficient $n_2 \equiv 3\chi^{(3)}/4\epsilon_0 c n_0^2$ in units of m^2/W may also be found in the literature. For instance, see Refs. [27] for optical crystals. By introducing the above definition for the nonlinear index coefficient n_2 in Eq. (100), and by using the definition of the intensity $\mathcal{I} \equiv \epsilon_0 c n_0 |\mathcal{E}|^2/2$, an expression is obtained for the nonlinear polarization envelope modeling an instantaneous Kerr response of the medium due to the electronic contribution to the polarization:

$$\frac{\mathcal{P}}{\epsilon_0} \equiv 2n_0 n_2 \mathcal{I} \mathcal{E}, \quad (101)$$

where both the linear refraction index n_0 and the nonlinear index $n_2 \mathcal{I}$ are dimensionless, since \mathcal{I} is expressed in W/m^2 and n_2 in m^2/W . Eq. (101) can then be introduced into all nonlinear envelope propagation equations. Using for instance Eq. (54) to describe the propagation of a monochromatic beam, which allows us to neglect dispersion ($k_0^{(2)} = 0$), we obtain the NLS equation with its standard cubic nonlinearity:

$$\frac{\partial \mathcal{E}}{\partial z} = \frac{i}{2k_0} \Delta_{\perp} \mathcal{E} + i \frac{\omega_0}{c} n_2 \mathcal{I} \mathcal{E} \quad (102)$$

Equation (102) models beam propagation under the effects of diffraction and the optical Kerr effect, leading to beam self-focusing (for a positive n_2), i.e. to the cumulative lens effect bending the phase fronts due to the higher refraction index in the most intense part of the beam. In a planar geometry, beam self-focusing and diffraction alternatively prevail, resulting in beam width oscillations without energy losses [28]. In cylindrical geometry, it is known that Eq. (102) is mathematically singular: Beams with power above a certain threshold P_{cr} undergo catastrophic collapse at a finite distance [29]. For Gaussian beams, this critical threshold is given by:

$$P_{\text{cr}} = \frac{3.77\pi n_0}{2k_0^2 n_2}. \quad (103)$$

For a collimated Gaussian beam $\mathcal{E} = \mathcal{E}_0 \exp(-r^2/w_0^2)$ of power $P_{\text{in}} \equiv \pi w_0^2 \mathcal{I}_0/2$, where $\mathcal{I}_0 \equiv \epsilon_0 c n_0 \mathcal{E}_0^2/2$, the self-focusing (collapse) distance follows [29]:

$$z_c = \frac{0.367 z_R}{\sqrt{[(P_{\text{in}}/P_{\text{cr}})^{1/2} - 0.852]^2 - 0.0219}} \quad (104)$$

where $z_R \equiv k_0 w_0^2/2$ denotes the Rayleigh (typical diffraction) length. Section 3.1.2 shows how to implement model (102) and Eqs. (103) and (104) provide analytical scaling laws for the collapse distance and the critical power threshold that can be used as test cases to check the correct implementation of the model.

2.4.2 Optical Kerr effect and third harmonic generation

Closely related to the optical Kerr effect caused by electrons in bound states is third harmonic generation which is often observed in femtosecond filaments. In fact, from a certain point of view the two effects are actually one.

Consider an instantaneous (electronic) Kerr effect in an isotropic medium. Also consider a propagation model which simulates directly the physical field rather than its envelope. A polarization response that is third-order in the electric field E must be constructed solely from E taken at the given instant in time, so there is a single vector to work with. That is why, the only possible form of an *instantaneous* third-order nonlinearity is as given in Eq. (98).

Note that as soon as there is memory, two frequency dependent components of third-order susceptibility tensor are needed for full description. The important point is that the frequency content of Eq. (98) consists of both the fundamental frequency of E and of its third harmonic. This is the main source of third harmonic radiation observed in femtosecond filaments (although it is not the only one).

It is worthwhile to remark that Readers will find in the literature also a very different approach to modeling third-harmonic generation. In works and simulations based on application of envelope pulse propagation equations, several authors used two envelope functions, one for the fundamental frequency and one for the third harmonic generation [32,33]. The electric field decomposition into carriers and envelopes with these two components reads: $E = \frac{1}{2}[\mathcal{E}_{\omega_0} \exp(ik_{\omega_0}z - i\omega_0t) + \mathcal{E}_{3\omega_0} \exp(ik_{3\omega_0}z - i3\omega_0t) + \text{c.c.}]$, and the nonlinear polarization can be decomposed similarly. Introduction of this decomposition into Eq. (98) yields expressions for the fundamental and third harmonic envelope components of the nonlinear polarization:

$$\mathcal{P}_{\omega_0} = \epsilon_0 \chi^{(3)} \frac{3}{4} [(|\mathcal{E}_{\omega_0}|^2 + 2|\mathcal{E}_{3\omega_0}|^2)\mathcal{E}_{\omega_0} + \mathcal{E}_{\omega_0}^{*2}\mathcal{E}_{3\omega_0}], \quad (105)$$

$$\mathcal{P}_{3\omega_0} = \epsilon_0 \chi^{(3)} \frac{3}{4} [(|\mathcal{E}_{3\omega_0}|^2 + 2|\mathcal{E}_{\omega_0}|^2)\mathcal{E}_{3\omega_0} + \mathcal{E}_{\omega_0}^3/3]. \quad (106)$$

For each component \mathcal{P}_{ω_0} and $\mathcal{P}_{3\omega_0}$, the first two terms represent self- and cross-phase modulation. The third terms are responsible for energy exchange between fundamental and third harmonic fields, namely third harmonic generation and back conversion. An envelope propagation equation for each component \mathcal{E}_{ω_0} and $\mathcal{E}_{3\omega_0}$ is derived following the methods presented in section 2.2 and follow the canonical form valid for envelopes with broad spectra.

It has to be emphasized that the two-envelope method can only be justified as long as spectral components centered around the fundamental and third harmonic frequency are well separated. However, spectra can become extremely broad in femtosecond filamentation. Then, distinction between fundamental and third harmonic is impossible, and any two-envelope parametrization is therefore non-unique leading to a fundamentally inconsistent model. Thus, if harmonic frequencies are expected to appear in the numerical experiment and if the spectrum for the fundamental component broadens sufficiently to overlap the third harmonic spectrum, a carrier resolving model implementing the optical Kerr effect as in (98) should be used. This will naturally capture also generation of other odd harmonics in a cascade process which may become important for longer-wavelength filamentation.

2.4.3 Nonlinear absorption

The NLS Equation (102) leads to optical beam collapse in cylindrical geometry but in a real experiment, saturation mechanisms prevent collapse to occur [31]. This means that the mathematical singularity of Eq. (102) must be cured by extending the model to a more realistic case. Close to the collapse, the beam intensity is sufficient to ionize the medium after absorption of several photons. The process is associated with

nonlinear absorption of energy, which is the main physical effect playing a saturation role in preventing the collapse to occur⁷.

Nonlinear absorption is described by an effective current \mathbf{J} such that the averaged dissipated power corresponds to that necessary for optical field ionization of the medium with density of neutral atoms ρ_{nt} , ionization potential (or gap for a solid medium) U_i and intensity-dependent ionization rate $W(\mathcal{I})$ [35]. Different ionization regimes exist and correspond to different ionization rates. For example for intensities smaller than a certain threshold, ionization occurs in the multiphoton regime and requires absorption of several (K) photons to liberate an electron. In this paper, without loss of generality, we will consider only the multiphoton regime for which a simple law for ionization rates reads $W(\mathcal{I}) = \sigma_K \mathcal{I}^K$, where σ_K denotes the cross section for multiphoton ionization. The above condition for power dissipation is expressed as

$$\frac{1}{2} \mathbf{J} \cdot \mathbf{E}^* = W(\mathcal{I}) K \hbar \omega_0 \rho_{nt}. \quad (107)$$

The current is therefore obtained as

$$\frac{\mathbf{J}}{\epsilon_0 c} = n_0 \frac{W(\mathcal{I}) K \hbar \omega_0 \rho_{nt}}{\mathcal{I}} \mathbf{E}, \quad (108)$$

and its envelope counterpart, in the multiphoton regime, reads as

$$\frac{\mathcal{J}}{\epsilon_0 c} = n_0 \beta_K \mathcal{I}^{K-1} \mathcal{E}, \quad (109)$$

where $\beta_K \equiv K \hbar \omega_0 \sigma_K \rho_{nt}$ denotes the cross section for multiphoton absorption.

By introducing Eq. (109) into the nonlinear envelope equations derived in section 2.2, the effect of multiphoton absorption is accounted for in propagation models. For instance, with the change $\mathcal{P} \rightarrow \mathcal{P} + i\mathcal{J}/\omega_0$ the NLS Equation (54) for a monochromatic beam undergoing diffraction, optical Kerr effect and multiphoton absorption becomes:

$$\frac{\partial \mathcal{E}}{\partial z} = \frac{i}{2k_0} \Delta_{\perp} \mathcal{E} + i \frac{\omega_0}{c} n_2 \mathcal{I} \mathcal{E} - \frac{\beta_K}{2} \mathcal{I}^{K-1} \mathcal{E}. \quad (110)$$

Equation (110) is an extended NLS equation that is also valid to describe the propagation of pulses provided they keep a narrow spectrum during their nonlinear propagation.

An evolution equation for the pulse intensity is obtained by multiplying Eq. (110) by \mathcal{E}^* and by adding the result to its complex conjugate:

$$\frac{\partial |\mathcal{E}|^2}{\partial z} = \frac{i}{2k_0} [\mathcal{E}^* \Delta_{\perp} \mathcal{E} - \mathcal{E} \Delta_{\perp} \mathcal{E}^*] - \beta_K \mathcal{I}^{K-1} |\mathcal{E}|^2. \quad (111)$$

Note that the Kerr term is no longer present in Eq. (111), reflecting the fact that the optical Kerr effect does not directly modify the laser beam intensity but leads to nonlinear phase accumulation. Spatial phase gradients mediated by the first term on the r.h.s. of Eq. (111) then lead to an energy flux toward the beam center, which is responsible for an increase of the beam intensity. For a very large beam, the term $[\mathcal{E}^* \Delta_{\perp} \mathcal{E} - \mathcal{E} \Delta_{\perp} \mathcal{E}^*]$ can be neglected in the central part of the beam⁸, the intensity of which is governed by:

$$\frac{\partial \mathcal{I}}{\partial z} = -\beta_K \mathcal{I}^K. \quad (112)$$

⁷ Note that plasma induced defocusing can also prevent collapse to occur, however, nonlinear absorption of energy is necessary to prevent subsequent catastrophic behavior [34].

⁸ By denoting ϕ the phase of the beam, a straightforward calculation shows that $[\mathcal{E}^* \Delta_{\perp} \mathcal{E} - \mathcal{E} \Delta_{\perp} \mathcal{E}^*] = 2i \nabla_{\perp} \cdot (|\mathcal{E}|^2 \nabla_{\perp} \phi)$. For a large beam, this term is small close to the beam center where the phase is flat.

An analytical solution of Eq. (112) reads

$$\mathcal{I}(z) = \frac{\mathcal{I}_0}{(1 + (K - 1)\beta_K \mathcal{I}_0^{K-1} z)^{1/(K-1)}}. \quad (113)$$

Tests of the numerical implementation of nonlinear energy losses can be easily made by comparison of simulation results with their analytical counterpart from Eq. (113).

2.4.4 Plasma generation and plasma defocusing

When the pulse is so intense that it ionizes the medium, the contribution of the plasma follows from the evolution equation for the plasma current density:

$$\frac{\partial \mathbf{J}}{\partial t} + \frac{\mathbf{J}}{\tau_c} = \frac{q_e^2}{m_e} \rho \mathbf{E}, \quad (114)$$

where ρ denotes the electron density and τ_c is the electron collision time. Equation (114) can be solved in the Fourier domain and its solution introduced in propagation equations with a source term $(\omega/c)(\hat{J}/\epsilon_0 c)$ involving spectral components of the free charge current. From Eq. (114), we obtain:

$$\frac{\omega}{c} \frac{\hat{\mathbf{J}}}{\epsilon_0 c} = \frac{q_e^2 \omega \tau_c}{\epsilon_0 c^2 m_e} \frac{1 + i\omega \tau_c}{1 + \omega^2 \tau_c^2} \widehat{\rho \mathbf{E}}. \quad (115)$$

We rewrite Eq. (115) as:

$$\frac{\omega}{c} \frac{\hat{\mathbf{J}}}{\epsilon_0 c} = k(\omega) \sigma(\omega) \widehat{\rho \mathbf{E}}, \quad (116)$$

where

$$\sigma(\omega) = \frac{\omega_0}{n(\omega) c \rho_c} \frac{\omega_0 \tau_c (1 + i\omega \tau_c)}{(1 + \omega^2 \tau_c^2)} \quad (117)$$

is a complex frequency-dependent coefficient with real part equal to the cross section for inverse Bremsstrahlung [36] and $\rho_c \equiv \epsilon_0 m_e \omega_0^2 / q_e^2$, the critical plasma density above which the plasma becomes opaque to the laser beam at frequency ω_0 . This is known as the Drude model. Note that $\sigma(\omega)$ is not effectively depending on the central frequency of the laser pulse ω_0 since the quantity ω_0^2 / ρ_c in Eq. (117) is a constant, the critical density being only a reference chosen for the pulse central frequency ω_0 .

The current in Equation (116) accounts for plasma absorption (real part) and plasma defocusing (imaginary part). Both effects are frequency dependent, for example defocusing is stronger for longer wavelengths. It can be important that our models capture such dispersive behavior, for example in pump probe experiments with different pulse wavelengths.

To close the model, one needs to know the evolution of the electron density $\rho(\mathbf{r}, t)$ entering in Eq. (116). It is governed by a rate equation in the form:

$$\frac{\partial \rho}{\partial t} = W_{\text{ofi}}(\mathcal{I})(\rho_{\text{nt}} - \rho) + W_{\text{ava}}(\mathcal{I})\rho \quad (118)$$

where the first term on the r.h.s. of Eq. (118) represents optical field ionization and the second term represents avalanche ionization. As stated in section 2.4.3, optical field ionization in the multiphoton regime occurs with a rate $W_{\text{ofi}}(\mathcal{I}) = \sigma_K \mathcal{I}^K$. The rate for avalanche ionization can be considered as proportional to the pulse intensity $W_{\text{ava}}(\mathcal{I}) = \sigma(\omega_0) \mathcal{I} / U_i$, where $\sigma(\omega_0)$ is the inverse Bremsstrahlung coefficient given by

Eq. (117) evaluated at the central frequency ω_0 of the laser pulse and U_i the ionization potential.

An example of nonlinear envelope equation with nonlinear terms accounting for the optical Kerr effect, nonlinear absorption and plasma effects is obtained by introducing the corresponding source terms in the FEE (41):

$$\frac{\partial \hat{\mathcal{E}}}{\partial z} = \frac{i}{2k(\omega)} \Delta_{\perp} \hat{\mathcal{E}} + i[k(\omega) - \kappa(\omega)] \hat{\mathcal{E}} + i \frac{\omega}{c} \frac{n_0}{n(\omega)} n_2 \widehat{\mathcal{I} \mathcal{E}} - \frac{\beta_K}{2} \widehat{\mathcal{I}^{K-1} \mathcal{E}} - \frac{\sigma(\omega)}{2} \widehat{\rho \mathcal{E}}. \quad (119)$$

2.4.5 Raman-Kerr effect

The optical Kerr effect includes in general the electronic contribution which is nearly instantaneous and a delayed component of fraction α , due to stimulated molecular Raman scattering.

Air is by a large part made of two-atomic molecules with different polarizabilities parallel and perpendicular to their symmetry axes. This leads to a nonlinear effect which is referred to as stimulated Raman effect, although the recent nomenclature acknowledges the fact that dynamic reorientation of molecules plays a central role in it.

The interaction energy of a molecule in an external field is such that it prefers to align with the direction of the field. When a femtosecond pulse hits such a molecule, it excites rotational motion; this is a stimulated Raman effect. Molecular rotation then changes the effective linear polarizability of the molecule as projected on the direction of the field. Because the interaction Hamiltonian is quadratic in field, the effect is of third-order. It is therefore often considered a companion of the electronic Raman effect. Taken a very different microscopic origin, this may seem arbitrary, but one has to keep in mind that manifestations of the two effects (i.e. self-focusing) are very difficult to distinguish in longer pulses.

A proper, first-principles model would need to integrate quantum mechanical equations of motion for a density matrix describing the rotational state of an ensemble of molecules. Note that such a system is to be solved at each spatial grid location, and at each propagation step! Instead of this (relatively) difficult calculation, the Raman effect is approximately parametrized as described next.

Let us denote Q_i a generalized coordinate of an effective oscillator *embedded* in the medium which responds to a force that is quadratic in external field,

$$\frac{\partial^2 Q_i}{\partial t^2} + 2\Gamma \frac{\partial Q_i}{\partial t} + (\omega_R^2 + \Gamma^2) Q_i = (\omega_R^2 + \Gamma^2) |\mathcal{E}(r, t, z)|^2, \quad (120)$$

for Q_i with boundary conditions $\partial Q_i / \partial t(-\infty) = 0$ and $Q_i(-\infty) = 0$. The solution to Eq. (120) reads:

$$Q_i(r, t, z) = \int_{-\infty}^t \mathcal{R}_0 \exp[-\Gamma(t - \tau)] \sin[\omega_R(t - \tau)] |\mathcal{E}(r, \tau, z)|^2 d\tau, \quad (121)$$

where $\mathcal{R}_0 = (\Gamma^2 + \omega_R^2) / \omega_R$.

The nonlinear polarization for the Kerr term with its Raman contribution therefore reads as

$$\frac{\mathcal{P}}{\epsilon_0} = 2n_0 n_2 \left((1 - \alpha) \mathcal{I}(r, t, z) + \alpha \int_{-\infty}^t \mathcal{R}(t - \tau) \mathcal{I}(r, \tau, z) d\tau \right) \mathcal{E}, \quad (122)$$

where $\mathcal{I} = \epsilon_0 c n_0 |\mathcal{E}(r, t, z)|^2 / 2$. The function $\mathcal{R}(t)$ mimics the molecular response with a characteristic time Γ^{-1} and frequency ω_R :

$$\mathcal{R}(t) = \mathcal{R}_0 \exp(-\Gamma t) \sin \omega_R t \quad (123)$$

One advantage of the above phenomenological approach is that it can be applied also to other types of stimulated Raman scattering. For example in glasses, this single-oscillator model can serve as an acceptable approximation of what is actually a significantly more complex process. It can also be generalized to include multiple effective oscillators, which in turn can mimic the true medium response quite accurately. In water, the single-oscillator model could accurately reproduce measured signatures of stimulated Raman scattering in angularly resolved spectra [37, 38]. We will discuss efficient numerical implementation of this and similar models in Sect. 3.3.

3 Implementation of propagation models

This section is devoted to a presentation of the numerical implementation of propagation equations. As shown in the previous section, a canonical form exists for all unidirectional propagation equations. This form has the same structure for envelope and for carrier-resolving equations, opening the question of the possibility for a universal scheme and solver. A numerical scheme valid for the UPPE should indeed apply for solving all other equations. However, there are a few distinguishing features in the propagation equations in the canonical form making worth presenting different schemes. First, carrier-resolving propagation equations involve real fields as in Maxwell equations, whereas envelope equations deal with complex envelopes. This implies slight differences in treating the spectra of real fields compared to complex envelope spectra. Second, nonparaxiality is one of the distinguishing features of the UPPE, making necessary to solve that equation in the three-dimensional spectral domain for frequency and wave numbers, whereas alternatives exist for paraxial equations, be they propagating envelopes or fields. At the price of a loss of universality, paraxial equations can indeed be solved by finite difference methods in the spatial domain, by space marching each frequency component after a one-dimensional temporal to spectral Fourier transform. We adopt a presentation covering both options with a first section devoted, but not restricted to paraxial envelope equations. We will start by the simplest propagation equation which describes diffraction of a laser beam as this provides the basic building block of the general scheme valid for all paraxial propagation equations. We then consider resolution of the UPPE in Fourier space, which apply in general to nonparaxial, carrier-resolving or envelope, propagation equations.

The generic form of the considered propagation equations is retrieved in models for different physical problems, therefore the methods we describe apply as well in different fields. The reader is referred to [39] and reference therein for a review of numerical schemes we apply to propagation equations.

3.1 Envelope propagation models

In this section, we consider paraxial envelope equations. The proposed implementation methods extend in a straightforward way to paraxial carrier-resolving equations, thus without loss of generality, we restrict the presentation to complex envelopes.

3.1.1 Diffraction

Diffraction occurs in all media and even in vacuum. Not surprisingly, the structure of the diffraction operator as a product of a frequency dependent coefficient and a

transverse Laplacian acting only on transverse coordinates is the common feature of all paraxial envelope or carrier-resolving propagation equations. Implementing diffraction therefore serves as a basic building block for all paraxial equations. We first consider monochromatic beams, i.e. a sufficiently long laser pulse with central wave number k_0 and a narrow spectrum so that all frequency dependence can be neglected. Diffraction of the monochromatic beam is described by the paraxial equation

$$\frac{\partial \mathcal{E}}{\partial z} = \frac{i}{2k_0} \Delta_{\perp} \mathcal{E}. \quad (124)$$

We start by describing beam propagation in 1+1 dimensions, i.e., one transverse dimension and one evolution (or propagation) variable z . We will consider either a planar geometry with transverse direction x , or a cylindrical geometry with revolution symmetry, with a radial transverse variable $r \equiv \sqrt{x^2 + y^2}$. From the point of view of the computational cost, the revolution symmetry is an interesting geometry for propagating a laser beam when it does not break-up into multiple beamlets since its cost corresponds to that of a 1-dimensional numerical method. In this section \mathcal{E} is therefore assumed to depend only on the transverse variable x or r , and the evolution variable z . The transverse Laplacian operator is therefore reduced to $\Delta_{\perp} \equiv \partial^2/\partial x^2$ in the planar geometry, or to $\Delta_{\perp} \equiv \partial^2/\partial r^2 + (1/r)\partial/\partial r$ in cylindrical geometry. To avoid redundancy, we will use r as a transverse variable but switching from cylindrical to planar geometry can be implemented in a single generic tool: Unless otherwise stated, all formulas are the same for both geometries with $r \leftrightarrow x$. We will specify minor differences between planar and cylindrical geometry by using x instead of r only where it is necessary.

Initial condition. The propagation starts at $z = 0$ where the beam amplitude and phase profiles are known, e.g., the beam has a Gaussian shape with quadratic spatial phase modeling a flat-phase beam having passed through a lens of focal length f :

$$\mathcal{E}(r, z = 0) = \mathcal{E}_0 \exp \left(-\frac{r^2}{w_0^2} - i \frac{k_0 r^2}{2f} \right). \quad (125)$$

The quantities w_0 and \mathcal{E}_0 are the beam width and the initial amplitude.

Boundary conditions. Boundary conditions must also be specified to solve Equation (124). In free space, one usually requires that the field vanish far from the peak. The highest order derivative in Equation (124) is second order, thus two boundary conditions must be specified at the boundaries of the numerical grid $r = r_{\min}$ and $r = r_{\max}$. These depend on the type of beam one wants to model.

In a cylindrical geometry, standard beams have intensity with a zero-slope at the origin and vanish far from the origin, which gives the boundary conditions:

$$\left. \frac{\partial \mathcal{E}(r, z)}{\partial r} \right|_{r=0} = 0, \quad (126)$$

$$\mathcal{E}(r = r_{\max}, z) = 0. \quad (127)$$

In a planar geometry, the boundary conditions for a standard beam vanishing far from the peak read:

$$\mathcal{E}(x = x_{\min}, z) = 0, \quad (128)$$

$$\mathcal{E}(x = x_{\max}, z) = 0. \quad (129)$$

Boundary conditions (128) and (129) in a cylindrical grid would be suitable for the propagation of vortex beams (having a zero field and phase singularity at the origin).

On finite difference schemes. Finite difference scheme consist in representing the solution to the original PDE by its values at discrete set of points and replacing the PDE by a set of coupled equations for these discrete quantities. In practice, we discretize the transverse variable r to form a numerical grid of finite size. For a uniform grid with $N_\perp + 2$ grid points, i.e., N_\perp inner points and 2 boundaries. We define $r_j = r_{\min} + j\Delta r$, $j = 0 \dots N_\perp + 1$ and the step-size $\Delta r = (r_{\max} - r_{\min})/(N_\perp + 1)$. For a cylindrical geometry $r_{\min} = 0$. Similarly to the discretization of the transverse variable, we will describe the propagation over a distance z_{\max} by making steps $z_n = n\Delta z$, $n = 0 \dots N_z$ of constant size Δz . Let E_j^n denote $\mathcal{E}(r = r_j, z = z_n)$.

A standard task of numerical analysis is to design robust algorithms, which have desirable properties including good *numerical stability*, *accuracy*, and *efficiency* with respect to computational time.

Discretization of PDEs is associated with local and global truncation errors due to the approximation of partial derivatives by their discretized versions. For example in Eq. (124), the evolution operator is discretized as:

$$\frac{\partial \mathcal{E}}{\partial z}(r = r_j, z = z_n) \simeq \frac{E_j^{n+1} - E_j^n}{\Delta z} + O(\Delta z), \quad (130)$$

which is first-order accurate in Δz . A second-order accurate discretization of the second-order space-derivative appearing in the transverse Laplacian reads:

$$\frac{\partial^2 \mathcal{E}}{\partial r^2}(r = r_j, z = z_n) \simeq \frac{E_{j+1}^n - 2E_j^n + E_{j-1}^n}{\Delta r^2} + O(\Delta r^2). \quad (131)$$

The *local truncation error* in the numerical solution is the error generated at a particular step, when the solution at the previous step is considered as exact (in practice, it is not exact, except if it corresponds to the initial condition). For example Eq. (131) gives a second order local truncation error. The cumulative error in the numerical solution to a PDE on an interval in the evolution variable is called the global truncation error and the order of accuracy is the order of the global truncation error.

Numerical stability refers to the fact that a numerical calculation does not amplify truncation or approximation errors. If approximation errors decay as the computation is carried forward, the numerical scheme is stable. If the errors grow, the numerical solution departs from the correct physical behavior of the modeled system and the numerical scheme is said to be unstable. The stability of finite difference schemes applied to linear partial differential equations can be commonly determined by a von Neumann stability analysis [40,41] which is based on the decomposition of the solution including the instability waves representing errors into Fourier series and a linear stability analysis of these waves. Depending on the numerical scheme, stability can require restrictive conditions on the step-sizes to be fulfilled. Scheme stability is in general difficult to investigate when the partial differential equations under consideration are nonlinear or nonuniform. Therefore, stability conditions on step-sizes associated with the linear-part of our canonical propagation equation may not be sufficient to ensure the stability of the complete scheme but constitute a good starting guess of the restrictions on the step sizes used in the scheme.

Implicit vs explicit schemes: Finite difference schemes are furthermore classified into *explicit* and *implicit* schemes. An explicit scheme allows for the calculation of quantities at each position J on the grid for the $(N+1)^{\text{th}}$ evolution variable, say E_j^{N+1} , explicitly from the previously known quantities E_j^n , $n = 0 \dots N$, $j = 0 \dots N_\perp + 1$. An implicit scheme requires the numerical resolution of implicit equations coupling E_j^{N+1}

for several j with the already known quantities in order to find E_j^{N+1} for all j , and are computationally more expensive. However, the efficiency of a calculation must be evaluated with stability constraints in mind. Explicit finite difference schemes for solving Eq. (124) are associated with very restrictive stability conditions in the form $\Delta z \ll k_0 \Delta r^2$, ruining the advantage of an explicit scheme [41]. We leave it to the reader to analyze the details in Ref. [41] and we will directly present a resolution method based on an implicit method, namely the Crank-Nicolson method [42], the computational cost of which is balanced by the fact that it is unconditionally stable and allows us to replace many small explicit steps by a single large implicit step to advance the solution.

Crank-Nicolson method. A standard and efficient scheme to perform numerical simulations of Eq. (124) and equations having the same structure, as e.g. Eq. (21), is the Crank-Nicolson scheme [42]. It is an implicit, unconditionally stable numerical scheme that is second order accurate in both Δr and Δz .

Below, Δ_j denotes the discretized diffraction operator defined as

$$\Delta_j E_j^n \equiv E_{j-1}^n - 2E_j^n + E_{j+1}^n + \frac{\nu}{2j}(E_{j+1}^n - E_{j-1}^n), \quad (132)$$

where $\nu = 0$ for planar geometry and $\nu = 1$ for cylindrical geometry. Δ_j can be formally represented as a tridiagonal matrix acting on the vector E_j^n , with $j = 0 \dots N_\perp + 1$.

$$\Delta_j E_j^n = \begin{pmatrix} -2 & v_0 & 0 & \cdots & \cdots & 0 & 0 \\ u_1 & -2 & v_1 & 0 & \cdots & 0 & 0 \\ 0 & \ddots & \ddots & \ddots & 0 & 0 & 0 \\ 0 & 0 & u_j & -2 & v_j & 0 & 0 \\ 0 & 0 & 0 & \ddots & \ddots & \ddots & 0 \\ 0 & \cdots & \cdots & 0 & u_{N_\perp} & -2 & v_{N_\perp} \\ 0 & \cdots & \cdots & \cdots & 0 & u_{N_\perp+1} & -2 \end{pmatrix} \begin{pmatrix} E_0^n \\ E_1^n \\ \vdots \\ E_j^n \\ \vdots \\ E_{N_\perp}^n \\ E_{N_\perp+1}^n \end{pmatrix} \quad (133)$$

where $u_j = 1 - \nu/2j$ and $v_j = 1 + \nu/2j$. At this stage, note that u_0 and v_0 are ill-defined for a cylindrical geometry. In fact, the coefficients in the first and last lines of the matrix Δ_j will be replaced later to take boundary conditions into account. We therefore assume $v_0 = 1$ for both planar and cylindrical geometries.

The Crank-Nicolson scheme consists in discretizing the evolution operator in Eq. (124) as $\partial_z \mathcal{E}(r = r_j, z = z_n) = (E_j^{n+1} - E_j^n)/\Delta z$, thus it is centered at step $n + 1/2$. On the right hand side of Eq. (124), the diffraction operator is discretized and applied to the average of the field at distance n and $n + 1$ so as to center the scheme at step $n + 1/2$. This yields the implicit equation:

$$E_j^{n+1} - E_j^n = i\delta(\Delta_j E_j^{n+1} + \Delta_j E_j^n) \quad (134)$$

where $\delta = \Delta z/4k_0(\Delta r)^2$. The solution of Eq. (134) formally reads as

$$E_j^{n+1} = (1 - i\delta\Delta_j)^{-1}(1 + i\delta\Delta_j)E_j^n, \quad (135)$$

or equivalently:

$$L_- E_j^{n+1} = L_+ E_j^n \quad (136)$$

and requires multiplication of the tridiagonal complex matrix $L_+ \equiv 1 + i\delta\Delta_j$ by the vector E_j^n , inversion of the tridiagonal complex matrix $L_- \equiv 1 - i\delta\Delta_j$ and multiplication of L_-^{-1} by $L_+ E_j^n$. The above definition of matrix L_+ and L_- must be

modified to take into account the boundary conditions. Equation (135) allows for space marching the field over one propagation step. Applying it repeatedly for N_z steps will thus propagate the input field $E_j^{n=0}$ over a distance $N_z \Delta z$, where $E_j^{n=N_z}$ is obtained. Without modifications, the first line ($j = 0$) of Equation (135) reads as $(1+2i\delta)E_0^1 - i\delta v_0 E_1^1 = (1-2i\delta)E_0^0 + i\delta v_0 E_1^0$, which does not match the discretized version of the boundary condition (126): $E_0^1 = 0$, or that of (126). Boundary conditions can be simply enforced by rewriting this first line of L^- as $(1, 0, 0, \dots, 0)$ for the planar geometry, or as $(1, -1, 0, \dots, 0)$ for the circular geometry, and the first line of L^+ as $(0, \dots, 0)$ in both cases. In circular geometry, this ensures that a first-order-accurate discretized version of Eq. (126) is satisfied: $(E_1^1 - E_0^1)/\Delta r = 0$. An implementation of the boundary condition should at least match the order of the inner scheme. Introducing a ghost value E_{-1} at $r = -\Delta r$ and a second-order-accurate version of Eq. (126): $(E_1^1 - E_{-1}^1)/2\Delta r = 0$ together with the discretization introduced in the scheme for inner grid points (135) allows us to eliminate the ghost value and preserve the overall second order accuracy of the scheme. The first lines of L^\pm are obtained by identifying the coefficients of: $(1+4i\delta)E_0^1 - 4i\delta E_1^1 = (1-4i\delta)E_0^0 + 4i\delta E_1^0$. The last lines of L^- and L^+ are treated similarly to enforce boundary condition (127). Thus, the complex matrix L^- and L^+ including proper treatment of boundary conditions reads:

$$L_+ E_j^n = \begin{pmatrix} d_{0,+}^{(o)} & d_{1,+}^{(o)} & 0 & 0 & 0 & 0 & 0 \\ i\delta u_1 & 1-2i\delta & i\delta v_1 & 0 & 0 & 0 & 0 \\ 0 & \ddots & \ddots & \ddots & 0 & 0 & 0 \\ 0 & 0 & i\delta u_j & 1-2i\delta & i\delta v_j & 0 & 0 \\ 0 & 0 & 0 & \ddots & \ddots & \ddots & 0 \\ 0 & 0 & 0 & 0 & i\delta u_{N_\perp} & 1-2i\delta & i\delta v_{N_\perp} \\ 0 & 0 & 0 & 0 & 0 & 0 & 0 \end{pmatrix} \begin{pmatrix} E_0^n \\ E_1^n \\ \vdots \\ E_j^n \\ \vdots \\ E_{N_\perp}^n \\ E_{N_\perp+1}^n \end{pmatrix} \quad (137)$$

$$L_- E_j^n = \begin{pmatrix} d_{0,-}^{(o)} & d_{1,-}^{(o)} & 0 & 0 & 0 & 0 & 0 \\ -i\delta u_1 & 1+2i\delta & -i\delta v_1 & 0 & 0 & 0 & 0 \\ 0 & \ddots & \ddots & \ddots & 0 & 0 & 0 \\ 0 & 0 & -i\delta u_j & 1+2i\delta & -i\delta v_j & 0 & 0 \\ 0 & 0 & 0 & \ddots & \ddots & \ddots & 0 \\ 0 & 0 & 0 & 0 & -i\delta u_{N_\perp} & 1+2i\delta & -i\delta v_{N_\perp} \\ 0 & 0 & 0 & 0 & 0 & 0 & 1 \end{pmatrix} \begin{pmatrix} E_0^n \\ E_1^n \\ \vdots \\ E_j^n \\ \vdots \\ E_{N_\perp}^n \\ E_{N_\perp+1}^n \end{pmatrix} \quad (138)$$

where first order accurate boundary conditions ($o = 1$) at the origin are enforced by:

$$d_{0,+}^{(1)} = 0, \quad d_{1,+}^{(1)} = 0, \quad (139)$$

$$d_{0,-}^{(1)} = 1, \quad d_{1,-}^{(1)} = -\nu, \quad (140)$$

and ν is unity for cylindrical geometry or zero for the planar case. For second order accurate boundary conditions ($o = 2$) at the origin:

$$d_{0,+}^{(2)} = 1 - 4i\delta, \quad d_{1,+}^{(2)} = 4i\delta, \quad (141)$$

$$d_{0,-}^{(2)} = 1 + 4i\delta, \quad d_{1,-}^{(2)} = -4i\delta. \quad (142)$$

Table 3. Crank-Nicolson Algorithm.

– 1. definition of useful data, e.g., beam width w_0 , focusing length f , laser wavelength λ_0 , index of refraction n_0 and central wave number $k_0 = n_0 2\pi/\lambda_0$.
– 2. definition of grids and z -invariant quantities for space marching the field over one step Eq. (135). <ul style="list-style-type: none"> – number of inner grid points N_\perp – r-grid: $r_j = r_{\min} + j\Delta r$, for $j = 0, \dots, N_\perp + 1$ – matrix L_+ and L_-: $L_\pm = 1 \pm i\delta\Delta_j$ – boundary conditions: replace first and last lines of L^\pm as indicated in Eqs. (137) and (138) – calculation of the inverse L_-^{-1} – calculation of the product $L = L_-^{-1}L_+$
– 3. definition of the initial field $E_j^0 = \mathcal{E}(r_j, z = 0)$, $j = 0 \dots N_\perp + 1$, e.g., as in Eq. (125) for a Gaussian beam
– 4. perform a loop for $N_z = M \times K_{max}$ propagation steps, with an outer loop including computationally expensive diagnostics each M steps and an inner loop including costless diagnostics performed each step:
outer loop: $k = 1, \dots, K_{max}$ inner loop: $m = 1, \dots, M$ $n = (k - 1)M + m$ $E_j^n = LE_j^{n-1}$ perform costless diagnostic n end inner loop perform expensive diagnostic k end outer loop

Different type of boundary conditions can be implemented in a similar way, and potentially involve more than a single line of the complex matrix L^+ and L^- for each boundary. For example, it may be needed to add boundary layers on one or several edges of the numerical box so as to avoid spurious reflection on the boundary in cases where free-space propagation is desired. The goal of the boundary layer is to mimic a physical process over a limited domain close to the boundary, that will prevent as much as possible incoming waves to be reflected. This can be achieved with absorption of the incoming waves, or diffusion. With a careful selection of the boundary layer features, the latter choice was shown to lead theoretically to no reflection and was called *perfectly matched layers* boundary conditions [43].

We can now detail in table 3 the different steps to build a simple propagation code for simulations of Eq. (124):

Steps 1 to 3 correspond to the initialization of the propagation. Step 4 constitutes the bulk of the scheme; it is centered around one propagation step following Eq. (135). By diagnostics, we mean the selection of a given set of computed data and their storage in external files for post-processing. In order to save computational time and memory, diagnostics can be separated into computationally expensive diagnostics and costless diagnostics. Costless diagnostics do not require long CPU time or large disk-memory and can thus be performed at each step without significant performance degradation. Typically, these concern sub-dimensional diagnostics such as, e.g., monitoring of the maximum intensity vs propagation distance. In contrast, expensive diagnostics require more computer resources, time or memory, such as monitoring the full spatial, temporal or spectral- beam or pulse dynamics and not only subdimensional slices. A proper balance between expensive and costless diagnostics must be ensured for a good efficiency of the whole simulation.

Spectral technique. We present in this section one of the most straightforward way to implement a numerical scheme for solving Eq. (124). It consists in a spectral method relying on a Fourier decomposition of the laser beam into its spectral components. We assume here a planar geometry and note that the method extends easily to the cylindrical geometry by replacing Fourier by Hankel transforms:

$$\tilde{\mathcal{E}}(k_x, z) = \int_{-\infty}^{+\infty} \mathcal{E}(x, z) \exp(-ik_x x) dx. \quad (143)$$

Applying this transformation to Eq. (124) leads to a simple set of ordinary differential equations for the spectral components of the beam envelope $\tilde{\mathcal{E}}(k_x, z)$:

$$\frac{\partial \tilde{\mathcal{E}}(k_x, z)}{\partial z} = -i \frac{k_x^2}{2k_0} \tilde{\mathcal{E}}(k_x, z) \quad (144)$$

which has a formal solution:

$$\tilde{\mathcal{E}}(k_x, z) = \tilde{\mathcal{E}}(k_x, z = 0) \times \exp\left(-i \frac{k_x^2}{2k_0} z\right). \quad (145)$$

From Eq. (145), the solution obtained by back transforming the spectral components into the spatial domain reads

$$\mathcal{E}(x, z) = \frac{1}{2\pi} \int_{-\infty}^{\infty} \tilde{\mathcal{E}}(k_x, z = 0) \times \exp\left(-i \frac{k_x^2}{2k_0} z + ik_x x\right) dk_x. \quad (146)$$

The numerical implementation of this is made straightforward by the availability of libraries including fast Fourier transform modules. We can now detail in Table 4 the different steps to simulate propagation governed by Eq. (124) with a Spectral Decomposition Algorithm: Boundary conditions are assumed to be periodic and automatically enforced by the Fourier decomposition, i.e., by the Fast Fourier Transforms performed at each step. In practice, this means that a sufficiently large spatial box must be chosen if this method is used to simulate free space propagation with fields exponentially decaying far from the peak. In a too small box, a beam would sooner or later hit a boundary and be artificially reintroduced at the opposite boundary.

Naturally Eq. (146) shows that the solution at an arbitrarily large propagation distance can be obtained in a single step from the input spectral components $\tilde{\mathcal{E}}(k_x, z = 0)$ to the final far-field $\tilde{\mathcal{E}}(k_x, z)$, without iteratively space marching the solution over N_z propagation steps of size z/N_z . This option is however restricted to linear propagation equations. Multiple steps as indicated in table 4 become necessary when nonlinear terms are added on the right hand side of Eq. (124), which is the reason for having specified them in the scheme. Due to the availability of Fast Fourier Transform routines in computational libraries and in spite of the imposed periodic boundary conditions, this scheme is fully explicit and might thus appear as more efficient than the Crank-Nicolson scheme. This advantage is lost when the scheme is extended to cylindrical geometries. In this case, FFT must be replaced by Hankel transforms. Although Fast Hankel Transform algorithms have been developed, these are not so fast as FFTs and usually require a specific grid point distribution. These constraints must be kept in mind in the design of efficient extensions of the above schemes.

The reader is referred to section 4.1.1 for a practical example of implementation of a scheme similar to that of table 4 but applied to pulse dispersion instead of diffraction, and to the next section for an extension of this scheme in the presence of nonlinearity.

Test of Diffraction. Any practical implementation of Eq. (124) must properly reproduce existing analytical solutions. Equation (124) allows for simulations of the

Table 4. Spectral Decomposition Algorithm.

– 1. definition of useful data, e.g., beam width w_0 , focusing length f , laser wavelength λ_0 , index of refraction n_0 and central wave number $k_0 = n_0 2\pi/\lambda_0$.
– 2. definition of grids and z -invariant quantities for space marching the field over one step Eq. (145). <ul style="list-style-type: none"> – number of grid points N_x – x-grid: $x_j = x_{min} + j\Delta x$, for $j = 0, \dots, N_x - 1$ – k_x-grid: $k_{xj} = j\Delta k_x$, for $j = 0, \dots, N_x/2 - 1$; $k_{xj} = -\pi/\Delta x + (j - N_x/2)\Delta k_x$, for $j = N_x/2 \dots N_x - 1$ with $\Delta k_x = 2\pi/(N_x\Delta x)$. – precalculation of the vector $A_j \equiv \exp[-2i\delta(k_{xj}\Delta x)^2]$ for $j = 0, \dots, N_x - 1$, with $\delta \equiv \Delta z/4k_0(\Delta x)^2$ and $k_{xj}\Delta x = 2\pi j/N_x$ for $j = 0, \dots, N_x/2 - 1$, $k_{xj}\Delta x = 2\pi(-1 + j/N_x)$ for $j = N_x/2 \dots N_x - 1$.
– 3. definition of the initial field $E_j^0 = \mathcal{E}(x_j, z = 0)$, $j = 0 \dots N_\perp + 1$, and its spectrum $\tilde{E}_j^0 = \tilde{\mathcal{E}}(k_{xj}, z = 0) = FFT(E_j^0)$, $j = 0 \dots N_\perp + 1$.
– 4. space march the solution by performing a double-loop for $N_z = M \times K_{max}$ propagation steps, with expensive and costless diagnostics: <div style="text-align: center; margin: 10px 0;"> outer loop: $k = 1, \dots, K_{max}$ inner loop: $m = 1, \dots, M$ $n = (k - 1)M + m$ $\tilde{E}_j^{n-1} = FFT(E_j^{n-1})$ $\tilde{E}_j^n = \tilde{E}_j^{n-1} \times A_j$ for all j $E_j^n = FFT(\tilde{E}_j^n)$ perform costless diagnostic n end inner loop perform expensive diagnostic k end outer loop </div>

propagation of Gaussian beams. The laws of Gaussian optics must therefore be reproduced by a numerical simulation of Eq. (124). Using the input Gaussian beam defined by Eq. (125), analytical formulas for Gaussian beam propagation read as:

$$\mathcal{E}(r, z) = \mathcal{E}_0 \frac{w_0}{w(z)} \exp\left(-\frac{r^2}{w^2(z)} + i\frac{k_0 r^2}{2R(z)} - i\Psi(z)\right), \quad (147)$$

where the beam parameters evolution is defined as:

$$\begin{bmatrix} w(z) \\ R(z) \\ \Psi(z) \end{bmatrix} = \begin{bmatrix} w_0 \left[\left(1 - \frac{z}{f}\right)^2 + \frac{z^2}{z_R^2} \right]^{1/2} \\ z - d_f + \frac{d_f(f - d_f)}{z - d_f} \\ \arctan\left(\frac{z - d_f}{(fd_f - d_f^2)^{1/2}}\right) \end{bmatrix} \quad \text{or} \quad \begin{bmatrix} w(z) \\ R(z) \\ \Psi(z) \end{bmatrix} = \begin{bmatrix} w_f \left[1 + \frac{(z - d_f)^2}{z_f^2} \right]^{1/2} \\ z - d_f + \frac{z_f^2}{z - d_f} \\ \arctan\left(\frac{z - d_f}{z_f}\right) \end{bmatrix} \quad (148)$$

where the first set in Eq. (148) involves only the input beam parameters and the focal distance $d_f = f/(1 + f^2/z_R^2)$, where $z_R = k_0 w_0^2/2$ denotes the Rayleigh length associated with the input beam width. The second set in Eq. (148) refers to the standard laws for which the origin of coordinate along the propagation axis is the waist position $z = d_f$. Other quantities are the beam waist $w_f = w_0 f/\sqrt{f^2 + z_R^2}$ and the Rayleigh length relative to the beam waist $z_f \equiv k_0 w_f^2/2$. Both sets of equations are identical as consistency is ensured by the relation $d_f(f - d_f) = z_f^2$.

3.1.2 Diffraction and nonlinear effects

Extended Crank-Nicolson scheme. The Crank-Nicolson scheme extends to propagation equations of the NLS type such as Eq. (102) or Eq. (110). In this aim, we will treat nonlinearity by the second order Adams-Bashforth scheme which is an explicit scheme working in general for all type of nonlinear terms. Thus, we define a prototypical equation

$$\frac{\partial \mathcal{E}}{\partial z} = \frac{i}{2k_0} \Delta_{\perp} \mathcal{E} + \mathcal{N}(\mathcal{E}), \quad (149)$$

where $\mathcal{N}(\mathcal{E})$ models the nonlinearity under investigation, e.g. $\mathcal{N}(\mathcal{E}) \equiv i \frac{\omega_0}{c} n_2 \mathcal{I} \mathcal{E}$ for the optical Kerr effect as in Eq. (102) or $\mathcal{N}(\mathcal{E}) \equiv i \frac{\omega_0}{c} n_2 \mathcal{I} \mathcal{E} - \frac{\beta_K}{2} \mathcal{I}^{K-1} \mathcal{E}$ for multiphoton absorption and Kerr effect as in Eq. (110). The advantage of the Adams-Bashforth scheme with respect to a completely implicit scheme lies in the fact that it preserves the second-order accuracy of the Crank-Nicolson scheme and allows fast calculations of the right hand side in Eq. (149). The implementation of a fully implicit scheme with nonlinear terms would indeed require the resolution of nonlinear implicit equations, which cannot be done as easily as solving linear implicit equations. It usually requires predictor-corrector routines and a large number of matrix inversions, thereby increasing the computational cost.

The proposed alternative can be viewed as applying a second order Adams-Bashforth time integrator to nonlinear term in the Crank-Nicolson scheme which reads:

$$E_j^{n+1} - E_j^n = i\delta(\Delta_j E_j^{n+1} + \Delta_j E_j^n) + \left\{ \frac{3}{2} N_j^n - \frac{1}{2} N_j^{n-1} \right\}, \quad (150)$$

where

$$N_j^n \equiv \Delta z \mathcal{N}(E_j^n) = \Delta z \left\{ i \frac{\omega_0}{c} n_2 |E_j^n|^2 E_j^n - \frac{\beta_K}{2} |E_j^n|^{2K-2} E_j^n \right\}. \quad (151)$$

Note that the nonlinear terms on the rhs of Eq. (150) only involve previously obtained fields E_j^n and E_j^{n-1} . The coefficients 3/2 and -1/2 ensure the second order accuracy. A scheme where the nonlinear terms are simply written as N_j^n on the rhs of Eq. (150) would work as well, however, the second order accuracy of the Crank-Nicolson scheme would be lost. Equation (150) is still an implicit equation but it allows us to express the vector E_j^{n+1} without more effort than in the absence of nonlinearities:

$$E_j^{n+1} = (L_-)^{-1} \left[L_+ E_j^n + \frac{3}{2} N_j^n - \frac{1}{2} N_j^{n-1} \right]. \quad (152)$$

Equation (152) extends Eq. (136) to the case of nonlinear propagation over a single step and constitutes the core of the scheme, which must be repeated to cover the entire propagation domain. The numerical scheme will therefore be similar to the Crank-Nicolson scheme in table 3, with the following differences: It is no longer necessary to compute and store the product $L_-^{-1} L_+$ in the initialization step 2 since each propagation step use independently L_+ and L_-^{-1} , which should thus be stored in different tables. Only the 4th step in the numerical scheme of table 3 must be modified as indicated in table 5.

The overall stability of the scheme depends on the nonlinear terms, so that a control of the step size Δz may be necessary in contrast to the unconditionally stable Crank-Nicolson scheme of table 3; however, the stability constraint is often found to be not so drastic as that for the description of diffraction with an explicit scheme ($\Delta z \leq k_0 (\Delta r)^2$) [41], which justifies the explicit treatment of nonlinearities.

Split-step technique. Propagation equations and more generally PDEs including several source terms as in Eq. (149) can be solved by an alternative scheme, the

Table 5. Crank-Nicolson Algorithm with explicit nonlinearity treated by the second order Adams-Bashforth scheme.

- 1. same as in table 3 and definition of data for nonlinearity, e.g., n_2, β_K .
- 2. definition of grids and matrix storage of L_+ and L_-^{-1} : $L_{\pm} = 1 \pm i\delta\Delta_j$ as in table 3. Introduction of boundary conditions in L_+ and L_- .
- 3. definition of the initial field $E_j^0 = \mathcal{E}(r_j, z = 0)$, $j = 0 \dots N_{\perp} + 1$.
- 4. double-loop for $N_z = M \times K_{max}$ propagation steps with two types of diagnostics at each step and each M steps:

```

outer loop:  $k = 1, \dots, K_{max}$ 
  inner loop:  $m = 1, \dots, M$ 
     $n = (k - 1)M + m$ 
    calculate and store vector  $N_j^{n-1}$  (loop  $j, \dots, N_{\perp}$ )
    calculate  $V_j^{n-1} = L_+ E_j^{n-1}$  (product matrix-vector)
    add  $S_j^{n-1} = V_j^{n-1} + (3N_j^{n-1} - N_j^{n-2})/2$  (sum of vectors)
     $E_j^n = L_-^{-1} S_j^{n-1}$  (product matrix-vector)
    perform costless diagnostic  $n$ 
  end inner loop
  perform expensive diagnostic  $k$ 
end outer loop

```

split-step method, that we introduce in the following. The idea of the split-step technique is to perform a fractional step for each source term by means of a suitable scheme that applies to each part. For example the propagation equation (149) takes the form $\partial_z \mathcal{E} = \mathcal{L}\mathcal{E} + \mathcal{N}(\mathcal{E})$, where $\mathcal{L} \equiv (i/2k_0)\Delta_{\perp}$. Previously presented algorithms allow us to treat each source term as in the set of equations:

$$\partial_z \mathcal{E} = \mathcal{L}\mathcal{E}, \quad (153)$$

$$\partial_z \mathcal{E} = \mathcal{N}(\mathcal{E}). \quad (154)$$

Equation (153) representing the linear part of Eq. (149) can be solved by e.g. the Crank-Nicolson algorithm (Eq. (135) and table 3) or by means of the spectral decomposition algorithm (Eq. (145) and table 4). Equation (154) representing the nonlinear part of Eq. (149) can be solved by e.g. the second order Adams-Bashforth method presented in previous section which reads:

$$E_j^{n+1} = E_j^n + \frac{3}{2}N_j^n - \frac{1}{2}N_j^{n-1}. \quad (155)$$

A split step scheme consists in sequentially propagating the envelope over a *fractional-step* of size Δz by each of the algorithms used for Eqs. (153) and (154). Here, *fractional-step* is not related to the step size but means that only part of source terms are considered. By denoting $E_j^{n+1/2}$ the discretized envelope after the first split-step, we obtain the scheme

$$E_j^{n+1/2} = E_j^n + \frac{3}{2}N_j^n - \frac{1}{2}N_j^{n-1}, \quad (156)$$

$$E_j^{n+1} = (1 - i\delta\Delta_j)^{-1}(1 + i\delta\Delta_j)E_j^{n+1/2}. \quad (157)$$

Hence, for the split-step scheme applied to Eq. (149), stages 1 to 3 of table 5 are identical with additional storage of matrix $L = L_-^{-1}L_+$ as in table 3, whereas stage

Table 6. Split-step algorithm with nonlinearity treated by the explicit second order Adams-Bashforth scheme and linear term treated by the Crank-Nicolson scheme.

<p>– 4- double-loop for $N_z = M \times K_{max}$ propagation steps with two types of diagnostics at each step and each M steps:</p> <p>outer loop: $k = 1, \dots, K_{max}$ inner loop: $m = 1, \dots, M$ $n = (k - 1)M + m$ calculate and store vector $N_j^{n-1} = \Delta z \mathcal{N}(E_j^{n-1})$ (loop j, \dots, N_\perp) first <i>half-step</i>: $E_j^{n-1/2} = E_j^{n-1} + (3N_j^{n-1} - N_j^{n-2})/2$ second <i>half-step</i>: $E_j^n = L E_j^{n-1/2}$ (product matrix-vector) perform costless diagnostic n end inner loop perform expensive diagnostic k end outer loop</p>
--

4 is modified as indicated in table 6. Note that the split-step scheme can be generalized to more than two *half-steps* when there are more than two source terms. The separation between linear and nonlinear effects is also convenient but not mandatory to implement a split-step scheme.

3.1.3 Diffraction and Dispersion

In Sections 3.1.1 and 3.1.2, we have considered beam propagation with $\mathcal{E} = \mathcal{E}(r, z)$ depending on the transverse r and evolution z variables only. The methods we have presented also apply to pulses with one or more additional dimensions. For example with a temporal dimension $\mathcal{E} = \mathcal{E}(r, t, z)$, the new coordinate is discretized as $t_l = t_{min} + l\Delta t$ and pulse propagation is described by applying one of the presented schemes to each time t_l . This is achieved by including each propagation step of previous schemes in a loop on the time index l . The discretized pulse envelope at a given propagation distance z_n must be defined over a two dimensional grid as $E_{j,l}^n = \mathcal{E}(r = r_j, t = t_l, z = z_n)$ for $j = 0, \dots, N_\perp$ and $l = 0, \dots, N_t$. The input pulse, e.g., a Gaussian pulse with spatial and temporal quadratic phases modeling lens-focusing (focal length f) and chirp C can be defined as:

$$\mathcal{E}(r, t, z = 0) = \mathcal{E}_0 \exp \left(-\frac{r^2}{w_0^2} - i \frac{k_0 r^2}{2f} - (1 + iC) \frac{t^2}{t_p^2} \right), \quad (158)$$

and its discretized counterpart as $E_{j,l}^0 = \mathcal{E}(r = r_j, t = t_l, z = z_0)$. As long as the propagation equation does not involve differential operators with time derivatives, these are the only additional features extending previous schemes from (1+1) to (2+1) dimensions. However, higher dimensionality is usually associated with couplings between the different slices in the additional dimension. In the time direction, dispersive effects plays this role. We will consider the lowest dispersive order, namely second order dispersion to present a standard way to extend the Crank-Nicolson scheme to (2+1)D simulations. We thus start from the diffraction-dispersion equation:

$$\frac{\partial \mathcal{E}}{\partial z} = \frac{i}{2k_0} \Delta_\perp \mathcal{E} - i \frac{k_0^{(2)}}{2} \frac{\partial^2 \mathcal{E}}{\partial t^2} \quad (159)$$

The split-step technique naturally applies to design an algorithm for Eq. (159) with each fractional step relying on either a Crank-Nicolson algorithm, a Fourier decomposition, or a combination of both. The efficient way to implement the first option leads to the Alternate Direction Implicit scheme. The second option is straightforward and the third will be presented in Sec. 3.1.4.

Gaussian optics for dispersion. Starting from a numerical code where diffraction described by Eq. (124) was successfully implemented and checked with respect to the laws of Gaussian optics, any implementation of dispersive terms as in Eq. (159) requires new tests ensuring that (i) diffraction still works properly, (ii) dispersion is correctly implemented and (iii) the combination of both effects is correct.

Test (i) can be easily performed by setting $k_0^{(2)} = 0$ as an additional input condition and checking again the laws for Gaussian optics. Similarly, test (ii) can be performed by setting the diffraction coefficient to zero (parameter δ in the schemes) and by comparing the results to the laws for Gaussian pulse optics. Using Eq. (158) as an input condition, the law for Gaussian pulse propagation reads:

$$\mathcal{E}(t, z) = \mathcal{E}_0 \frac{t_p}{T(z)} \exp \left(-\frac{t^2}{T^2(z)} \left\{ 1 + i \left[C + (1 + C^2) \frac{z}{z_{\text{ds}}} \right] \right\} - i\Phi(z) \right), \quad (160)$$

where the beam parameters evolution is defined as:

$$\begin{bmatrix} T(z) \\ \Phi(z) \end{bmatrix} = \begin{bmatrix} t_p \left[\left(1 + C \frac{z}{z_{\text{ds}}} \right)^2 + \frac{z^2}{z_{\text{ds}}^2} \right]^{1/2} \\ \arctan \left(\frac{(1+C^2)z+C}{z_{\text{ds}}} \right) \end{bmatrix} \quad (161)$$

where $z_{\text{ds}} = t_p^2 / 2k_0^{(2)}$ denotes the dispersion length. For normal dispersion ($k_0^{(2)} > 0$) and a positive chirp coefficient, the pulse duration increases with distance whereas for a negative chirp coefficient, the pulse duration first decreases until it reaches $T_m = t_p / (1 + C^2)$ at distance $z_m = -Cz_{\text{ds}} / (1 + C^2)$, and then increases while the Gaussian pulse shape is preserved. All these properties must be reproduced in a correct implementation of dispersion.

Since the linear propagation of the pulse preserves the separation of time and space variables, test (iii) consists again in comparing numerical results with the laws for Gaussian optics for the beam and the pulse when both diffraction and dispersion have non-zero coefficients.

Alternate direction implicit (ADI) scheme. The Alternate Direction Implicit scheme is a split-step scheme comprising two half-steps of size $\Delta z/2$, each of which treating both the transverse and the temporal dimensions but only one dimension is treated implicitly during within the first half-step while the other is treated explicitly. Within the second half-step, dimensions are alternated with respect to their implicit/explicit treatment [44]. Applying this technique to Eq. (159) leads to the discretized equations:

$$E_{j,l}^{n+1/2} = E_{j,l}^n + i\delta\Delta_{\perp}E_{j,l}^{n+1/2} + id\Delta_tE_{j,l}^n \quad (162)$$

$$E_{j,l}^{n+1} = E_{j,l}^{n+1/2} + i\delta\Delta_{\perp}E_{j,l}^{n+1/2} + id\Delta_tE_{j,l}^{n+1} \quad (163)$$

where

$$\Delta_tE_{j,l}^n \equiv E_{j,l+1}^n - 2E_{j,l}^n + E_{j,l-1}^n \quad (164)$$

and

$$\delta \equiv \frac{\Delta z}{4k_0(\Delta r)^2}, \quad d = -\frac{\Delta zk_0^{(2)}}{4(\Delta t)^2}. \quad (165)$$

The scheme described by Eqs. (162,163) is rewritten compactly using the tridiagonal complex matrix

$$L_{\pm}(\delta) \equiv 1 \pm i\delta\Delta_{\perp}, \quad (166)$$

$$L_{\pm}(d) \equiv 1 \pm i\delta\Delta_t, \quad (167)$$

in the form

$$L_{-}(\delta)E_{j,l}^{n+1/2} = L_{+}(d)E_{j,l}^n \quad (168)$$

$$L_{-}(d)E_{j,l}^{n+1} = L_{+}(\delta)E_{j,l}^{n+1/2} \quad (169)$$

or in a single step:

$$E_{j,l}^{n+1} = L_{-}(d)^{-1}[L_{+}(\delta)(L_{-}(\delta)^{-1}\{L_{+}(d)E_{j,l}^n\}^T)]^T, \quad (170)$$

where superscript T denotes transposition and reflects the fact that $L_{\pm}(\delta)$ and $L_{\pm}(d)$ act on different dimensions of the envelope, i.e., $L_{\pm}(d)$ act on the temporal dimension (columns of $E_{j,l}^n$) whereas $L_{\pm}(\delta)$ act on the transverse dimension (rows of $E_{j,l}^n$). On physical grounds in our case, it is equivalent to reverse the order in which different dimensions are treated implicitly, hence a single step can also be written as:

$$E_{l,j}^{n+1} = L_{-}(\delta)^{-1}[L_{+}(d)(L_{-}(d)^{-1}\{L_{+}(\delta)E_{l,j}^n\}^T)]^T, \quad (171)$$

where $E_{j,l}^n = \{E_{l,j}^n\}^T$. Mathematically, the interchange is equivalent only if the matrices commute.

3.1.4 Diffraction, dispersion and nonlinear effect – spectral extended Crank-Nicolson scheme

This section presents an extension of the Crank-Nicolson scheme for (2+1)D simulations of paraxial propagation equations presented in the theory section, namely those which in the canonical form read as:

$$\frac{\partial \hat{\mathcal{E}}}{\partial z} = \frac{i}{2\mathcal{K}_0(\Omega)}\Delta_{\perp}\hat{\mathcal{E}} + i\mathcal{D}(\Omega)\hat{\mathcal{E}} + \frac{i}{2\mathcal{K}_0(\Omega)}\frac{\omega^2}{c^2}\frac{\hat{\mathcal{P}}}{\epsilon_0}, \quad (172)$$

where $\hat{\mathcal{E}} = \hat{\mathcal{E}}(r, \Omega, z)$, $\Omega = \omega - \omega_0$, $\mathcal{K}_0(\Omega) \equiv \mathcal{K}(\Omega, \mathbf{k}_{\perp} = 0)$ denotes any of the \mathcal{K} functions listed in the Table 2, and the subscript zero in \mathcal{K}_0 will be omitted for simplicity. The proposed extended Crank-Nicolson scheme is simply applied frequency component by frequency component and therefore includes all effects that are naturally included in frequency dependent terms of Eq. (172), namely dispersion, space-time focusing and self-steepening.

The temporal coordinate is discretized with N_t equally spaced steps of size Δt : $t_l = t_0 + l\Delta t$ for $l = 0 \cdots N_t - 1$, we have a corresponding discretization of the spectral domain $\omega_l = \omega_0 + l\Delta\omega$ for $l = 0 \cdots N_t/2 - 1$, $\omega_l = \omega_0 - \pi/\Delta t + l\Delta\omega$ for $l = N_t/2 \cdots N_t - 1$, with $\Delta\omega = 2\pi/[N_t\Delta t]$. The natural variable for the envelope spectra is $\Omega_l = \omega_l - \omega_0$. Note that in this section, the index l will refer to either discrete times or discrete frequencies, depending on whether the quantity we consider belongs to the temporal or the spectral domain. For completeness, we reintroduce a current in the nonlinear terms of Equation (172):

$$\frac{\partial \hat{\mathcal{E}}}{\partial z} = \frac{i}{2\mathcal{K}(\Omega)}\Delta_{\perp}\hat{\mathcal{E}} + i\mathcal{D}\hat{\mathcal{E}} + \frac{i}{2\mathcal{K}(\Omega)}\frac{\omega^2}{c^2}\frac{\hat{\mathcal{P}}}{\epsilon_0} - \frac{1}{2\mathcal{K}(\Omega)}\frac{\omega}{c}\frac{\hat{\mathcal{J}}}{\epsilon_0 c}. \quad (173)$$

Let \mathcal{K}_l and \mathcal{D}_l denote $\mathcal{K}(\Omega_l)$ and $\mathcal{D}(\Omega_l)$, respectively. The numerical scheme extending Eq. (150) and corresponding to Eq. (173) reads:

$$\hat{E}_{j,l}^{n+1} - \hat{E}_{j,l}^n = i\delta_l(\Delta_j \hat{E}_{j,l}^{n+1} + \Delta_j \hat{E}_{j,l}^n) + id_l(\hat{E}_{j,l}^{n+1} + \hat{E}_{j,l}^n) + \frac{3}{2}\hat{N}_{j,l}^n - \frac{1}{2}\hat{N}_{j,l}^{n-1} \quad (174)$$

where

$$\delta_l = \delta \frac{k_0}{\mathcal{K}_l} = \frac{\Delta z}{4(\Delta r)^2 \mathcal{K}_l} \quad (175)$$

$$d_l = \frac{\Delta z \mathcal{D}_l}{2} \quad (176)$$

$$\hat{N}_{j,l}^n \equiv \frac{i\Delta z}{2\mathcal{K}_l} \frac{\omega_l^2}{c^2} \frac{\hat{P}_{j,l}^n}{\epsilon_0} - \frac{\Delta z}{2\mathcal{K}_l} \frac{\omega_l}{c} \frac{\hat{J}_{j,l}^n}{\epsilon_0 c}. \quad (177)$$

The solution to equation (174) represents one step along the propagation direction:

$$\hat{E}_{j,l}^{n+1} = (L_{-,l})^{-1} [L_{+,l} \hat{E}_{j,l}^n + \frac{3}{2}\hat{N}_{j,l}^n - \frac{1}{2}\hat{N}_{j,l}^{n-1}] \quad (178)$$

where $L_{-,l} \equiv 1 - id_l - i\delta_l \Delta_j$, $L_{+,l} \equiv 1 + id_l + i\delta_l \Delta_j$. With respect to previous expressions of L_- and L_+ , the matrices $L_{-,l}$ and $L_{+,l}$ are different only by an additional frequency dependent term, i.e., l -dependent, on the diagonal. As for L_- and L_+ , the matrices $L_{-,l}$ and $L_{+,l}$ operate on vectors representing transverse profiles (described by index j) of the Fourier components $\hat{E}_{j,l}$ for the envelope, corresponding to the fixed frequency Ω_l ; in other words, Eq. (178) allows us to apply the standard Crank-Nicolson scheme to each frequency component l of the envelope spectrum, thus performing one step from $E_{j,l}^n$ at distance n to $E_{j,l}^{n+1}$ at distance $n+1$. This step must be inserted within a loop on frequencies (l).

Depending on the need to save either memory or simulation time, matrices $L_{-,l}$ and $L_{+,l}$ may be either precomputed (to minimize simulation time, in which case the additional amount of memory used corresponds to the size of a $14 \times N_\perp \times N_\omega$ table of real numbers, seven diagonals of complex numbers being needed to describe $L_{-,l}$ and $L_{+,l}$) or recomputed at each step (to minimize memory usage). In the second option, step 2 of the scheme is simplified since only a few frequency dependent tables must be precomputed in order to reconstruct $L_{-,l}$ and $L_{+,l}$ in step 4 with a minimum number of operations. The changes in steps 1 to 4 of the Crank-Nicolson scheme are indicated in table 7.

Step 4 still constitutes the bulk of the scheme. It is evident that efficiency of the code is enhanced if all unnecessarily repetitive calculations are avoided. These concern loops including multiplications by factors which do not vary with the loop index. For example it is clear that the quantities p_l and u_l in front of the nonlinear polarization and current must be precalculated and stored in step 2 so that the calculation of $N_{j,l}^{n-1}$ needs only two multiplications and an addition per element (j, l). Constant factors can also usually be removed via renormalization of the discretized equations. As a general rule, the efficiency of a code must be optimized by a careful count of all operations appearing in nested loops and an attempt to minimize them. For example, all matrix-vector operations performed on with tridiagonal matrices must be implemented so as to avoid unnecessary multiplication and sum of zeros. This can be achieved by using compact matrix storage for the non-zero diagonals only, as discussed in [41].

Table 7. Spectrally extended Crank-Nicolson algorithm.

<ul style="list-style-type: none"> – 1. definition of useful data: laser and medium parameter; in particular everything needed to properly define the dispersion relation in the medium and nonlinearity, e.g., Kerr parameters, ionization rates, etc. – 2. definition of grids and z invariant quantities: <ul style="list-style-type: none"> – r-grid: $r_j = j\Delta r$, for $j = 0, \dots, N_\perp + 1$ – t-grid: $t_l = t_{min} + l\Delta t$, for $l = 0, \dots, N_t - 1$ – ω-grid: $\omega_l = \omega_0 + l\Delta\omega$ for $l = 0, \dots, N_\omega/2 - 1$ $\omega_l = \omega_0 - \pi/\Delta t + l\Delta\omega$ for $l = N_\omega/2, \dots, N_\omega - 1$, with $\Delta\omega = 2\pi/[N_\omega\Delta t]$ and $N_\omega = N_t$ – calculation and storage of the one dimensional tables: $\mathcal{K}_l, \mathcal{D}_l, d_l, \delta_l, p_l \equiv \frac{i\Delta z}{2\mathcal{K}_l} \frac{\omega_l^2}{\epsilon_0 c^2}$, $u_l \equiv -\frac{\Delta z}{2\mathcal{K}_l} \frac{\omega_l}{\epsilon_0 c^2}$ – 3. definition of the initial field, $E_{j,l}^0 = \mathcal{E}(r_j, t_l, z = 0)$ by e.g., Eq. (158) for Gaussian profiles of the beam and pulse. Input spectral components by FFT: $\hat{E}_{j,l}^0 = FFT(E_{j,l}^0)$ – 4. double-loop on propagation steps with diagnostics each step and each M steps: 	
outer loop: $k = 1, \dots, K_{max}$ inner loop: $m = 1, \dots, M$ $n = (k - 1)M + m$ calculate quantities for nonlinearity, e.g.: electron density $\rho_{j,l}^{n-1} = \rho(r_j, t_l, z_{n-1})$ (solve ODE (118) for $j = 1, \dots, N_\perp$) Raman-Kerr term $Q_{j,l}^{n-1} = Q_i$ (r_j, t_l, z_{n-1}) (solve ODE (120) for $j = 1, \dots, N_\perp$) calculate and store $P_{j,l}^{n-1}, J_{j,l}^{n-1}$ ($j = 1, \dots, N_\perp; l = 0, \dots, N_\omega - 1$) $\{\hat{P}_{j,l}^{n-1}, \hat{J}_{j,l}^{n-1}\} = FFT(\{P_{j,l}^{n-1}, J_{j,l}^{n-1}\})$ (FFT) $j = 1, \dots, N_\perp$ $\hat{E}_{j,l}^{n-1} = FFT(E_{j,l}^{n-1})$ (FFT) $j = 1, \dots, N_\perp$ calculate and store $N_{j,l}^{n-1}$ from Eq. (177) (multiply $p_l \hat{P}_{j,l}^{n-1}, u_l \hat{J}_{j,l}^{n-1}$ and sum) loop on frequencies $l = 0, \dots, N_\omega - 1$ calculate $L_{+,l}, L_{-,l}$ (tridiagonal complex matrices) calculate $L_{-,l}^{-1}$ (matrix inversion) calculate $V_{j,l}^{n-1} = L_{+,l} \hat{E}_{j,l}^{n-1}$ (product matrix-vector) add $S_{j,l}^{n-1} = V_{j,l}^{n-1} + (3\hat{N}_{j,l}^{n-1} - \hat{N}_{j,l}^{n-2})/2$ (sum of vectors) $\hat{E}_{j,l}^n = L_{-,l}^{-1} S_{j,l}^{n-1}$ (product matrix-vector) end loop on frequencies (l) inverse Fourier transform $\hat{E}_{j,l}^n \rightarrow E_{j,l}^n$ (FFT $^{-1}$) $j = 1, \dots, N_\perp$ store $E_{j,l}^n$ perform costless diagnostic n end inner loop (m) perform expensive diagnostic k end outer loop (k)	

3.2 Numerical Methods for UPPE Solution

Having formulated our pulse propagation models in Sec. 2, we have seen a number of numerical simulation techniques valid for paraxial equations and we now address the question of how to solve non-paraxial equations numerically. To keep the notation simple, and equations readable, we will restrict ourselves to carrier-resolving equations

in the form of the simplest version of UPPE, namely a one-component propagation equation in a bulk medium. We also suppose that all nonlinear interactions are expressed in the nonlinear polarization P and for simplicity omit from our equations the current density term. Note that the numerical approach described next translates directly to a general vectorial case, and its practical implementation in software is essentially the same.

3.2.1 UPPE as a large system of ordinary differential equations

We have written the UPPE equation in a form which resembles the usual structure of pulse propagation equations and to which simulation practitioners in the field are most used to. The UPPE expresses evolution of the spectral (both temporal and spatial) transform of the electric field, and its right-hand-side contains linear and nonlinear terms:

$$\partial_z E_{k_x, k_y}(\omega, z) = ik_z E_{k_x, k_y}(\omega, z) + \frac{i\omega^2}{2\epsilon_0 c^2 k_z} P_{k_x, k_y}(\omega, z) \text{ where } k_z = \sqrt{k^2(\omega) - k_x^2 - k_y^2}. \quad (179)$$

Let us point out a few important points before going into details of a solver implementation. First, unlike many propagation models, this is in a spectral representation. It describes evolution of a Fourier spectrum, rather than that of a real physical field. One important consequence is that what we have is not a partial differential equation anymore. Rather, it is a system of ordinary differential equations for spectral amplitudes, albeit a very large system. Thus, there are no partial derivatives to approximate, which makes numerical solution conceptually very simple: One can utilize *any* available library for ODE systems, and the *only* remaining thing to do is to define a right-hand-side calculation subroutine which will be fed to the chosen ODE solver.

Second, the above representation, which is in terms of spectral amplitudes for electric field, is not exactly the one a numerical solver should work with. This is because the slowest-evolving variables in this problem only change in response to nonlinearity, and these are actually the *native variables* A_{k_x, k_y} which appeared in the course of UPPE derivation:

$$E_{k_x, k_y}(\omega, z) = A_{k_x, k_y}(\omega, z) \exp[ik_z z] \equiv A_{k_x, k_y}(\omega, z) \exp[i\sqrt{k^2(\omega) - k_x^2 - k_y^2} z]. \quad (180)$$

Their evolution equation (see Section 2.3) only contains nonlinear terms:

$$\partial_z A_{k_x, k_y}(\omega, z) = + \frac{i\omega^2}{2\epsilon_0 c^2 k_z} e^{-ik_z z} P_{k_x, k_y}(\omega, z) \text{ with } k_z = \sqrt{k^2(\omega) - k_x^2 - k_y^2}. \quad (181)$$

It is obvious that spectral amplitudes A are the slowest variable in the pulse evolution problem, because they do not change at all in a linear regime. This also means that UPPE equations exactly solve the linear part of a problem, which is an extremely desirable property (reader is encouraged to review various propagation equations specifically to recall how much *effort* often goes even into design of the linear part of all these equations). The most important advantage is the ability to model an arbitrary medium with frequency dependent index of refraction *and* frequency dependent losses.

Alternatively, one can view Eq. (181) as Eq. (179) to which integrating factor $\exp[ik_z z]$ has been applied. This cancels oscillations in the spectral amplitudes of the electric field which are due to linear propagation. Nonlinearity alone contributes to the evolution of the native UPPE variables A_{k_x, k_y} , and implementation based on them thus yields to faster numerical integration. This point of view makes it evident that there is a degree of freedom in the relation between E and A amplitudes. Namely, one

could also use an integrating factor $\exp[ik_z(z - z_0)]$, thus moving the point at which $A = E$ from $z = 0$ to z_0 . Lacking a better term, we say that E and A amplitudes are *aligned* at z_0 .

It is imperative that a simulator utilizes this degree of freedom. At $z = z_0$ spectral amplitudes of E and native variables A coincide, but as z increases, E and A diverge from each other. Although always connected by a simple complex phase change $\Delta\phi = k_z(\omega, k_x, k_y)(z - z_0)$, one must realize that the latter can attain very large values. To avoid numerical difficulties in handling the corresponding exponentials, the relation between E and A has to be re-aligned after every integration step by moving z_0 to the current propagation distance. After the new array of A is produced in the ODE solver taking a step Δz , re-alignment with E is achieved by

$$A_{k_x, k_y}^{\text{new}}(\omega, \Delta z) = \exp[ik_z(\omega, k_x, k_y)\Delta z]A_{k_x, k_y}^{\text{old}}(\omega, \Delta z). \quad (182)$$

After this operation, E and A amplitudes coincide once again when the next integration step is to be executed. Note that the above procedure corresponds to nothing but to the free, linear propagation of the field, and re-alignment therefore amounts to applying a linear propagator. In what follows it is assumed that amplitudes are aligned before each step, which means that $z = 0$ in Eq. (181) should be understood as a beginning of the current ODE solver step. It also means that all z values are small, restricted to $z < \Delta z$.

Equation (181) is not completely explicit, because it hides the fact that the non-linear polarization P must be calculated from the current value of the electric field. Indeed, polarization is a functional of $E(x, y, t, z)$ taken at a fixed z value. As a rule, medium models are formulated in real space. For example Raman-effect contribution to the change of refractive index can be expressed as convolution (in time) calculated at a given spatial point $(x, y, z) \equiv (\mathbf{r}, z)$. While the concrete relation between electric and polarization fields is unimportant for how the UPPE solver is designed, the fact that medium response is calculated in real space is crucial. We will therefore assume that a function implementation $P(x, y, t, z) = P_{\text{NL}}(\{E(x, y, t, z)\})$ is given, and that it calculates nonlinear polarization as a function of time from a history of the electric field at a fixed spatial point.

Let us incorporate this into our notation and write down an explicit definition of the UPPE ODE system. The unknown functions are $A_{k_x, k_y}(\omega, z)$ and they obey

$$\partial_z A_{k_x, k_y}(\omega, z) = + \frac{i\omega^2}{2\epsilon_0 c^2 k_z} e^{-ik_z z} P_{k_x, k_y}(\omega, z, \{E(x, y, z, t)\}), \quad k_z = \sqrt{k^2(\omega) - k_x^2 - k_y^2} \quad (183)$$

where

$$P_{k_x, k_y}(\omega, z, \{E(x, y, t)\}) = (2\pi)^{-3/2} \int e^{+i\omega t - ik_x x - ik_y y} P_{\text{NL}}(\{E(x, y, t, z)\}) dt dx dy \quad (184)$$

is a Fourier (or in general spectral) transform of $P_{\text{NL}}(\{E(x, y, t, z)\})$ which in turn encapsulates nonlinear medium properties. (Note that a solver implementation does not need to, and in fact should not know about its concrete functional form!) To evaluate the above, one first needs to calculate the real-space field from the native computational variables through another (inverse) Fourier transform

$$E(x, y, t, z) = (2\pi)^{-3/2} \int e^{-i\omega t + ik_x x + ik_y y} A_{k_x, k_y}(\omega, z) e^{ik_z z} d\omega dk_x dk_y. \quad (185)$$

Now it should be clear that when an ODE solver requests evaluation of its right-hand-side function for a given value of z , and for a given array $A_{k_x, k_y}(\omega, z)$, spectral

transforms will be invoked in both directions. One can view this as a price to pay for the elimination of partial derivatives from propagation equations, and for the ability to solve the linear problem exactly.

There is one more issue to clarify before transition to discretization, and that is that of a moving frame. It is of course advantageous, and in fact necessary, to follow pulse evolution in a frame of reference which moves with a velocity v_f (with respect to the laboratory frame) chosen such that at each location z in a lab, the pulse arrives at $t \approx 0$, and thus stays located around the center of the temporal computational domain. This is achieved by expressing time t through $t = \tau + z/v_f$ where τ is our new temporal variable. Inspection of Eqs. (183-185) reveals that this amounts to a simple modification of the linear propagator:

$$\exp [ik_z(\omega, k_x, k_y)\Delta z] \rightarrow \exp [ik_z(\omega, k_x, k_y)\Delta z - \Delta z\omega/v_f]. \quad (186)$$

We emphasize that v_f is an arbitrary parameter which does not reflect any physics of the model. It is merely an expression of what one deems to be the best reference frame. Quite often it is reasonable to choose

$$\frac{1}{v_f} = \frac{1}{v_g} = \frac{\partial k_z(\omega_{\text{pulse}}, k_x = 0, k_y = 0)}{\partial \omega} \quad (187)$$

which means that the computational frame of reference moves with the group velocity of the pulse. Readers familiar with Nonlinear Schrödinger Equation should realize that it is exactly the choice that makes a pulse described by NLS to stay localized in the vicinity of $\tau \approx 0$.

3.2.2 Discretization and spectral transforms

Because any UPPE solver is spectral in all dimensions, grid representation of both, real-space and spectral space fields is determined by properties of discrete spectral transforms. Depending on the symmetry of the problem, these are either variants of Fourier or discrete Hankel transforms.

Spatial (linear) axis

For a spatial dimension, say x , that spans one side of a computational domain box, the values of coordinates (in real space) and transverse wave numbers k_x (in spectral space) are those of ordinary Fourier transform sampling points. Both sets are equidistant and equal in size.

Temporal axis

A computational domain axis in time direction has its corresponding Fourier transform which is slightly modified due to the fact that physical fields are real-valued. It is sufficient to sample spectral amplitudes $A_{k_x, k_y}(\omega)$ only for positive angular frequencies ω . Moreover, one can restrict discrete sampling points to $\omega \in (\omega_{\min}, \omega_{\max})$ if one only knows the medium susceptibility $\chi^{(1)}(\omega)$ in this interval. Only these discrete frequencies become active in the simulations in the sense that they carry corresponding spectral amplitudes. When spectral-to-real transform is invoked, the active set of frequency-samples is padded by zeros before a standard Fourier transform is executed. This has the effect that the resulting real-space amplitude becomes the so-called analytic signal. While its real part corresponds to physical electric field, its modulus squared can be interpreted (in suitable units) as the time-averaged light intensity. Both quantities are often needed in the calculation of various nonlinear medium responses. Note that in this arrangement the total number of discrete samples in the time dimension is more than twice the number of active samples in the frequency

dimensions. However, the number of ODEs to solve is given by the active frequency samples.

Radial axis

For problems with axial symmetry, it is advantageous to utilize the radial discrete Hankel transform instead of a two-dimensional Fourier transform. Because the discrete Hankel transform is represented by a full matrix, it is not *fast* in the sense fast Fourier transforms are. Still, the main computational savings are related to the reduced dimensionality of variable-arrays representing physical fields. Sampling points in both real and spectral space are the same and namely given by scaled zeros of Bessel function J_0 . For example N samples in real space are $r_i = u_i/u_N R$ where $J_0(u_i) = 0$. Note that there is no radial sample located directly on the axis.

Readers concerned about the usage of *slow* spectral transform, should note that there are fast discrete Hankel transforms. However, UPPE solver requires a truly orthogonal transform implementation, because forward and inverse transformations are executed many times over the same array. Only the proper Hankel transform is orthogonal (and in addition equal to its own inverse) and should be preferred on grounds of numerical accuracy.

3.2.3 Integration of evolution equations for spectral amplitudes

The core of a UPPE solver can be based on essentially arbitrary ODE-solver library. A good library should have the capability to choose between different algorithms, and it will also take care of allocating auxiliary arrays based on the selected method. The advantage of using a canned library over hard-coding a concrete algorithm into the solver implementation is the flexibility in the choice of method, and also the fact that everything concerning auxiliary variables involved in ODE solution remains hidden. However, the UPPE system can contain several million variables, and that an ODE solver will, depending on the requested method, allocate several auxiliary arrays of the same size. As a consequence, the bulk of the memory allocated for the whole simulation will actually be requested by the solver. Not only the memory needs will be several times larger than those for one copy of all fields, but also that the method performance can be affected by the size of the system solved. In practice simpler methods tend to perform better than the more sophisticated ones. In particular, all methods that require calculation of a Jacobian are utterly unsuitable for UPPE solution. Fortunately, the standard ODE solver work-horses such as various Runge-Kutta methods work well.

Now, suppose we have calculated an array $A_{k_x, k_y}(\omega, z)$ representing the solution at propagation distance z . To keep the notation simple, discrete wave numbers k_x, k_y and active angular frequencies ω now represent array indices. To calculate $A_{k_x, k_y}(\omega, z + \Delta z)$, an ODE solver is invoked to produce it. Because we synchronize A and E representations after each step, we can understand $z = 0$ as if the currently executed step was the very first one. A pseudo-code for the integration loop reads:

Repeat for each step:

A) Invoke ODE Solver:

$$A_{k_x, k_y}(\omega, 0) \rightarrow A_{k_x, k_y}(\omega, \Delta z)$$

B) Re-align native and field variables:

$$A_{k_x, k_y}(\omega, \Delta z) = \exp[i(k_z(\omega, k_x, k_y) - \omega/v_f)\Delta z]A_{k_x, k_y}(\omega, \Delta z)$$

Readers may note that the above integration may seem like an operator splitting method. It does look as if nonlinear and linear *propagators* were applied in turns the same way as in the split-step approach. However, this is where the similarity ends. The second sub-step is nothing but a *shift* of our reference frame. If our numerics

did not suffer from rounding, and could evaluate exponentials with arbitrarily large arguments, this addition would not be necessary.

Behind the scenes, while executing A), ODE solver will invoke calculation of the right-hand-side of our ODE system, i.e. it asks to evaluate

$$\frac{i\omega^2}{2\epsilon_0 c^2 k_z} e^{-i(k_z - \omega/v_f)\Delta z} P_{k_x, k_y}(\omega, z, \{E(x, y, \Delta z, t)\})$$

for given spectral amplitudes $A_{k_x, k_y}(\omega)$. Depending on the ODE algorithm, call of this function occurs several times during a single integration step, each time with a different value of Δz . UPPE solver implements the function call in the following steps:

1. Apply linear propagator to shift from $z = 0$ to Δz :

$$A_{k_x, k_y}(\omega) \mapsto A_{k_x, k_y}(\omega) \exp [+i(k_z(\omega, k_x, k_y) - \omega/v_f)\Delta z]$$

2. Perform the spectral transform from spectral to real space:

$$E(x, y, t) = \text{FFT}\{A_{k_x, k_y}(\omega)\}$$

3. In real-space representation, calculate nonlinear medium response for a given field $E(x, y, t)$, using a user-supplied medium-response implementing algorithm P_{NL} :

$$P(x, y, t) = P_{\text{NL}}\{E(x, y, t)\}$$

4. Perform spectral transform from the real to spectral space:

$$P_{k_x, k_y}(\omega) = \text{FFT}^{-1}\{P(x, y, t)\}$$

5. Apply linear propagator to *undo* the previous shift in z :

$$P_{k_x, k_y}(\omega) \mapsto P_{k_x, k_y}(\omega) \exp [-i(k_z(\omega, k_x, k_y) - \omega/v_f)\Delta z]$$

6. Finally, multiply by the coupling factor and return result to the ODE solver:

$$P_{k_x, k_y}(\omega) \mapsto \frac{i\omega^2}{2\epsilon_0 c^2 k_z} P_{k_x, k_y}(\omega).$$

The above is the most computation-intensive part of UPPE solution and thus merits attention with respect to efficient parallel implementation.

3.2.4 Parallelization

Even if a problem has axial symmetry, a typical UPPE ODE system contains several million variables. It is therefore more or less necessary that computations are parallelized. Let us briefly point out facts that may influence our parallelization design decisions.

First, we have to take into account the fact that the UPPE framework is inherently spectral. This means that each processor or a thread of execution will, at some point, require access to *distant* locations in allocated arrays. The shared memory paradigm is therefore a natural way to go, and the current UPPEcore implementation uses Pthreads. OpenMP (i.e. pragma based loop parallelization) would probably work equally well for our purposes.

Second, one has to decide which parts of the code will actually execute in parallel. Of course, ideally all of them, but the question is if it is worth of the trouble. It turns out that most of the computational effort in UPPE is spent within the ODE system right-hand-side calculations and in performing spectral transforms. This invites a parallel work crew strategy: A master thread creates a family of workers or slaves and dispatches these to perform work as needed. The master thread executes all work outside of the ODE solver loop which includes all initialization, analysis or diagnostics of results, input, and output. Master also runs the main ODE loop without help from its slaves. (This is of course a compromise between the achievable parallelization efficiency and complexity of the solution!) This means that almost any serial ODE solver library can be used as a plug-in for the UPPE solver.

The parallel working crew enters a synchronization barrier immediately after their creation. Here, they wait for commands from their master who specifies which is the next function to execute in parallel. For example, this may be a spectral transform. Within the parallel section, each of the workers takes over a proportional part of the load. When the parallel section is done, workers meet again at the synchronization barrier, awaiting further commands from the master.

Obviously the biggest drawback of this design is that the ODE part of the code remains serial. Although it is relatively small, it would limit possible parallel speed up with a large number of threads. An alternative solution is akin to the domain decomposition strategy; the set of ODE equations is evenly distributed between multiple instances of ODE solvers, each executed by an independent thread. However, this solution requires a mild modification of the ODE routines that control adaptive integration step. Some earlier versions of the UPPEcore were based on this approach. Since the performance penalty with the working crew method is mostly negligible in practice, it is preferred because it does not require open access to the code of the ODE solver.

3.3 Numerical methods for nonlinear medium response models

This section is devoted to the numerical implementation of nonlinear response models by using a method similar to the so-called exponential time differencing method [45].

3.3.1 Numerical implementation of plasma related terms

A formal solution to Eq. (114) may be written as:

$$J(\mathbf{r}, t, z) = \frac{q_e^2}{m_e} \int_{-\infty}^t \exp\left(-\frac{t-t'}{\tau_c}\right) \rho(\mathbf{r}, t', z) E(\mathbf{r}, t', z) dt'. \quad (188)$$

From the knowledge of the field and electron density for all grid points, it is therefore possible to determine the current step by step by expressing for each fixed spatial position (\mathbf{r}, z) the current at time $t + \Delta t$ as a function of the current at previous time t :

$$J(\mathbf{r}, t + \Delta t, z) = \frac{q_e^2}{m_e} \int_{-\infty}^{t+\Delta t} e^{-(t+\Delta t-t')/\tau_c} \rho(\mathbf{r}, t', z) E(\mathbf{r}, t', z) dt'. \quad (189)$$

Omitting the (\mathbf{r}, z) dependence for simplicity, we obtain:

$$J(t + \Delta t) = \frac{q_e^2}{m_e} e^{-\Delta t/\tau_c} \left\{ \int_{-\infty}^t e^{-(t-t')/\tau_c} \rho' E' dt' + \int_t^{t+\Delta t} e^{-(t-t')/\tau_c} \rho' E' dt' \right\} \quad (190)$$

Table 8. Coefficients for modeling plasma current or electron density in Eq. (195).

$A(t)$	$Q(t)$	a	η
$J(t)$	$\rho(t)E(t)$	$e^{-\Delta t/\tau_c}$	$\frac{\Delta t}{2} \frac{q_e^2}{m_e}$
$\rho(t)$	$W_{\text{ofi}}[\mathcal{I}(t)]$	$e^{-\int_t^{t+\Delta t} [W'_{\text{ofi}} - W'_{\text{ava}}] dt'}$	$\frac{\Delta t}{2} \rho_{\text{nt}}$

where $\rho' E' \equiv \rho(\mathbf{r}, t', z)E(\mathbf{r}, t', z)$. This is rewritten by using a trapezoidal integration rule for the second term on the right hand side:

$$J(t + \Delta t) = e^{-\Delta t/\tau_c} \left\{ J(t) + \frac{\Delta t}{2} \frac{q_e^2}{m_e} \rho(t)E(t) \right\} + \frac{q_e^2 \Delta t}{2m_e} \rho(t + \Delta t)E(t + \Delta t). \quad (191)$$

Similarly, a formal solution to Eq. (118) reads:

$$\rho(t) = \rho_{\text{nt}} \int_{-\infty}^t \exp \left(- \int_{t'}^t [W''_{\text{ofi}} - W''_{\text{ava}}] dt'' \right) W'_{\text{ofi}} dt' \quad (192)$$

where e.g. $W'_{\text{ofi}} \equiv W_{\text{ofi}}[\mathcal{I}(t')]$. Eq. (192) is similar to Eq. (188), thus its solution is similar to Eq. (191) and reads:

$$\rho(t + \Delta t) = e^{-\int_t^{t+\Delta t} [W'_{\text{ofi}} - W'_{\text{ava}}] dt'} \left\{ \rho(t) + \frac{\Delta t}{2} \rho_{\text{nt}} W_{\text{ofi}}[\mathcal{I}(t)] \right\} + \frac{\rho_{\text{nt}} \Delta t}{2} W_{\text{ofi}}[\mathcal{I}(t + \Delta t)]. \quad (193)$$

The solutions (193) and (191) take the generic form:

$$A(t + \Delta t) = a[A(t) + \eta Q(t)] + \eta Q(t + \Delta t), \quad (194)$$

where a and η are step-dependent constants and $Q(t)$ is a known function over the whole integration domain. With the (a, η) couples indicated in table 8, the discretized version of Eq. (194) which read as

$$A_{l+1} = a[A_l + \eta Q_l] + \eta Q_{l+1}, \quad (195)$$

allows for the determination of the electron density and current densities over the entire time window by a loop over the time index l .

3.3.2 Numerical implementation of the Raman-Kerr response

The inclusion in the numerical scheme of the Raman-Kerr contribution is formally equivalent to that of the plasma. We indicate two possibilities to achieve this task.

- 1. Resolution of an ordinary differential equation: Assuming that the envelope $\mathcal{E}(r, t, z)$ is known at a given propagation distance z , both the electron density $\rho(r, t, z)$ and the Raman-Kerr contribution $Q_i(r, t, z) = \int_{-\infty}^t \mathcal{R}_0 \exp[-\Gamma(t - \tau)] \sin[\omega_R(t - \tau)] |\mathcal{E}(r, \tau, z)|^2 d\tau$ are solutions to a non-homogeneous ODE that involves $\mathcal{E}(r, t, z)$ as a source term. The temporal profiles $\rho(r, t, z)$ and $Q_i(r, t, z)$ are indeed obtained for each fixed spatial coordinate (r, z) by solving Eq. (118) for ρ with boundary condition $\rho(-\infty) = \rho_0 \ll \rho_{\text{nt}}$ and Eq. (120):

These tasks can be done by any ODE solver based on, e.g., the Runge-Kutta scheme.

- 2. Direct resolution. An explicit formulation satisfying Eq. (120) exists for the Raman-Kerr response (the electron density, solution to Eq. (118) admits a similar and simpler explicit formulation):

$$Q_i(r, t, z) = \int_{-\infty}^t \mathcal{R}_0 \exp[-\Gamma(t - \tau)] \sin[\omega_R(t - \tau)] |\mathcal{E}(r, \tau, z)|^2 d\tau \quad (196)$$

which can be rewritten as the imaginary part of

$$Q(r, t, z) = \mathcal{R}_0 \left\{ e^{-\Gamma t + i\omega_R t} \int_{-\infty}^t e^{\Gamma\tau - i\omega_R\tau} |\mathcal{E}(r, \tau, z)|^2 d\tau \right\}. \quad (197)$$

A numerical scheme to compute Eq. (197) is obtained by using a trapezoidal evaluation of the integral term:

$$Q(r, t + \Delta t, z) = e^{(-\Gamma + i\omega_R)\Delta t} Q(r, t, z) + \mathcal{R}_0 \frac{\Delta t}{2} \left[|\mathcal{E}(r, t + \Delta t, z)|^2 + e^{(-\Gamma + i\omega_R)\Delta t} |\mathcal{E}(r, t, z)|^2 \right]. \quad (198)$$

Discretization of this scheme leads to an expression allowing the calculation of the temporal profiles for the complex Raman-Kerr response $Q(r, t, z)$ at each fixed spatial position (r, z) .

$$Q_{j,l+1}^n = \left\{ e^{(-\Gamma + i\omega_R)\Delta t} Q_{j,l}^n + \mathcal{R}_0 \frac{\Delta t}{2} [|E_{j,l+1}^n|^2 + e^{(-\Gamma + i\omega_R)\Delta t} |E_{j,l}^n|^2] \right\} \quad (199)$$

from which $Q_i(r, t, z) \equiv \text{Im}(Q_{j,l}^n)$ is obtained. Scheme (199) must be inserted within an outer loop on j (transverse coordinate) and an inner loop on l (time).

4 Worked out modeling examples

This section presents selected worked-out simulation examples designed for teaching purposes during the Stella-School 2011 [9]. The examples illustrate mini-projects spanning the build-up of a simulation engine, the assessment of its numerical correctness as well as the set-up and execution of numerical experiments on ultrashort laser pulse propagation, from the very basics up to a full-blown simulation project.

The following examples consists of two subsections relying on the complementary approaches presented in sections 2 and 3. In the first part, authors aim to address the needs of readers who would like to hone their simulation-code building skills. Useful hints are summarized for implementing numerical schemes presented in section 3 and tested step by step. Linear propagation of a chirped pulse in a dispersive media is used as a specific example to illustrate the main principles of the suggested bottom-up approach for a step by step code implementation and testing. In this subsection, we then continue with the presentation of new numerical results for the nonlinear propagation, filamentation and pulse-splitting of a chirped pulse in water.

In the second subsection, we want to approach readers who want to jump right into the numerical experiments. We envision that experimentalists may be interested in using simulators in this way, i.e., as a vehicle for a numerical experiment. A simulation engine was used to design and perform a pump-probe numerical experiment, the aim of which is to infer the nature of nonlinearity that occur within an optical filament.

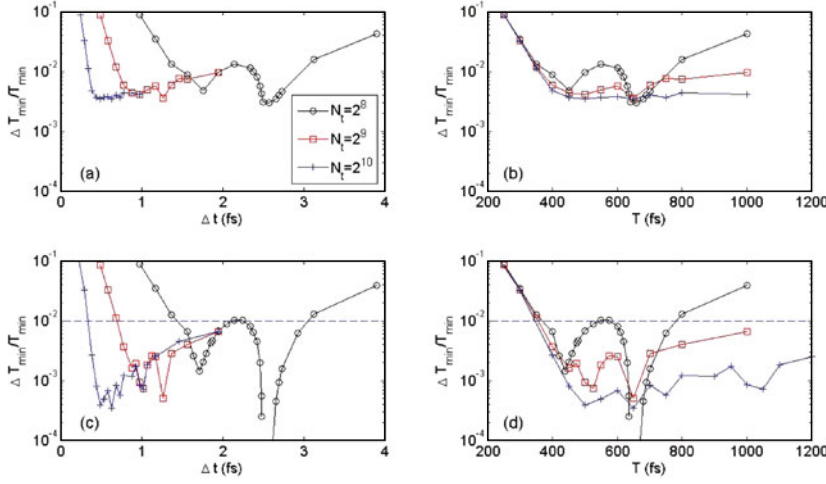


Fig. 2. Relative error $\Delta T_m/T_m$ as a function of parameters of the numerical scheme. The three curves refer to different numbers of grid points in the temporal dimension: circles: $N_t = 2^8$, squares: $N_t = 2^9$, cross: $N_t = 2^{10}$. The temporal step-size Δt is fixed by the choice of the box-size $\Delta t = T/(N_t - 1)$. The step-size along the z -direction is (a),(b) $\Delta z = 300 \mu\text{m}$, and (c),(d) $\Delta z = 30 \mu\text{m}$. The dashed line indicates a predefined tolerance value.

4.1 Simulation project example using Nonlinear Envelope Equations

4.1.1 Linear propagation of chirped pulses in water

We implemented model Eq. (159) in order to numerically simulate the linear propagation of a chirped pulse undergoing the effects of diffraction and dispersion. The input pulse is a Gaussian pulse with central wavelength $\lambda_0 = 800 \text{ nm}$, pulse duration $\tau_{FWHM} = 100 \text{ fs}$, beam width $w_0 = 100 \mu\text{m}$, temporal quadratic phase with a chirp coefficient $C = -10$ as defined by Eq. (158). The medium is water with the GVD coefficient $k_0^{(2)} = 241 \text{ fs}^2/\text{cm}$. We applied the scheme described in section 3.1.3, i.e. a split-step scheme relying on a Fourier transform to treat dispersion in the spectral domain and a Crank-Nicolson algorithm described in table 3 to treat the diffraction term.

First we investigated the effects of finite box- and step-sizes. We monitored the numerically simulated minimal pulse duration $T_m^{(num)}$, maximum intensity and its position in local time. We then calculated relative errors associated with these quantities when Δz , the step size along the propagation direction, N_t , the number of grid points and T , the temporal box-size are varied. Figure 2 shows the relative error for the minimal duration $\Delta T_m/T_m \equiv (T_m^{(num)}/T_m) - 1$ as a function of various numerical parameters, where $T_m \equiv \tau_{FWHM}/\sqrt{1 + C^2}$ denotes the minimum pulse duration according to the laws for Gaussian optics (see Sec. 3.1.3). Each subfigure shows curves referring to different number of grid points N_t in the temporal dimension. Figures 2(a) 2(b) were obtained with $N_z = 100$ propagation steps (step size $\Delta z = 300 \mu\text{m}$), whereas figures 2(c) 2(d) were obtained for $N_z = 1000$ steps ($\Delta z = 30 \mu\text{m}$). Comparison of these figures shows that the error is smaller for a smaller step size. We performed all calculations with the same value of T and N_t but increased N_z up to 4000 and we did not observe any change in the value of $\Delta T_m/T_m$ with respect to the case $N_z = 1000$. This indicates that $N_z = 1000$ points are sufficient to accurately model dispersion with our input parameters. Figures 2(b) and 2(d) exhibit a higher error for

small box sizes indicating finite box effects. This effect corresponds to small temporal steps in figures 2(a) and 2(c). For large step- or box-sizes each figure exhibits an increase of the relative error due to a too coarse resolution. All curves exhibit a minimum error indicating the best box size or temporal resolution that can be achieved with a given number of grid points. A peculiar feature is observed in Figs. 2(c) and 2(d) where the relative error changes sign in a certain range of box sizes ($\Delta t \approx 2.5$ fs, $T \approx 640$ fs; negative values are not shown in Fig. 2 due to the logarithmic scale). This feature is an effect of the coarse resolution and does not correspond to a true minimum of the relative error.

If we define a tolerance value of, e.g. 10^{-2} , for the relative error $\Delta T_m/T_m$, the intersection of the dashed line and a curve for a given number of points in Fig. 2(c) and 2(d) indicates the range of box or step sizes that can be used without exceeding the predefined tolerance.

4.1.2 Nonlinear propagation of chirped pulses in water

Marburger's formula (104) is known to reproduce well the power threshold for catastrophic behavior and position of the collapse when a non-chirped powerful pulse propagates in a pure Kerr medium. The goal of this section is twofold:

- First it constitutes an example of implementation of one of the most general numerical schemes designed for simulations of Nonlinear Envelope Equations.
- Second, we present the results of numerical experiments with intense chirped pulses undergoing filamentation in a dispersive medium and we compare them with known results for pulse collapse. The filamentation threshold for non-chirped pulses is known to exceed P_{cr} and lead to pulse-splitting [30, 46]. By monitoring the position of the nonlinear focus and the chirped pulse-splitting dynamics, we extended Marburger's formulation coupled with the so-called moving focus picture [47–50] to fit our numerical results for the splitting velocity. This extends the moving-focus model to media where intense laser pulses also undergo nonlinear losses and dispersion.

Numerical experiments on nonlinear propagation in water were performed by extending the code designed in section 4.1.1 so as to simulate the NLS-like propagation equation

$$\frac{\partial \mathcal{E}}{\partial z} = \frac{i}{2k_0} \Delta_{\perp} \mathcal{E} - i \frac{k_0''}{2} \frac{\partial \mathcal{E}}{\partial t^2} + i \frac{\omega_0}{c} n_2 \mathcal{I} \mathcal{E} - \frac{\beta_K}{2} \mathcal{I}^{K-1} \mathcal{E}, \quad (200)$$

where \mathcal{I} denotes the pulse intensity. Equation (200) includes a limited number of physical effects, namely diffraction, second order group velocity dispersion, optical Kerr effects and multiphoton absorption. However, it is used as a simplified prototypical model for nonlinear pulse propagation, allowing for an implementation of the extended Crank-Nicolson scheme as described in Sec. 3.1.2. As a follow-up to previous section, a split step scheme was used, treating dispersion in the Fourier domain for the first half-step, and other effects in the temporal domain for the second half-step. The simulation of Eq. (200) aims at interpreting the pulse splitting phenomenon, a standard effect in the physics of femtosecond filamentation [51, 52], in the framework of the moving focus model. Strictly speaking, the moving focus model does not accurately reproduce filamentation physics in dispersive media [53] but we will show that relaxing its underlying assumptions allows for the derivation of scaling laws that predict rather accurately the pulse-splitting velocities obtained by simulations of the propagation of chirped intense pulses described by Eq. (200).

Moving focus model. The moving focus model consists of a slice by slice pulse self-focusing in the sense that the pulse is viewed as a collection of independent thin time

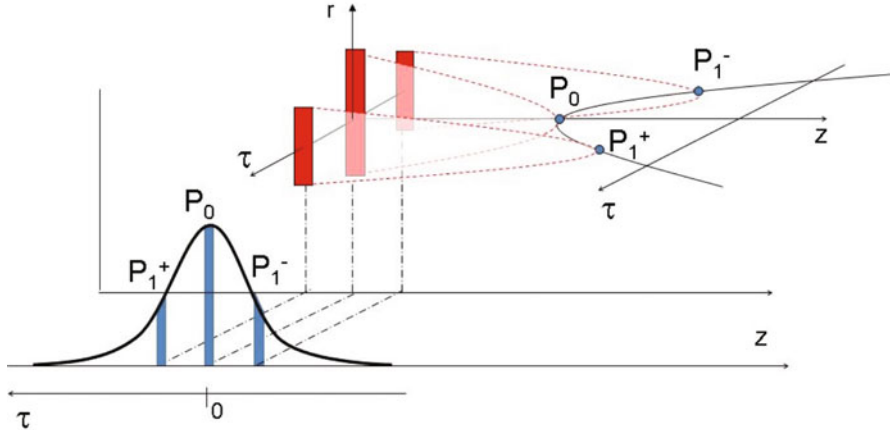


Fig. 3. Prediction of the moving focus model for the nonlinear beam-foci associated with given power for each time slice within the pulse. The time slice with peak power P_0 collapses at the shortest distance from the laser. Time slices with smaller power P_1^\pm collapse farther on the propagation axis while the central time slices undergo nonlinear absorption. The simultaneous collapse of two time slices P_1^- and P_1^+ on the ascending and descending edges of the pulse lead to pulse splitting.

slices undergoing self-focusing [50,54]. This assumption is valid when the physical effects coupling the various time slices together can be neglected. Each time slice contains a given power. In an ideal Kerr medium, all central slices with power above critical would collapse at distances that become larger as the corresponding power is closer to P_{cr} . The slices with power below P_{cr} diffract. In a real medium, several physical effects can arrest collapse, e.g., nonlinear losses reduce power of collapsing time slices once intensity exceeds a certain threshold. In this process, an intensity maximum (nonlinear focus) is reached and the propagation continues. The nonlinear foci corresponding to the different temporal slices of the pulse with power above critical do not appear simultaneously in the laboratory frame, and can be viewed as a moving focus. Figure 3 shows the locations of the nonlinear foci corresponding to the peak power P_0 of the pulse, and those corresponding to a smaller power P_1^- in the leading or P_1^+ in the trailing part of the pulse. In a pure Kerr medium, these beam collapse positions are predicted by the Marburger formula (104) [29]. In the presence of nonlinear losses, the slices with larger power collapse faster and lose at least part of their power, thereby leading to the occurrence of pulse splitting beyond the nonlinear focus. It manifests itself in the form of two intensity peaks departing from each other, each corresponding to the nonlinear focus of a given time slice [55]. In a dispersive medium, the assumption of independent time slices no longer holds, however, we still expect the moving focus model to accurately predict the positions of nonlinear foci and pulse splitting over distances shorter than the typical dispersive length. When the distance to the nonlinear focus and the dispersive length have the same order of magnitude, we will show that the moving focus picture and Marburger's formulation for beam collapse can be extended so as to fit the splitting velocities obtained from simulation results.

Numerical simulations of pulse splitting. The collimated input pulse has Gaussian intensity distribution in both space and time (see Eq. (158)), with pulse duration of 50 fs at full width at half maximum (FWHM), beam width $w_0 = 100 \mu\text{m}$, wavelength 800 nm. Medium parameters correspond to water: refractive index $n_0 = 1.328$, nonlinear refractive index coefficient $n_2 = 1.6 \times 10^{-16} \text{cm}^2/\text{W}$, dispersion

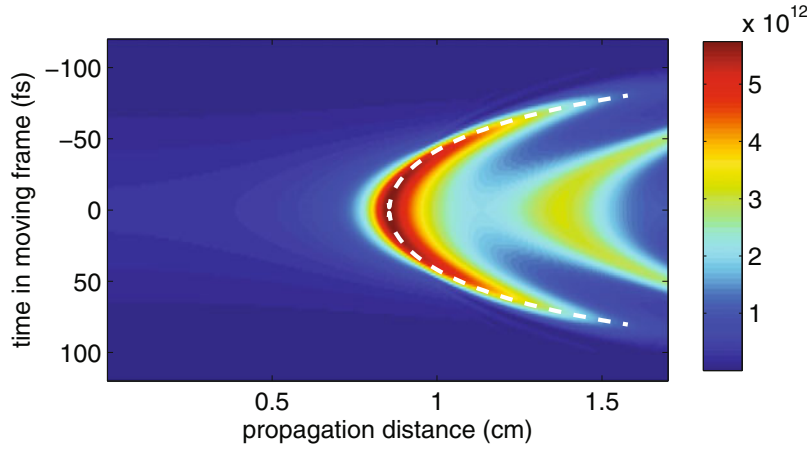


Fig. 4. Pulse intensity profile as a function of propagation distance. The input pulse power is $P_0 = 10P_{cr}$, and the input chirp is $C = -1$. The colorbar shows intensity in W/cm^2 . The white dashed curve represents the best fit, by using the modified Marburger law, of the peak positions of each sub-pulse resulting from pulse splitting beyond the nonlinear focus. A second nonlinear focus followed by another pulse splitting phenomenon can be observed about 1 cm beyond the main collapse.

coefficient $k_0^{(2)} = 241 \text{ fs}^2/\text{cm}$, cross-section for fifth-order multi-photon absorption $\beta_5 = 8 \times 10^{-50} \text{ cm}^7/\text{W}^4$ [51,52]. We investigated the effects of input peak power and initial pulse chirp. The input power varied from $1.5 P_{cr}$ to $50 P_{cr}$ and the pulse chirp parameter from -10 to 10 . Simulations were performed by setting the time window to $T = 400 \text{ fs}$ with $N_t = 2^8$ sampling points, and the propagation distance was divided into $N_z = 1000$ steps. These parameters closely correspond to those determined in section 4.1.1 to achieve the minimal relative error (See Fig. 2). To optimally use the computing time at a given resolution, the propagation length was adjusted from 1 to 3 cm so as to exceed 2.5 times the position of nonlinear focus roughly estimated with the original Marburger law.

Fig. 4 shows the evolution of the intensity profile of the pulse along the propagation distance for an input pulse power of $10 P_{cr}$ and chirp $C = -1$. Around $z = 0.8 \text{ cm}$, the intensity starts to increase, and beyond the nonlinear focus at $z \sim 0.9 \text{ cm}$ a splitting event is observed with the formation of two sub-pulses in the leading and trailing edges of the input pulse. Fig. 4 shows peak intensities of the leading and trailing pulses. The velocity of a given peak is given by $v_p = (v_g^{-1} + dt/dz)^{-1}$, where v_g denotes the moving frame or pulse group velocity and dt/dz , the inverse of the peak velocity in the local frame. The latter quantity is obtained from the slope of the curve in Fig. 4 representing the temporal position of the peak intensity in the pulse frame as a function of propagation distance.

Modified Marburger's law. We expect that Marburger's law (104), originally derived for the continuous wave regime from a fit of numerical simulation results, requires modifications to match the collapse position of chirped pulses. We will therefore fit our numerical results for the nonlinear foci by assuming a slice by slice self-focusing following a modified Marburger's law:

$$z_c(t) = \Delta z_c + \frac{b_M z_R}{\sqrt{[(P_{in}(t)/P_{cr})^{1/2} - a_M]^2 - (1 - a_M)^2}} \quad (201)$$

$$P_{in}(t) = P_0 \exp(-2t^2/r^2 t_p^2) \quad (202)$$

where a_M , b_M , Δz_c and r are free parameters to be determined by fitting numerical results. The original Marburger law (104) for slice-by-slice self-focusing is recovered for $a_M = 0.852$, $b_M = 0.367$ and $\Delta z_c = 0$, $r = 1$. The parameter Δz_c represents a shift along the z -axis of the nonlinear focus related to the most intense time slice, whereas the parameter r accounts for pulse lengthening or pulse shortening induced by dispersion and input chirp before the nonlinear focus.

We searched for parameters of the modified Marburger's law (201,202) realizing the best fit for each simulation performed with a given input chirp and input power P_0 . First, we allowed all parameters a_M , b_M , Δz_c and r to vary as a function of P_0 in the fitting procedure. However, best fits were obtained for nearly constant values of parameters $a_M = 0.7823$ and $b_M = 0.405$, close to original Marburger's coefficients. We therefore decreased the number of free parameters from four to two by keeping constant a_M and b_M and by allowing only Δz_c and r to vary as functions of P_0 and chirp C .

The dashed curve in Fig. 4 shows an example of best fit to numerical results. For a given input power P_0 , pulse splitting does only appear within a range of input chirps since dispersion induced pulse lengthening leads to a decrease of the pulse power below critical for strong chirp and low pulse power. Fits were therefore calculated for parameters that led to a clear splitting event. Furthermore, for the highest powers ($50 P_{cr}$), pulse reshaping into a flat-top pulse occurs before the nonlinear focus due to multiphoton absorption. In that case, a proper fit could not be obtained due to the assumption of a Gaussian pulse shape in the model [see Eq. (202)]. This restricts the validity of our fits to chirp coefficients between -5 and 5 and pulse powers up to $40 P_{cr}$.

Figure 5 summarizes curve fitting results. The parameter r takes into account pulse lengthening during the propagation toward the nonlinear focus and therefore naturally depends on both input chirp and power, which affects pulse reshaping through pulse dispersion and beam self-focusing. At a given input power, both r and Δz_c are quasi linearly dependent on the chirp parameter. However, a larger region of chirp parameter and pulse power needs to be investigated to confirm this linear dependence. Our data cover chirp coefficients between -5 and 5. Larger absolute values for the chirp coefficient led to more complicated dynamics during pulse propagation, for which pulse splitting was either absent or too short-lived to allow for an accurate fit. Powers between 1.5 and $40 P_{cr}$ and chirp coefficients between -5 and 5 led to clear pulse splitting events, and excellent agreement between numerical results and the modified Marburger's law for the splitting velocities. Positive chirp values lead to pulse lengthening and thus tend to shift the nonlinear focus toward larger distances with respect to the nonlinear focus of non-chirped pulses position of the collapse ($\Delta z_c > 0$ and increases with increasing C). In contrast, negative chirps lead to pulse compression and an increase of the peak power during the self-focusing stage, resulting in a shift of the nonlinear focus toward the laser ($\Delta z_c < 0$).

All numerical results shown in Fig. 5 can be approximated with phenomenological scaling laws that depend on the chirp parameter C and ratio $p \equiv P/P_{cr}$:

$$r = 1.58 + 0.0188(p - 1) + \frac{3.94 + 0.348 C}{\sqrt{p - 1}} \quad (203)$$

$$\Delta z_c = -0.0259 + 4.14 \times 10^{-5}(p - 1)^2 + \frac{5.49}{p^3} + \frac{0.536 C}{(p - 1)^{1.63}}. \quad (204)$$

We found in particular an excellent R -square of 0.9998 by fitting numerical results of Fig. 5a with Eq. (203) whereas the error in fitting numerical results in Fig. 5b with Eq. (204) does not exceed 10%.

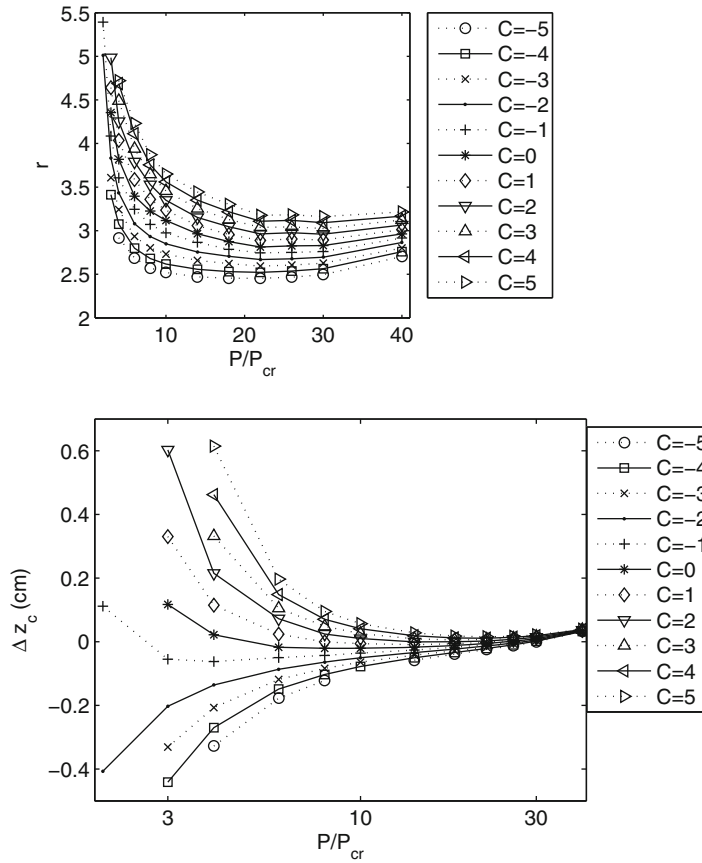


Fig. 5. Modified Marburger's law coefficient dependence on power for different pulse chirps.

We expect that this two-parameter modification of Marburger's law accompanied by the moving focus picture is generic enough to apply to other media and laser wavelengths. Scaling laws (203) and (204) have to be confirmed or adapted for different media and laser wavelength; in particular the exact value of the fitting parameters is expected to depend on medium dependent parameters such as the cross-section for nonlinear absorption and the GVD coefficient. This dependence has to be determined by fitting additional numerical results extending the results of this project. The method allows us to predict in a large parameter range the position in local time and the velocity of split-pulses formed by the filamentation dynamics in an ideal medium representing water. Extension of this moving focus picture to realistic condensed media that include high-order dispersion, plasma generation and Raman-Kerr effects, is an open question which may be answered to by relaxing the assumption of a frozen Gaussian profile for the pulse power in the moving focus picture, as proposed in e.g., Ref. [3,55].

4.2 Simulation project example using the UPPEcore simulator

The following Section is devoted to a worked-out example using the UPPEcore, which is a minimalist, but widely customizable software implementation of a UPPE solver. Its design combines a solver for a multi-component propagation equation as described in Sections 2 and 3, with most common options for nonlinear medium response models.

It also has an interface which makes it possible to add user-defined initial conditions, medium models and various operators acting on optical fields. While used as a vehicle for a simulation example, the UPPEcore is not the subject of this Section. Rather, we aim to discuss modeling and numerical issues which are universal, and common to numerical experiments supported by any simulation software.

On the modeling and computational level, our main goal is to illustrate the way a computational physicist designs and executes numerical experiments. This is why details, which are normally omitted in research papers, are provided in order to elucidate important numerical and practical issues. Our hope is that this will allow our reader to utilize this worked-out example as a self-study learning exercise.

On the nonlinear optics level, we describe a comprehensive computational model for a proposal of a pump-probe experiment with ultrashort femtosecond pulses, in which the aim is to compare manifestations of focusing and defocusing nonlinearities that occur *within* an optical filament. The scheme extends a recent experiment [56] which was designed to test a proposal that femtosecond filamentation may not require defocusing by free electrons. Beyond what was done in [56], here we want to explore additional possibilities in detection of the probe pulse. In particular, it is shown that angularly resolved spectra of the probe provide clear signatures that distinguish focusing and defocusing processes. Thus, the goal of the numerical experiment is to propose extension and provide a proof of principle for an experimental method to distinguish the Kerr interaction, occurring inside a femtosecond filament, from other types of nonlinear effects. For simplicity, we shall consider propagation in a noble gas (argon), assuming that the only nonlinear processes affecting pulse propagation are the instantaneous Kerr effect, multi-photon ionization, and interaction with free electrons (plasma). Naturally, chromatic dispersion of argon is also fully taken into account.

The experiment scheme is shown in Fig. 6. A high intensity pump pulse ($\lambda = 800$ nm) is strongly focused with lens f_1 , so that it undergoes filamentation through Kerr interaction and induces ionization in the focal region. A broad-beam second-harmonic probe pulse ($\lambda = 400$ nm) is injected at a much lower intensity from the second input port of beam-splitter BS_1 . Its linear polarization is set at $+45^\circ$ with respect to the pump pulse polarization, and a controlled delay is applied between the two pulses. While in a real experiment or in a full-blown simulation the pump-probe delay would be scanned, we restrict ourselves to comparison of two specific cases: We set the delay such that the pulses either overlap, or the probe propagates in the wake of the pump pulse through the filamentation region. In the latter case, field-plasma interaction is the only source of nonlinearity affecting the propagation of the probe, and its polarization is expected to remain unchanged, due to the isotropic nature of the plasma interaction. In the first case, i.e. when the two pulses overlap, the four-wave mixing process, originating in the third-order nonlinear response of the medium, will transfer some energy to the initially empty polarization direction of the probe field, at -45° .

We analyze the resulting properties of the probe beam after it samples the filament volume, and deduce from it information about the interactions taking place inside. We will look at the fluence profiles of the probe beam in the far field beyond focus, which mimics the use of a CCD camera to visualize the transverse profile of a beam. In order to extract as much information as possible, and in particular to explore the possibility to distinguish Kerr and plasma related effects, we utilize a polarizer in the detection path of the experiment. Alternatively, we examine the so called angularly resolved spectrum of the probe [57]. As will be seen shortly, the far-field spectrum as it is also often called is an attractive tool for this kind of experiment, because it carries both temporal and spatial information pertaining to the inside of the interaction zone which is otherwise difficult to access [34, 58–60].

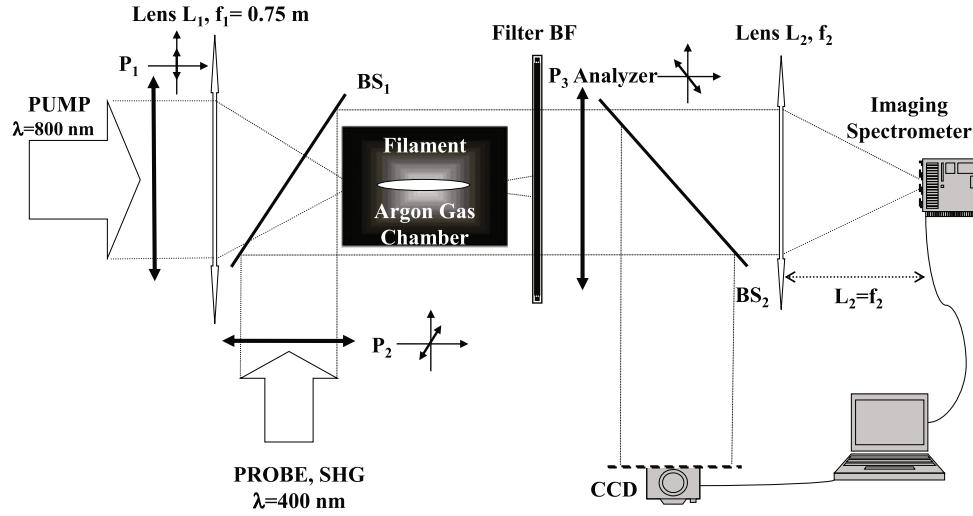


Fig. 6. Scheme of the simulated experiment: an intense, ultrashort pump pulse ($\lambda = 800$ nm, $\tau_p = 15$ fs) is focused by lens L1 in a gas chamber filled with argon at atmospheric pressure, where it undergoes filamentation. A broad-beam probe pulse ($\lambda = 400$ nm) polarized at $\theta = +45^\circ$ with respect to the polarization of the pump pulse, is injected through beam-splitter BS_1 with a tunable temporal delay, so that it can overlap with the pump pulse or follow in its wake through the focus region. The pump pulse is then blocked with a bandpass filter BF , while the probe is analyzed with the polarization filter P_3 in the orthogonal direction ($\theta = -45^\circ$) with respect to the initial polarization imposed by P_2 . The output field is divided by beam-splitter BS_2 and analyzed either with CCD and/or in an imaging spectrometer.

In order to give the reader an idea of how a practical simulation is actually executed, we next describe our procedure from the practitioner's point of view.

Most often, one requires to run a series of preliminary simulations in the beginning stages of a numerical experiment. To achieve an acceptable turn-around times in this set-up phase, simulations are run with relatively coarse resolutions of the computational domain grid. Later, a convergence study may be performed to determine numerical grid parameters for the final production runs. In this example, we initially used radial-temporal grids with 512 and 2048 sampling points for a domain with the radius of 2 cm and 300 fs temporal size. This gave us an acceptable resolution and qualitatively correct results in the preliminary runs which took typically only a few minutes to execute. Later, to produce data shown in this Section, we improved the computational domain parameters to those listed in Table 9, and a single run required about an hour of wall-clock time.

In the first case (referred to as Case A), the delay between the two pulses was adjusted so that they overlapped in the focal region, and so that Kerr effect is the main source of nonlinear interaction. Instead of scanning through the pump-probe delay values (as it would be done in real life) we performed a preliminary simulation (on a coarse grid) meant to find suitable temporal delay. To do this, we switched off all non-linear propagation effects, and observed pump and probe temporal intensity profiles on the logarithmic scale to confirm that the pulse delays are set properly. A similar procedure was applied to the second case (referred to as Case B) in which the probe tailed the pump pulse. Naturally, the temporal delays depend on the group velocity dispersion of the medium in which pulses propagate, and on the geometry of a given experiment. For the sake of simplicity, it was assumed here that propagation takes place in an argon gas from the beginning to the end.

Table 9. Select simulation parameters.

Computational domain properties	exploratory runs	production runs
temporal domain size	300 fs	600 fs
# of points in temporal direction	2048	4096
domain radius	2 cm	2 cm
# of points in radial direction	512	1000, 1500
runtime	few minutes	≈ 1 hour
Initial pump pulse parameters	sampling Kerr	sampling plasma
input intensity	$1 \times 10^{15} \text{ W/m}^2$	$1 \times 10^{15} \text{ W/m}^2$
wavelength	800 nm	800 nm
duration	15 fs	15 fs
beam waist	2 mm	2 mm
temporal shift (delay)	-24 fs	+50 fs
Initial probe pulse parameters (x,y pol. comp.)		
input intensity	$4 \times 10^{12} \text{ W/m}^2$	$4 \times 10^{13} \text{ W/m}^2$
wavelength	400 nm	400 nm
duration	15 fs	15 fs
beam waist	6 mm	6 mm
delay	+24 fs	-24 fs

To illustrate how initial simulation runs can be accelerated, we applied the following approximation. We ignore nonlinear effect during the initial propagation stage beyond the focusing lens where we consider the pump intensity to be low enough for the nonlinearity to be unimportant. Because the UPPEcore solver is spectral, propagation over this distance can be simulated in a single step while taking chromatic dispersion and diffraction properly into account. The nonlinear interaction was then activated in a 25 cm long region in the neighborhood of the focal point, starting 60 cm after the input plane. In order to speed up the simulation further, the pulses are also propagated linearly after this region, again in a single step. This approximation is legitimated by the low intensity of the two pulses outside the focal region and the weak nonlinearity of argon, but it has to be emphasized that it should not be used for publication-quality production runs. Nevertheless, as a practitioner’s trick for the initial stages of a project, it is very useful.

The scheme in Fig. 6 encompasses two experiments with different detection paths. To economize numerical calculations, we split the procedure into two simulation stages. The first covered the pulse evolution up to the end of the nonlinear focus domain, where the complete snapshots of the optical field were recorded into checkpoint data. This was subsequently retrieved by the same simulator performing calculations corresponding to the two different ways to detect the probe beam. This approach is often useful when a parameter space must be explored, and when at the same time a fully developed “nonlinear initial condition” (i.e. one that requires substantial numerical effort) can be utilized.

Table 9 collects some of the simulation parameters in order to illustrate typical parameters characterizing the numerical side of the simulation.

Next we discuss representative results produced in our simulations. First, let us consider the detection path in which a CCD camera records the spatial beam profile in the probe (see Fig. 6). Figure 7 shows characteristic patterns which reveal the presence of the focusing and de-focusing interactions in the nonlinear focal volume. These radial profiles depict fluence as it would be seen by a CCD (in the far field beyond the filament), and consist of a wide background given by the unperturbed probe beam, and of additional structures located around the center. These can be viewed as interference patterns between the original probe beam and the probe component

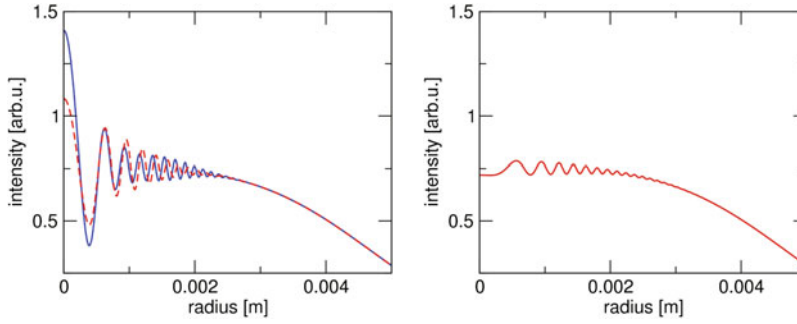


Fig. 7. Interference patterns in the probe beam detected by a model CCD (see Fig. 6). The left panel corresponds to the pump-probe delay which results in the overlap of the two pulses directly in the focal region. The right panel is obtained for the probe following the pump without a direct temporal overlap.

which diffracted off the refractive index perturbation created by the pump. Since the probe beam diameter is relatively large, its diffraction is negligible over the propagation distances characteristic for this numerical experiment. Consequently, it serves effectively as a plane-wave reference beam. In contrast, the refractive index perturbations in the filament are rather small-scale, and therefore act as a localized source of spherical waves emanating from the nonlinear focus. However, the whole picture is rather complex, because this source is spread over the length of the filament. Since the latter has a length of several centimeters in our case, one cannot understand its effect in terms of a thin phase screen. Rather, we observe a superposition of partial waves from all locations along the optical axis where the probe experienced effects of the pump or of the free electrons left in its wake. Moreover, time dependence of the Kerr-induced nonlinear index changes impose modulation on the probe pulse and result in a nontrivial spatio-temporal spectrum. We will show how this can be used to obtain more information about the nonlinear processes in the filament.

An important point is that the detected pattern depends on the polarization when the probe pulse samples the Kerr effect induced by the linearly polarized pump. This is visible in the difference between the blue and red lines in the left panel, which correspond to the parallel and perpendicular polarization (with respect to pump polarization direction) of the probe after interaction. The two polarization components could be observed experimentally by reorienting the polarization analyzer P_3 accordingly, i.e. parallel or perpendicular to the pump beam polarization. On the other hand, the effect of defocusing by free electrons, illustrated on the right, is isotropic and both polarization components of the pump suffer equal phase shifts. Consequently, the interference pattern induced by the plasma does not depend on the detected probe polarization. From this follows that the polarizer before the CCD detector can be utilized to distinguish between the Kerr effect (case a) and plasma-induced defocusing (case b).

Next we turn to an alternative way to detect the probe beam, shown as the horizontal path in Fig. 6. In this case, the detector is behind the analyzer oriented at 90 degrees with respect to the initial polarization of the probe beam. We consider either CCD or, alternatively, an imaging spectrometer recording an angularly resolved spectrum. Because of the crossed polarizers, only the light which experienced the nonlinear polarization rotation (due to the interaction with the pump pulse) is transmitted on the CCD detector. The observed pattern is illustrated in Fig. 8. The red curve shows a two-peak superposition for the pump-probe delay that samples the cross-phase modulation by the Kerr effect (case a). This is actually a part of the diffracting probe component we eluded to in the above paragraphs. In contrast, much

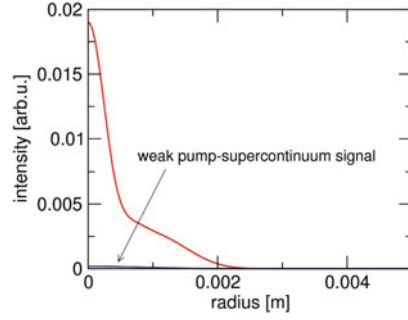


Fig. 8. Probe beam profiles detected behind the analyzer. Temporal pump-probe delays that result in sampling of the Kerr effect (case a) and defocusing by free electrons (case b) are depicted by the red and blue lines, respectively. With the crossed polarizer-analyzer pair, only the pulse component that resulted due to nonlinear polarization rotation is detected. Because the effect of free electrons is isotropic, the tiny signal shown in blue is only due to supercontinuum extending from the pump into the probe spectral region.

weaker signal is seen for the delay at which the probe only samples the plasma (case b). In fact the signal should be zero, and what we see is the energy of the supercontinuum extending from the pump [61, 62]. Because the supercontinuum is mostly linearly polarized, it results in a tiny but non-zero signal on the detector. This measurement scheme thus presents the option to eliminate the isotropic plasma effects, and only observe the instantaneous Kerr-induced interaction.

A more sophisticated way to distinguish between the effects originating in the Kerr and plasma, is based on the so called angularly resolved spectra. These can be measured for the resulting probe beam as indicated in Fig. 6 depicting the scheme of our numerical experiment. The lens f_2 collects the light emanating from the filament region, and focuses all rays with a common direction (angle) to the focal plane. In its focal plane. If the latter coincides with the entrance slit of an imaging spectrometer, each spatial direction is separately spectrally analyzed. As a result, we obtain a two-dimensional map of spectral power as a function of angle of propagation (after the nonlinear focus) and frequency (or wavelength). We use transverse wave numbers instead of angles, as these remain invariant when the beam passed between different media. A real spectrum analyzer, that resolves angles rather than transverse wave vectors, would give a slightly deformed version of the density plot reported in Fig. 9, because of the broadband nature of the source.

Angularly resolved spectra of the probe are depicted in Fig. 9. The left panel shows the spectrum for the pump-probe delay that samples the Kerr effect, and the panel on the right represents the analogous result for a long probe delay at which only plasma-related effect modify the probe.

One can see a clear difference; Because the Kerr effect results in the time-dependent index perturbation, it imprints on the probe spatial *and* temporal changes. As a result, the angularly resolved spectrum exhibits a relatively complex structure. For now we leave the interesting question if this structure can be used for an inversion problem to deduce the map of the Kerr induced change of the refractive index within the filament, and turn to comparison with the spectrum induced by plasma effects. Because the probe samples free electron density which is barely changing in time (e.g. on the nanosecond time scale due to recombination), there is very small temporal modulation. This results in the far-field spectrum that extends in the radial direction, but has no structure in the frequency direction. The radial extent is larger than that of the Kerr-induced spectrum, which reflects the fact that the plasma density is concentrated in a spatially narrower region. This clearly shows that angularly

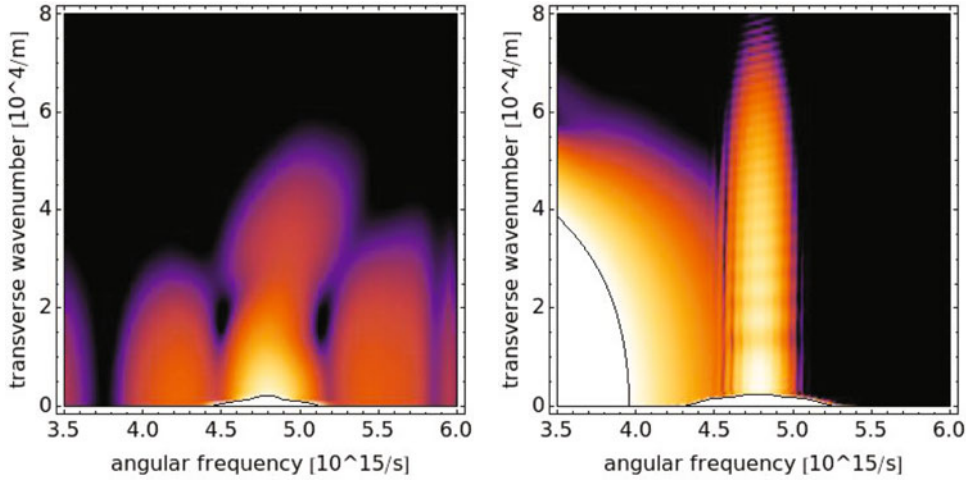


Fig. 9. Angularly resolved spectra of the probe pulse. The left panel illustrates the effect of the Kerr induced cross-phase modulation imposed on the probe beam by the pump (case a). The right panel shows the result of de-focusing of the probe by the free electrons left in the wake of the pump pulse (case b). The over-saturated region in the right panel is the supercontinuum light originating from the pump pulse. Both panels have the same dynamic range of four orders of magnitude, but the second spectrum is biased to lower intensity – this is why the supercontinuum components are much less prominent in the left panel.

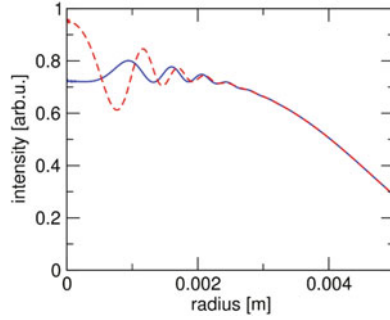


Fig. 10. Interference patterns in the 2-micron wavelength probe beam as detected by a model CCD (see Fig. 6). Due to the longer wavelength, the signal from free electrons is relatively stronger compared to the case of 400 nm wavelength probe shown in Fig. 7.

resolved spectra can be used experimentally to help distinguish the origin of the non-linear response. It may therefore be used as an important tool to guide experimental investigation on filamentation in nonlinear media.

Finally, let us briefly examine the role of the probe wavelength. There is of course the issue of detection, but for the purpose of this exercise we do not want to consider this (in practice very important) aspect of the problem. Rather, we concentrate on the physical properties which affect how the probe responds to the filament. Let us therefore consider a probe beam, perhaps created in an OPA from the pump pulse, at a central wavelength of 2 micron. Figure 10 shows the probe beam profiles for two pump probe delays, in analogy to Fig. 7. One can see that the signal from the plasma induced defocusing (blue) becomes relatively stronger in comparison with the

Kerr signature (red). This is because the defocusing power of free electrons is inversely proportional to the light frequency, while the Kerr-induced index is only weakly wavelength dependent. Thus, longer probe wavelength is advantageous when one needs to improve sensitivity to plasma-related effects.

Another effect brought in by the longer probe wavelength is the stronger diffraction. This manifests itself in the wider spreading angle of the interference pattern we observe. Picture 10 would therefore be recorded closer to the filament to accommodate the interesting part of the probe beam on the given CCD chip.

Yet another issue to consider is the separation between the probe and pump light in detection. Because the pump spectrum can broaden significantly, a small portion of it can be detected in the spectral range of our probe. Clearly, our measurement scheme works best when this undesirable signal can be kept sufficiently small. In the present illustration, having the probe on the longer wavelength side of the pump results in a better separation of pump and probe spectral components. Naturally, the choice of the probe pulse will be mainly decided based on the detection and generation possibilities, and on the type of the data one aims to collect (e.g. CCD pictures as opposed to only total energy for the curves shown in Fig. 8), but it is important to keep in mind the probe wavelength effect for the purpose of interpretation.

On the computational level, the probe wavelength will affect the separation between the initial pulses in the computational domain (which reflects the relative temporal delays). The group-velocity difference between the pump and probe also affects how different temporal slices of the pump are sampled. For example, the second harmonic is able to sample the leading edge of the pulse without experiencing the plasma induced defocusing because the slower probe always leads the pump pulse during their approach to the focal region. On the other hand, longer wavelength probe can cleanly sample the free electrons left in the wake of the pump pulse, without interacting with the strong pump at all. In this sense the two approaches can be viewed as complementary.

5 Conclusion

The last decade has brought lot of progress in ultrafast nonlinear optics, especially in the area of generation and control of femtosecond pulses with extreme intensities. This advancement would not be possible without the contribution of numerical simulations. Computer models have not only been instrumental in interpretation of experimental results, but represent the most important component of the theoretical picture. As a result, a growing number of researchers in the area wear two hats, one of an experimentalist and one of a computational physicist. Ranks of those who need to utilize computing as a component of their experimental work are wider still.

This motivated the inclusion of a simulation and modeling course in the experimental Stella 2011 Summer School on laser physics, and writing of this guide. Our main goal was to provide a self-contained overview of theoretical approaches and practical computer simulation methods relevant in the general area of nonlinear optics. Most of the material is presented at a level of detail which is not usual for regular research papers or review articles, and most modeling problems are discussed from more than one point of view. This approach was chosen to facilitate the second, but not less important aim of this work, namely to serve as an introduction into computer simulation for the broadest possible audience of researchers and students.

The numerical experiments have been performed in the context of STELLA, the School for Training in Experiments with Lasers and Laser Applications, held at the Insubria University in Como from June 20 to July 8 2011 (see www-stella-school.eu). The Authors wish to acknowledge CARIPLO, UNIVERCOMO and Banca del Monte di Lombardia Foundations for having financed the project. M.K. is grateful for the support from the U.S.A. Air Force Office for Scientific Research through the grant no. FA9550-10-1-0064 and Multi University Research Initiative FA9550-10-1-0561. The Authors like also to acknowledge Dr. Yi Liu for his careful reading of the manuscript, and the STELLA-school students for their support in developing the numerical laboratory used during STELLA.

Appendix A. Useful definitions

In order to facilitate navigation throughout this paper, we provide tables with a list of abbreviations (see Table 10) and a list of symbols used in Equations of this paper (see Table 11).

A.1 Abbreviations

A.2 Symbols

Table 10. List of abbreviations.

PDE	Partial Differential Equation
ODE	Ordinary Differential Equation
UPPE	Unidirectional Pulse Propagation Equation
FME	Forward Maxwell Equation
FWE	Forward Wave Equation
FOP	First-Order Propagation equation
NLS	Nonlinear Schrödinger Equation
NEE	Nonlinear Envelope Equation
LEE	Linear Envelope Equation
FEE	Forward Envelope Equation
PC-NLS	Partially Corrected Nonlinear Schrodinger Equation
SVEA	Slowly Varying Envelope Approximation
SEWA	Slowly Evolving Wave Approximation
SEEA	Slowly Evolving Envelope Approximation
GFEA	Generalized Few-cycle Envelope Approximation
MA	minimal approximation
PA	Paraxial Approximation
FFT	Fast Fourier Transform
FHT	Fast Hankel Transform
MPI	Multiphoton Ionization
MPA	Multiphoton Absorption
GVD	Group Velocity dispersion
THG	Third Harmonic Generation
SPM	Self Phase Modulation
SCG	Super Continuum Generation
CEP	Carrier Envelope Phase
FWHM	Full Width at Half Maximum

Table 11. List of symbols.

Symbol	Unit	Physical quantity or constant
$\mathbf{E}, E, \mathcal{E}$	V/m	electric field (vector, scalar, envelope)
$\mathbf{B}, B, \mathcal{B}$	H/m	magnetic field (vector, scalar, envelope)
$\mathbf{H}, H, \mathcal{H}$	H/m	magnetic induction (vector, scalar, envelope)
$\mathbf{D}, D, \mathcal{D}$	C/m ²	displacement field (vector, scalar, envelope)
$\mathbf{J}, J, \mathcal{J}$	A/m ²	free charge current (vector, scalar, envelope)
$\mathbf{P}, P, \mathcal{P}$	C/m ²	nonlinear polarization (vector, scalar, envelope)
$\mathbf{P}^{(1)}, P^{(1)}, \mathcal{P}^{(1)}$	C/m ²	Linear polarization (vector, scalar, envelope)
\mathbf{e}_s	-	unit vector in the polarization plane (direction)
\mathbf{z}	-	unit vector in the z -direction
A_+, A_-, A_μ	units of A	amplitudes of the forward (+) or backward (−) propagating components
$\lambda = \pm 1, \pm$	-	indicator for forward or backward propagation
$\mathcal{E}_\lambda, \mathcal{H}_\lambda$	-	harmonic wave solutions to Maxwell equations
$\mathcal{E}_0, \mathcal{H}_0$	-	amplitudes of harmonic waves
$\mathcal{E}_m, \mathcal{H}_m$	-	amplitudes of transverse modes
$N_m(\omega)$	-	normalisation constant
X, Y, T	m, m, s	normalization volumes or window sizes
$\delta_{m,n}, \delta_{\Omega,\omega}$	-	Kronecker symbols
$\epsilon_0 = 8.85 \times 10^{-12}$	F/m	permittivity of free space
$\mu_0 = 4\pi \times 10^{-7}$	H/m	permeability of free space
$c = 2.998 \times 10^8$	m/s	light velocity in vacuum
$m_e = 9.11 \times 10^{-31}$	kg	electron mass
$q_e = 1.60 \times 10^{-19}$	C	electron charge
$\hbar = 1.05 \times 10^{-34}$	m ² kg/s	Planck constant
ω	s ⁻¹	frequency coordinate
ω_0, ω_r	s ⁻¹	pulse central and reference frequencies
$\Omega \equiv \omega - \omega_0$	s ⁻¹	frequency departure from ω_0
t, τ, t'	s	(laboratory, local) time coordinate
z, ζ	m	propagation coordinate
x, y	m	transverse coordinates
$\epsilon(t), \epsilon(\omega)$	-	permittivity of the medium
$\chi^{(1)}(\omega)$	-	material linear susceptibility
$n(\omega)$	-	linear refraction index
$n_0 \equiv n(\omega_0)$	-	linear refraction index at ω_0
\mathcal{I}	W/m ²	$\mathcal{I} = \epsilon_0 c n_0 \mathcal{E} ^2 / 2$, Pulse intensity
$\mathcal{E}_{\omega_0}, \mathcal{E}_{3\omega_0}$	V/m	Electric field envelopes for fundamental and third harmonic pulses
$k(\omega) \equiv n(\omega)\omega/c$	m ⁻¹	material dispersion relation
$k_0 \equiv k(\omega_0), k_r \equiv k(\omega_r)$	m ⁻¹	wavenumbers at frequency ω_0, ω_r
$v_g \equiv 1/k_0^{(1)}, v_f$	m/s	pulse group and moving frame velocities
$k_0^{(l)} \equiv d^l k / d\omega^l _{\omega_0}$	s ^{l} /m	dispersion coefficients
$\kappa(\omega) \equiv k_0 + k_0^{(1)}(\omega - \omega_0)$	m ⁻¹	propagation constant in NEEs with MA
$\mathcal{D}(i\partial_\tau) \equiv \sum_{l=2}^{+\infty} \frac{k_0^{(l)}}{l!} (i\partial_\tau)^l$	m ⁻¹	high-order dispersion
K_z, K_ζ	m ⁻¹	propagation constants for the canonical equation
\mathcal{Q}, \mathcal{Q}	m ⁻¹	nonlinear dispersion operators for the canonical equation
$\mathcal{K}_0(\Omega) \equiv \mathcal{K}(\Omega, \mathbf{k}_\perp = 0)$	m ⁻¹	linear frequency dispersion
$\partial_z \equiv \partial / \partial z$	m ⁻¹	partial derivative with respect to z
$\mathbf{r} \equiv (x, y), r \equiv \sqrt{x^2 + y^2}$	m	transverse coordinate vector, modulus

Table 11. Continued.

Symbol	Unit	Physical quantity or constant
k_x, k_y, k_z	m^{-1}	transverse (x, y) and longitudinal (z) wave numbers
$\mathbf{k}_\perp \equiv (k_x, k_y)$	m^{-1}	transverse wave vector
$k_\perp \equiv \sqrt{k_x^2 + k_y^2}$	m^{-1}	modulus of the transverse wave vector
$\Delta_\perp, \nabla_\perp^2$	m^{-2}	transverse Laplacian
$\chi^{(3)}$	m^2/V^2	material third-order susceptibility
n_2	m^2/W	nonlinear index coefficient
α	-	fraction of delayed contribution to the Kerr effect
ω_R, Γ	s^{-1}	characteristic Raman frequencies
Q_i	V^2/m^2	effective oscillator amplitude (Raman response)
$\mathcal{R}_0 \equiv (\Gamma^2 + \omega_R^2)/\omega_R, \mathcal{R}(t)$	s^{-1}	Raman response (amplitude and functional form)
K	-	number of photons involved in MPA
β_K	$\text{W}^{1-K} \text{m}^{2K-3}$	cross section for multiphoton absorption
σ_K	$\text{s}^{-1} \text{W}^{-K} \text{m}^{2K}$	cross section for multiphoton ionization
U_i	J	ionization potential or gap
$W(\mathcal{I}), W_{\text{ofi}}, W_{\text{ava}}$	s^{-1}	ionization rate, optical field ionization, avalanche
τ_c	s	collision time
ρ, ρ_{nt}	m^{-3}	density of electrons and neutral atoms
ρ_c	m^{-3}	critical plasma density
ρ_f	m^{-3}	density of free space charge
$\sigma(\omega)$	m^2	cross section for inverse Bremsstrahlung
P_{cr}, P_{in}, P_0	W	critical, input and peak powers
$p = P_{in}/P_{cr}$	-	ratio of input to critical powers
f, d_f	m	beam curvature (focal length) and focal distance
w_0, w_f	m	beam radius ($1/e^2$), waist
$z_R \equiv k_0 w_0^2/2, z_f \equiv k_0 w_f^2/2,$	m	Rayleigh lengths for input beam width or waist, Dispersion length
$z_{ds} \equiv t_p^2/2k_0^{(2)}$	-	chirp coefficient
C	-	pulse duration (half duration at $1/e^2$, FWHM)
t_p, τ_{FWHM}	s	
$w(z), R(z), T(z), \Psi(z), \Phi(z)$	m, m, s, -, -	beam width, curvature, pulse duration, axial phases in laws for Gaussian optics
$T_m \equiv t_p/(1 + C^2),$ $z_m \equiv -Cz_{ds}/(1 + C^2)$	s, m	minimal pulse duration (chirped pulse) and pulse shortening distance
$\Delta r, \Delta x, \Delta z$	m	radial, transverse and longitudinal step-sizes
$\Delta t, \Delta \omega$	s, s^{-1}	time and frequency step-sizes
x_{\min}, x_{\max}	m	boundaries of the transverse numerical grid
r_{\min}, r_{\max}	m	boundaries of the radial numerical grid
$\omega_{\min}, \omega_{\max}$	s^{-1}	boundaries of the spectral grid
N_\perp, N_x, N_t, N_z	-	numbers of steps in radial, transverse, time and longitudinal directions
M, K_{\max}	-	numbers of propagation steps between numerical diagnostics

Table 11. Continued.

Symbol	Unit	Physical quantity or constant
Δ_j, Δ_t		discretized Laplacian operators
$\nu = 0$ or 1	-	switch between planar and cylindrical geometries
$\delta = \Delta z / 4k_0(\Delta r)^2$	-	normalized diffraction coefficient
$d = -\Delta z k_0^{(2)} / 4(\Delta t)^2$	-	normalized dispersion coefficient
$L_{\pm}(\delta) \equiv 1 \pm i\delta\Delta_j$, $L \equiv L_-^{-1}L_+$	-	tridiagonal matrices in the Crank-Nicolson scheme
$L_{+,l}, L_{-,l}$	-	frequency dependent tridiagonal matrices
$\mathcal{K}_l, \mathcal{D}_l$	m ⁻¹	discretized values for \mathcal{K} and \mathcal{D} at ω_l
$\delta_l = \frac{\Delta z}{4(\Delta r)^2 \mathcal{K}_l}$		frequency dependent diffraction coefficient
$d_l = \frac{\Delta z \mathcal{D}_l}{2}$		discretized dispersion values
\mathcal{L}, \mathcal{N}		linear and nonlinear source terms
$N_j^n, N_{l,j}^n$	-	discretized nonlinearity at z_n, r_j, ω_l
A^* (or c.c.), A^T	-	complex conjugate of A , transpose of A
$A * B$	-	convolution
$\hat{A}(x, y, \omega)$		1D Fourier transform of $A(x, y, t)$, ($t \rightarrow \omega$)
$\tilde{A}(k_x, k_y, \omega)$		3D Fourier transform of $A(x, y, t)$
$a_M, b_M, r, \Delta z_c$	- , - , - , m	coefficients of modified Marburger's model

References

1. F. Krausz, M. Ivanov, Rev. Mod. Phys. **81**, 163 (2009)
2. E. Esarey, Rev. Mod. Phys. **81**, 1229 (2009)
3. A. Couairon, A. Mysyrowicz, Phys. Rep. **441**, 47 (2007)
4. M.B. Gaarde, J.L. Tate, K.J. Schafer, J. Phys. B.: At. Mol. Opt. Phys. **41**, 132001 (2008)
5. M. Kolesik, J.V. Moloney, Phys. Rev. E **70**, 036604 (2004)
6. D. Faccio, A. Couairon, P. Di Trapani, *Conical Waves, Filaments and Nonlinear Filamentation Optics* (Aracne, Roma, 2007)
7. P. Maine, D. Strickland, P. Bado, M. Pessot, G. Mourou, IEEE J. Quant. Electron., **24**, 398 (1988)
8. A. Braun, et al., Opt. Lett. **20**, 73 (1995)
9. <http://www.stella-school.eu/>
10. M. Kolesik, J.V. Moloney, M. Mlejnek, Phys. Rev. Lett. **89**, 283902 (2002)
11. A.V. Husakou, J. Herrmann, Phys. Rev. Lett. **87**, 203901 (2001)
12. H.S. Chakraborty, M.B. Gaarde, A. Couairon, Opt. Lett. **31**, 3662 (2006)
13. M.B. Gaarde, A. Couairon, Phys. Rev. Lett. **103**, 043901 (2009)
14. M. Geissler, G. Tempea, A. Scrinzi, M. Schnürer, F. Krausz, T. Brabec, Phys. Rev. Lett. **83**, 2930 (1999)
15. P. Kinsler, G.H.C. New, Phys. Rev. A **67**, 023813 (2003)
16. M.A. Porras, Phys. Rev. A **60**, 5069 (1999)
17. T. Brabec, F. Krausz, Phys. Rev. Lett. **78**, 3282 (1997)
18. J.V. Moloney, A.C. Newell, *Nonlinear Optics* (Westview Press, Boulder, Colorado, 2004)
19. J.D. Jackson, *Classical Electrodynamics*, 3rd edn. (Wiley, New York, 1998)
20. M.D. Feit, J.A. Fleck, Jr., J. Opt. Soc. Am. B **5**, 633 (1988)
21. A. Lotti, D. Faccio, A. Couairon, M.B. Gaarde, P. Di Trapani, Phys. Rev. A **83**, 053804 (2011)
22. A. Couairon, H.S. Chakraborty, M.B. Gaarde, Phys. Rev. A **77**, 053814 (2008)
23. D.S. Steingrube, E. Schulz, T. Binhammer, M.B. Gaarde, A. Couairon, U. Morgner, M. Kovačev, New J. Phys. **13**, 043022 (2011)

24. E. Schulz, D.S. Steingrube, T. Binhammer, M.B. Gaarde, A. Couairon, U. Morgner, M. Kovačev, *Opt. Express* **19**, 19495 (2011)
25. <http://refractiveindex.info/>
26. G. Fibich, B. Ilan, *Physica D* **157**, 112 (2001)
27. V.G. Dmitriev, G.G. Gurzadyan, D.N. Nikogosyan, *Handbook of Nonlinear Optical Crystals*, 3rd edn. edited by A.E. Siegman, Springer Series in Optical Sciences vol. 64, (Springer, Berlin, 1999)
28. Y. Silberberg, *Opt. Lett.* **15**, 1282 (1990)
29. J.H. Marburger, *Theory. Prog. Quant. Electr.* **4**, 35 (1975)
30. G.G. Luther, J.V. Moloney, A.C. Newell, E.M. Wright, *Opt. Lett.* **19**, 862 (1994)
31. A. Couairon, *Phys. Rev. A* **68**, 015801 (2003)
32. N. Aközbe, A. Iwasaki, A. Becker, M. Scalora, S.L. Chin, C.M. Bowden, *Phys. Rev. Lett.* **89**, 143901 (2002)
33. Y. Liu, M. Durand, A. Houard, B. Forestier, A. Couairon, A. Mysyrowicz, *Opt. Commun.* **284**, 4706 (2011)
34. A. Couairon, E. Gaizauskas, D. Faccio, A. Dubietis, P. Di Trapani, *Phys. Rev. E* **73**, 016608 (2006)
35. S.C. Rae, K. Burnett, *Phys. Rev. A* **46**, 2077 (1992)
36. E. Yablonovitch, N. Bloembergen, *Phys. Rev. Lett.* **29**, 907 (1972)
37. D. Faccio, et al., *Opt. Lett.* **32**, 184 (2007)
38. D. Faccio, et al., *Opt. Express* **15**, 13077 (2007)
39. A.-K. Kassam, L.N. Trefethen, *SIAM J. Sci. Comput.* **26**, 1214 (2005)
40. W.F. Ames, *Numerical methods for Partial Differential Equations*, 2nd edn. (Academic Press, New York, 1977)
41. W.H. Press, S.A. Teukolsky, W.T. Vetterling, B.P. Flannery, *Numerical Recipes* (Cambridge University Press, Cambridge 1992)
42. J. Crank, P. Nicolson, *Proc. Camb. Phil. Soc.* **43**, 50 (1947)
43. F. Collino, *J. Comput. Phys.* **113**, 164180 (1997)
44. J. Strikwerda, *Finite Difference Schemes and PDEs*, 2nd edn. (SIAM, 2004)
45. S.M. Cox, P.C. Matthews, *J. Comp. Phys.* **176**, 430 (2002)
46. D. Faccio, et al., *Phys. Rev. A* **78**, 033826 (2008)
47. M.M.T. Loy, Y.R. Shen, *Phys. Rev. Lett.* **22**, 994 (1969)
48. V.N. Lugovoi, A.M. Prokhorov, *JETP Lett.* **7**, 117 (1968)
49. V.N. Lugovoi, A.M. Prokhorov, *Sov. Phys. Uspekhi* **16**, 658 (1974)
50. Y.R. Shen, *Principles of Nonlinear Optics* (Wiley, New York, 1984)
51. S. Minardi, A. Gopal, M. Tatarakis, A. Couairon, G. Tamosauskas, R. Piskarskas, A. Dubietis, P. Di Trapani, *Opt. Lett.* **33**, 86 (2008)
52. S. Minardi, A. Gopal, A. Couairon, G. Tamosauskas, R. Piskarskas, A. Dubietis, P. Di Trapani, *Opt. Lett.* **34**, 3020 (2009)
53. P. Whalen, J.V. Moloney, M. Kolesik, *Opt. Lett.* **36**, 2542 (2011)
54. A. Brodeur, C.Y. Chien, F.A. Ilkov, S.L. Chin, O.G. Kosareva, V.P. Kandidov, *Opt. Lett.* **22**, 304 (1997)
55. A. Couairon, *Eur. Phys. J. D* **27**, 159 (2003)
56. P. Polynkin, M. Kolesik, E.M. Wright, J.V. Moloney, *Phys. Rev. Lett.* **106**, 153902 (2011)
57. D. Faccio, et al., *J. Opt. Soc. Am. B* **22**, 862 (2005)
58. M. Kolesik, E.M. Wright, J.V. Moloney, *Phys. Rev. Lett.* **92**, 253901 (2004)
59. D. Faccio, et al., *Phys. Rev. E* **72**, 037601 (2005)
60. M. Kolesik, E.M. Wright, J.V. Moloney, *Opt. Express* **13**, 10729 (2005)
61. M. Kolesik, G. Katona, J.V. Moloney, E.M. Wright, *Phys. Rev. Lett.* **91**, 043905 (2003)
62. M. Kolesik, G. Katona, J.V. Moloney, E.M. Wright, *Appl. Phys. B* **77**, 185 (2003)